Probing the electrical properties of multilayer graphene

Submitted by Tymofiy Khodkov to the University of Exeter as a thesis
for the degree of Doctor of Philosophy in Physics
December, 2012

This thesis is available for Library use on the understanding that it is copyright material and that no quotation from the thesis may be published without proper acknowledgement.

I certify that all material in this thesis which is not my own work has been identified and that no material has previously been submitted and approved for the award of a degree by this or any other University.

Tymofiy Khodkov
December, 2012

Abstract

Graphene is a new two-dimensional (2D) material with unique electrical transport, optical and mechanical properties. However, monolayer graphene (MLG) is a gapless semiconductor, which limits its relevance for transistor applications where a large on/off ratio of the current is required. In this work the investigation of transport properties of few-layer graphene (FLG) is presented. These 2D electronic systems offer a novel solution to the problem concerned the absence of an energy gap in single layer graphene, since they exhibit an electric field and stacking-dependent band gap in the energy dispersion.

Thus far, a clear observation of a band-gap in multilayer graphene (e.g. Bernal-stacked bilayers) in transport measurements was hindered by the presence of disorder. Here we develop a reliable and effective method of fabrication of high-quality suspended double-gated graphene devices, which are of crucial importance for probing the low-energy dispersion of few-layer graphene. The current annealing technique, described in details, improves transport characteristics like carrier mobility, which is typically higher than $\sim 10^4$ cm^2/Vs for our multilayer devices.

Electrical transport experiments on suspended dual-gated ABC-stacked trilayer are performed. We report the direct evidence of the opening of a tunable band-gap with an external perpendicular electric field, ranging from 0 meV up to 5.2 meV for an electric field of 117 mV/nm. Thermally activated transport is observed in these samples over the temperature range 0.5 - 80 K. The values of energy gap extracted from both temperature dependence of minimum conductivity measurements and non-linear $I-V$ characteristics correlate well. Our experimental results are in a good agreement with theoretical approximation, based on self-consistent tight-binding calculations. The high quality of our ABC trilayer samples is also demonstrated by a particularly high on/off ratio of the current (250 at applied electrical displacement as low as 80 mV/nm), which makes these devices promising for future semiconductor electronics.

FLG samples with reduced disorder allow us to observe quantum Hall effect (QHE) at magnetic field as low as 500 mT. We present the first study of electric field- induced new QH states in ABC trilayer graphene (TLG). The transitions between spin-polarized and valley polarized phases of the sample at the charge neutrality point are investigated. Resolved novel broken symmetry states along with observed Lifshitz transition

in rhombohedral TLG display exciting phenomena attributed to rich physics in these interactive electronic systems.

Acknowledgements

Here I would like to acknowledge several people, whose help an inspiration made a significant contribution for this work to be successful.

Firstly, and the most importantly, I thank my decedent supervisor Alex K. Savchenko, without whom this PhD would not have started. He selected me out of dozen of other competitive students and gave the opportunity to do the research in the QSNM lab. Alex was always willing to help at any issue, not only concerning physics. His strict nature and, at the same time, kindness created a very special, friendly and encouraging working atmosphere in the lab. It was very nice of him to organize the trips and show lots of beautiful places in Cornwall and Devon. Thanks to him I realized what real science should be. I am glad and very proud that I worked with Alex. It was a big loss of such a good scientist and a human for all. Heavenly Kingdom to him! He was a great man.

I want to express a huge thanks to my supervisor Saverio Russo, who took the responsibility of me after the sudden death of Alex Savchenko. Saverio is pushing physicist, helping me and motivating to do the research. I am thankful to him for teaching me a lot, not only about the measurement techniques, but also how the things should be organized. The latter helped me a lot and, without no doubt, this knowledge will be helpful in future. A great sense of humor in his italian manner and his "Focus!" I will never forget. And I very much appreciate the valuable contribution of Monica Craciun - the main person in the "Russo-team" - in writing the papers and discussing the results.

I am grateful to Prof. Adrian Whyatt, who helped me during my 1st year of study and was always full of enthusiasm. My gratitude to Prof.Bill Barnes for being my mentor over the whole PhD. My deepest acknowledgements to David Anderson, Dave Horsell and Mark Heath. They taught me how to operate with many different equipment in the cleanroom. Without this knowledge I would not succeed.

It was a big pleasure for me to work all three years with the colleagues and concurrently my friends, who kindly shared their knowledge and experience within the group,- Ivan Khrapach, Alexey Kaverzin, Alexey Kozikov, Dave Hudson, Tom Bointon, Eugine and Arseny Alexeev, Sneha Eashwer-Singhraj, Fedor Tikhonenko. Especial thanks to Fred Withers, Adam Price, Peter Hale, Samuel Hornett for their help in correcting my

English.

The role of people from theory group - Andrey Shytov, Eros Mariani and Michail Portnoi- should not be underestimated. They were always happy to help me with the understanding of arisen questions in physics. And I am thankful to Sasha Mayorov and Roman Gorbachev from Manchester Group for their useful proposals in improving my fabrication and measurement techniques. Also, big thanks to Jens Martin, who helped me sometimes in the data interpretation.

A separate gratefulness should be given to University of Exeter, provided me with financial support over all three years of PhD research.

Many thanks to technicians and other staff from the Physics Department. Paul Wilkings performed all the necessary technical jobs in the mechanical workshop. Without a permanent supply of liquid Helium by David Gregory and Adam Woodgate the low-temperatures measurements would not be possible. I am thankful to office staff, in particular to Liz Roberts and Natalia Ogrina, for doing all the bureaucratic jobs. I was glad to deal with John Meakin from stores, who supplied us with all required things and who was always exhilarated, conveying his positive mood to other people. I want also to say thanks to Sam - the cleaner, who maintained our lab tidy. I thank Dave Colridge and Chris Forest for hardware and software support and all other people from the department, who I forgot to mention here.

A great thanks to you all, Margarita Mikelane, Tanya Chistova, Dmitry Karaskevich, Yuri Marusiak, Archil Tscickaridze, Juliya Dautova, Pavel and Katya Burovskii - my friends here, in Exeter. They made my life joyful in UK. It was awesome to have fun together. My special gratitude to cheerful friendly people from Exeter Uni Windsurf Society, who introduced me to amazing world of windsurfing that allowed me to perceive the beauty and the freedom of the ocean. That was very inspiring and always gave a new strength for my further work.

Massive acknowledgements to all those people, who were far away but always stayed with me in heart. Special thanks to my best friend Andreii Pitirimov, whom I know from the early childhood, and Lyudmila Frolochkina. They always believed in me and shared all my success and failures.

Finally, I must to highlight the importance of my family, especially the parents Irina and Viktor Khodkov. Thanks them for my education. Their warmth and support during the whole time I was here are priceless.

List of publications

[3] Observation of a gate tunable band-gap in electrical transport in ABC-trilayer graphene. **Tymofiy Khodkov**, Ivan Khrapach, Monica F. Craciun and Saverio Russo. Under review in *Phys. Rev. Lett.* (2012)

[2] Electrical transport in suspended and double gated trilayer graphene. **Tymofiy Khodkov**, Freddie Withers, David Christopher Hudson, Monica Felicia Craciun, and Saverio Russo *Appl. Phys. Lett.* 100, 013114 (2012).

[1] S. Russo, M. F. Craciun, **T. Khodkov**, M. Koshino, M. Yamamoto and S. Tarucha (2011). Electronic Transport Properties of Few-Layer Graphene Materials, Graphene - Synthesis, Characterization, Properties and Applications, Jian Ru Gong (Ed.), ISBN: 978-953-307-292-0, InTech

Symbols and abbreviations used

2D/3D : two/three dimensional (if not concerned Raman spectrum)

MLG (SLG) : monolayer graphene (single layer graphene)

TLG (FLG) : trilayer graphene (few-layer graphene)

ABA (ABC) : Bernal (rhombohedral) stacking order

FET : field effect transistor

(F)QHE : (fractional) quantum Hall effect

2DEG : two dimensional electron gas

DOS : density of states

BZ : Brillouin zone

LL : Landau level

SdH : Shubnikov-de Haas

NP : neutrality point

LT : Lifshitz transition

IPA : isopropanol

PMMA : polymethylmethacrylate

PMGI :Polymethylglutarimide

FWHM : full width at half maximum

AFM : atomic force microscopy

HF : hydrofluoric acid

DC : direct current

e : elementary charge

γ_i (i=0,1,2...) : coupling constants between atomic sites

ϕ_0 : magnetic flux quantum

$h, \hbar$: Planck's constant

σ : conductivity

l : mean free path

$L; W$: length;width of a sample

l_B : magnetic length

μ : mobility

m, m_e : mass of electron

m^* : effective mass

n, n_e : carrier concentration

ν : Landau level filling factor

ρ : resistivity

τ : scattering time

v_F : Fermi velocity

V_g : gate voltage

ω_c : cyclotron frequency

Contents

Abstract **2**

Acknowledgements **4**

List of publications **6**

Symbols and abbreviations used **7**

Contents **9**

List of Figures **12**

List of Tables **22**

Introduction **23**

1 Theoretical background **27**

1.1 Crystallographic structure of single layer grephene 27

1.2 Tight-binding approximation 28

1.3 Band structure of trilayer graphene 32

1.3.1 Introduction 32

1.3.2 Bernal-stacked trilayer 34

1.3.3 ABC-trilayer 36

1.3.4 Lifshitz transition 38

1.4 Band-gap engineering in graphene-based systems 40

1.4.1 Introduction 40

1.4.2 Symmetry breaking and the role of screening in multilayer devices 41

1.4.3 Related experiments 42

1.5 Properties of 2D graphene based structures 44

1.5.1 Density of states 44
1.5.2 Berry's phase 45
1.6 Quantum Hall Effect in 2DEG systems 47
1.6.1 Introduction 47
1.6.2 Classical Hall Effect 47
1.6.3 QHE in 2DEG 49
1.6.4 LLs in graphene 53
1.6.5 Related experiments and theoretical expectations 56

2 Fabrication and characterization of samples. Experimental techniques 60
2.1 Introduction 60
2.2 Graphene-based transistors 60
2.3 Thickness and quality determination 64
2.3.1 Optical contrast 64
2.3.2 Raman spectroscopy 66
2.3.3 Atomic force microscopy 70
2.3.4 Conclusions 72
2.4 Low-temperature set-up 74

3 Fabrication of high quality double-gated devices 77
3.1 Introduction 77
3.2 High quality samples: fabrication approaches 78
3.3 Suspended gate fabrication 81
3.4 Etching of SiO2 85
3.5 Improving the quality of the samples 89
3.5.1 Thermal annealing 90
3.5.2 Current annealing 93
3.6 Results 100
3.7 Conclusions 104

4 Gate tunable band-gap in rhomboherdal-stacked trilayer 105
4.1 Introduction 105
4.2 Device characterization and description 106

4.3 Low-T measurements 107
4.3.1 Resistance as a function of applied top- and back-gate voltages . 108
4.3.2 I-V characteristics and spectroscopy measurements 109
4.4 Temperature dependence analysis 110
4.5 Results 113
4.6 Conclusions 114

5 Quantum transport in multilayer graphene structures at high magnetic field 116
5.1 Introduction 116
5.2 Effect of external electric field on broken symmetry states in QH regime 117
5.2.1 Two terminal transport measurements in perpendicular magnetic field 117
5.2.2 Evolution of QH plateaux with carrier concentration and magnetic field 120
5.3 Signature of the Lifshitz transition 122
5.4 $\nu = 0$ LL and the transition between quantum Hall states 123
5.5 Conclusions 126

Conclusions and proposals for future work 127

Bibliography 131

I 138

II 140

III 142

IV 143

List of Figures

1.1 Graphene lattices in real (a) and reciprocal (b) space with unit vectors. Dashed and shadowed diamonds correspond to a unit cell and first Brillouin zone respectively. δ_1, δ_2 and δ_3 in (a) are vectors from one atom to the nearest neighbours. 28

1.2 Graphene's energy dispersion. 30

1.3 Schematic of atom arrangements in crystallographic structure of : (a),(b) Bernal-stacked bilayer and trilayer respectively, (c) rhombohedral trilayer. γ_0 and γ_1 are coupling constants. 33

1.4 Band structure of ABA trilayer graphene near the K point : (a) calculation includes only γ_0 and γ_1, $\Delta = 0$; (b) γ_0, γ_1, γ_2, γ_3, γ_4 and γ_5 are considered, $\Delta = 0$; (c) same as be with $\Delta = 0.5\gamma_1$, $\theta = \tan^{-1}(p_y/p_x)$. Adapted from [13] 36

1.5 Band structure of ABC-stacked trilayer graphene around the K_+ point along p_x axis plotted for different values of interlayer asymmetry . Adapted from [15] 38

1.6 Constant energy contour plot of the conduction band near zero energy. The units of energy are eV. $G = 4\pi/(3a)$ is a reciprocal vector's length. Adapted from [23] 39

1.7 Adapted from [32]:(a)The band structure of ABC trilayer graphene with (red) and without (green) the presence of a perpendicular electric field, calculated within the tight binding model. Transitions 1 and 2 are the strongest optical transitions near the K-point for electron doping. Inset: schematic representation of the trilayer device used in experiment. (b) Energy gap as a function of carrier concentration. The symbols are experimental data and the solid lines are the results of the TB model for ΔE_K(green) and E_g(blue), as indicated in (a). 43

1.8 The schematic of the density of states as a function of energy for : (a)conventional 2DEG, (b) monolayer graphene, (c) multilayer graphene with N$>$ 2 44

1.9 The schematic of the circuit for Hall Effect measurements. Black arrows along the sample indicate the current flow $\vec{\jmath}$ from the source to drain. The blue arrow shows the bend of the trajectories in the presence of a perpendicular magnetic field $\vec{B}$. Pluses/minuses signs at the edges demonstrate the negative/positive charge accumulation. V_{xx}(V_{xy}) is the voltage along(across) the sample. 48

1.10 (a) The density of states for the particles in magnetic field when the disorder and the spin is not taken into account. For comparison the shaded area shows the DOS when magnetic field is zero. (b) The schematics of the DOS of Landau levels for the real sample in the presence of disorder. Two regions of localized and extended states are labeled .The dashed line is the position of the Fermi level. 50

1.11 (a) A semiclassical view of the skipping orbits. (b) The schematic picture of two-terminal sample with chemical potentials μ_1 and μ_2 of the electrodes. The loops and curly lines demonstrates the equipotential line pattern of localized (in the middle) and extended (edge) states respectively determined by disorder. Black arrows indicate the current direction along the edge channels .(c) The energy landscape of the LL in the direction across the sample. The dashed line shows the position of the Fermi level. 52

1.12 Schematic illustration of the quantum Hall effect in (a) conventional 2DEGs, (b) monolayer graphene, (c) bilayer graphene and (d) ABC stacked trilayer graphene as a function of chemical potential μ at fixed magnetic field. The red line on each figure represents transversal conductivity σ_{xy} and blue shaded regions correspond to the DOS (it is inverted for holes for clarity). The chemical potential μ is measured in units of $1/\gamma_1^{N-1}\left(\sqrt{2}\hbar v/l_B\right)^N$ with $N = 1,2,3$ for mono-,bi- and ABC trilayer graphene respectively and in units of $\hbar^2/(m^* l_B^2)$ for conventional 2DEG. Adapted from [38]. 56

1.13 Hall conductivity of (a) ABA- and (b) ABC- stacked trilayer graphene calculated for different values of the interlayer asymmetry δ_1 induced by external perpendicular electric field. Adapted from [47]. 57

1.14 (a) Illustration of energy surface in ABC trilayer.(b) Adapted from [15]. Landau levels of ABC trilayer, plotted as a function of $\sqrt{B}$. Value of $\left(2\hbar v^2 eB\right)^{1/2}/\gamma_1 = 0.1$ corresponds to $B \sim 1$ T. The region where Landau levels are triply degenerate is shaded. The arrows show the corresponding areas in (a) below and above the Lifshitz transitions when degeneracy is broken. 58

2.1 Schematic image of the fabrication process of a standard device. . . . 62

2.2 (a) Typical $R(V_g)$ dependence. Blue(red) part of the curve corresponds to electron(hole) current. (b) Energy spectrum around Dirac point (D.P.- on the graph). Blue and red dashed lines represent the position of the Fermi level at positive and negative gate voltages respectively (regions on the dependence in (a)). Schematics of the experimental setup. 63

2.3 (a) An optical image of graphene flakes on top of Si/SiO_2 substrate. The number of layer are indicated by red arrows. (b) Color plot of the contrast as a function of wavelength and thickness of oxide layer (adapted from [51]). 65

2.4 The schematic of the electronic transition process for monolayer in: (a) G-peak, (b) D-peak, (c) 2D-peak. (d) The same as (c) but for bilayer graphene. $\vec{q}_{ij}$ (i=1,2; j=A,B) correspond to phonon vectors that take part in scattering process. 67

2.5 (a) Comparison of Raman spectra ($\lambda = 514$ nm) for bulk graphite and single layer graphene. The plots are scaled to have similar height of the 2D peaks. (b) Evolution of the 2D band with increasing number of layers. Adapted from [53]. 68

2.6 2D Raman peak (black) fitted with 6 Lorenzian functions (red) for : (a) ABC and (b) ABA trilayers. 69

2.7 Schematic of the atomic force microscope (AFM). The inset shows scanning electron microscopy image of the tip. 71

2.8 (a) Topography of graphene flakes on top of Si/SiO_2 substrate(AFM image); (b) a profile taken along a blue line in (a). 72

2.9 Normalized intensity of 2D Raman peaks for different mono-, bi- and tri- layers as the function of frequency Δx (cm^{-1}). The position of the right part of each curve where normalized intensity equals 0.5 was set as the origin for clarity. 73

2.10 Scheme of "Oxford instruments" Heliox-TL cryostat. 76

3.1 (a) Illustration of pre patterned structure with gold electrodes (see the description above). The distance between adjacent metal electrodes ranges from 1 to 3 μm, and the width of the pillars is 4-6 μm. Gray ellipse demonstrates graphene flake laying acros the trench. (b) Optical image of a real device shown in (a). Red dashed line surrounds the area with trilayer graphene flake. Poor contrast demonstrates that it is difficult to visualize suspended graphene on top of this structure. (c) and (d) AFM scan (3D image) of graphene flakes on top of etched holes and trenches, similar to illustrated in (a). The hole's diameter and trench's width are 1 and 2 μm respectively. 80

3.2 Fabrication process for air-bridge gate electrode. (a) Spin-coating the sample with two subsequent layers of soft and hard PMMA (1 and 2 respectively) followed be e-beam lithography. Inset: schematics of the top-view of patterned structure. (b) Metal evaporation and lift-off. Covering the sample with PMGI/PMMA1/PMMA2 polymers and electron beam lithography of the areas denotes as I and II on the inset. (c) Exposure of and development in PMMA developer only of the area marked by dashed rectangular on the inset. Shaded gray rectangles correspond to regions of developed polymers in step (b).(d) Evaporation of metal bridge and lift-off followed by removal of PMGI resist. 83

3.3 SEM micrograph of suspended metal bridge over the graphene flake. The region highlighted with dashed ellipse corresponds to the area with the hole, shown on the inset. Inset: top-view of the same device - the hole's diameter is about 150 nm and the width of the bridge is 350 nm. The scale bar corresponds to length of 1μm. 84

3.4 False color SEM micrograph a device etched with HF vapor. Yellow colored parts represent metal contacts. Scale bar corresponds to 3μm. . 85

3.5 Illustration of the set-up used for etching oxide layer in HF solution. The sample holder is shown on the left in the figure. The blue semi-sphere demonstrates the full coverage of the sample with a liquid droplet. . . . 86

3.6 False-color SEM micrograph of the samples after final step of wet chemical etching. Two different samples in (a) and (b) were kept in ultra-clean water to dilute BOE for less than 1 minute and 3.5 minutes respectively. The parts painted with yellow/green color represent contact/top-gate electrodes. Crystal-like structures on (a) correspond to organic residue after HF reaction in water and IPA. Scale bars on (a) and (b) are respectively 3μm and 500nm. 88

3.7 False-color SEM micrograph of collapsed contacts. Scale bar corresponds to 1μm. 89

3.8 False-color SEM micrograph of (a) suspended bilayer sample with Hall-bar geometry of the contacts, (b) suspended Aharonov-Bohm graphene ring. Scale bars correspond to 1μm. 90

3.9 Scheme of thermal annealing set-up in furnace. 91

3.10 Typical "annealing curve": resistance as a function of time during thermal heating at 120 ^{0}C. 92
3.11 Resistance vs back-gate voltage for the sample before(red) and after(black) thermal annealing at T = 120^{0}C. The measurements were performed at T = 4.2K. 93
3.12 Circuit for current-induced cleaning method. The RC-filter has total resistance 30 kΩ and the time constant ∼300 ms. The back-gate voltage is applied by "Keithley 2400" (voltage source) through 1GΩ resistor, served as a filter. 94
3.13 R(V_g) dependence of one of our sample, supported on SiO_2, before(black) and after(red) current annealing. 95
3.14 The effect of current annealing on different suspended trilayer graphene samples reflected on the dependence of the resistance as a function of gate voltage. The annealing was implemented by using (a) ramping technique, when current was gradually increased up to predefined value, and (b) pulse technique. "int" on the figure corresponds to intermediate step of annealing. 96
3.15 SEM image of the device exploded during current annealing. Scale bar corresponds to 2μm. 98
3.16 The example of the current annealing, when after a certain stage, the transport properties of the sample started to degrade until the total failure of the flake, represented as an evolution of the resistance as a function of gate voltage. Black and blue curves correspond to first and final annealing steps respectively. "Int1" and "Int2" represent two intermediate steps of annealing. 99
3.17 False-color SEM micrograph of suspended double-gated graphene devices. Yellow/green color correspond to metal contacts/gate electrode. Scale bar on (a) and (b) correspond to 1μm. Images on the right-hand side represent framed regions on (a) and (b) respectively (for the bottom right image the scale bar corresponds to 500nm), that were taken from different perspective. 101

3.18 (a) Resistance as a function of back-gate voltage for bilayer sample. (b) Mobility as a function of carrier concentration. The data are taken at $T = 4.2K$. 102

3.19 (a) Resistance versus back-gate voltage measured at T = 0.3K for different values of fixed top-gate voltage (V_{tg}) as indicated in the graph. (b) Schematic cross section of a suspended double gated device and the electrical measurement configuration. (c) Measurements of the on/off ratio of the current as a function of the average electric displacement D (see main text). 103

3.20 Conductance (G) vs. back-gate voltage measured for different values of perpendicular magnetic field. 104

4.1 (a) Energy dispersion for ABC-trilayer with zero (left) and finite (right) external perpendicular electric field. (b) 2D-Raman peak for ABC-trilayer measured with a 532nmn laser. The dots are the experimental data points, whereas the red continuous line is a fit to 6 Lorentzians (continuous blue lines). (c) False-color SEM micrograph of suspended double gated graphene device. Scale bar corresponds to 1μm. (d) Resistance vs back-gate voltage before(black) and after(red) current annealing. The data are taken at T = 4.2K. 107

4.2 Electric circuit for low-T conductance measurements in a voltage-biased two-terminal configuration. The resistances R_1 and R_2 are 10 MΩ and 100 Ω respectively. 108

4.3 (a) Zero-bias resistance versus V_{bg} measured at T = 300 mK and for different fixed V_{tg} as indicated in the graph. (b) 3D Plot of R vs. V_{bg} and V_{tg}. The dashed line is a guide line connecting the maximum of resistance R_{max}. (c) R(V_{bg}) for V_{tg} = 15V (left) and V_{tg} = 0V (right) and for different temperatures, as indicated in the graph. 109

4.4 Electric circuit for the measurements of $I - V$ and $dI/dV - V$ characteristics at low temperature. The resistances R_1 and R_2 and R_3 are respectively 10 MΩ, 10 kΩ and 100 Ω. 110

4.5 (a) Color plot of log(R) as a function of V_{tg} and V_{bg}. Yellow arrows indicate the directions of a constant carrier concentration and an electric displacement correspondingly. The inset shows $I - V$ characteristics at the R_{max} for 3 different gate configurations (I, II and III) highlighted in the main graph. The differential conductance dI/dV versus V_{sd} and V_{bg} for fixed V_{tg} corresponding to I, II and III is plotted in panel (b). The sketches on the right hand side show a schematic low-energy band structure of ABC-trilayer and the position of the Fermi level (E_F) for the three different values of V_{bg} indicated by the white dashed lines. . . 111

4.6 (a) Arrhenius plot for different values of external electric displacement. The dots are experimental data and the continuous lines are fit to thermally activated transport over the band-gap Δ.(b) Minimum conductivity as a function of inverse temperature for different average external electric displacements, as indicated. The dots are experimental data points, whereas the continuous line is a fit to Eq.(4.1). 112

4.7 (a)The values of the band-gap, extracted from the fit to experimental data using eq.(4.1), as a function of D. The continuous line is a fit to $\Delta \propto D^{3/2}$ (see the main text for the description). Linear fit of ln(Δ) vs. ln(D) with best fit $N = 3\pm0.3$. 113

4.8 (a)Energy gap Δ as a function of average electric displacement D. Red and blue circles correspond to two different samples, as indicated in the graph. 114

5.1 Conductance in units e^2/h as a function of V_{bg} for ABA(a) and ABC(b) trilayer graphene measured at T = 300mK. In (a) the data are taken at fixed magnetic field B = 3T for three values of top-gate voltages as indicated on the graph. The numbers on the blue curve correspond to different filling factors ν. In (b) the measurements are performed at B = 3(blue), 5(red) and 7(green) Tesla. The dotted and solid lines represent the data at fixed V_{tg} = 0 and 20 Volts respectively. 118

5.2 Schematic representation of the current lines in a sample with two-terminal geometry in the QH regime [111]. The current lines originate from one corner of the sample (left bottom corner) and terminate in the opposite corner. V_S and V_D denote source and drain voltage. 120
5.3 Fan diagram - dG/dB(in colour scale) as a function of gate voltage and magnetic field - of ABC trilayer at T = 0.3K. (a) The data are taken at fixed V_{bg} = 0V when V_{tg} is varied. (b) The top gate voltage is fixed (V_{tg} = 0V) and the V_{bg} is varied. Dashed lines in (a) and (b) are guide lines that correspond to filling factors ν (some of them are shown on the graphs), calculated as described in the main text. 121
5.4 (a) Fan diagram - dG/dB(V_{bg},B) - of ABC trilayer graphene at T = 300mK. The top-gate voltage is fixed at V_{tg} = 15V. The dashed lines are guide lines for calculated filling factors. Values of ν against given dashed lines are shown outside of the image. (b) High resolution scan related to (a). The measurements are performed over the range of B and V_{bg} indicated on the graph. The dashed black circles represent the regions of Landau levels splitting due to the Lifshitz transition. 123
5.5 (a) Colorplot of the conductance in units e^2/h as a function of applied out of plane electric and magnetic fields. The data are taken around neutrality point region. The dashed line guides the transition region between $\nu = 0$ and $\nu = 2$ states. The picture on the right is a schematic representation of the counter-propagating edge modes, which have opposite layer indices (U and L for upper and lower layers respectively). . 124
5.6 (a) Conductance of ABC trilayer (in units of e^2/h) at zero carrier concentration as a function of magnetic field for different fixed electric displacements D: the values are increasing from the top to bottom, as indicated on the graph. (b) Conductance (color scale) as a function of electric field D and magnetic filed B at zero carrier concentration. The data represent the result in (a) as the colorplot. The numbers on the figure denotes different quantum Hall states. 125

III.1 Etched depth of SiO_2 as a function of etching time. A buffered oxide etch solution comprises of 40% NH_4F and 49% HF in water, which are mixed in the proportion of 6:1 by volume respectively. 142

List of Tables

II.1 Thickness dependence on spin-coating parameters. 140
II.2 Thickness dependence on the concentration with respect to the "T-thinner". 140
II.3 Dilution speed of PMGI-SF6 resist in the MF-319/water solution (the proportion is 50%:50%). 141

IV.1 Statistics of suspended graphene samples broken by current annealing. 143

Introduction

Over the past decades the research community has challenged the difficulties standing in the way of discovering novel materials and exploration of new properties, pursuing the goal to satisfy the demands of general society - create reliable, cheap, handy, flexible, supersensitive and ultrafast electronic devices that can simplify our life. Since the end of the last century, emerging technologies have risen very fast with a trend towards a reduction in size of the primary components (e.g. individual transistor), as well as of the whole device, down to nanometer scales, thus, leading to a growth of a new separate research area called nanotechnology. Once an object is reduced in size below the mesoscopic range ($\sim$ 100nm), it starts to display its quantum nature. This results in observation of novel physical properties of the material, which instead of being a bulk 3D object behaves like new kind of system of one- (nanowires or nanotubes), two- (topological insulators, heterostructures and heterojunctions) and even zero-dimensions (quantum dots, quantum wells). The explored systems, in turn, give rise to a next generation of electronic devices. Finally, nanotechnologies have become an inalienable part of our daily life, serving as base components of modern computers, mobile phones, memory storage devices and so on.

Graphene is a new two dimensional (2D) system, which is as thin as a single atomic plane. Being the thinnest material in nature, graphene for a long time was thought not to exist as free 2D sheet due to its mechanical instability (it can be rolled into carbon nanotube or wrapped into buckyball). Only after the experimental discovery of graphene in 2004 did it became possible to investigate thoroughly this material, which in less than a decade has attracted enormous attention in scientific community. The interest in exploring new physical phenomena in this material is growing exponentially.

Some of the discovered properties of graphene make it promising for a big range of applications. Firstly, single layer graphene (SLG) is a good conductor with high room-temperature carrier mobility. That holds a promise for its integration into ultrafast electronic circuits. In addition, this material is a potential candidate for applications in spintronics due to its long spin relaxation time. Besides intriguing electrical properties, graphene is currently known as the strongest material in the world, and it is very flexible. Revealing itself to possess astonishing mechanical and thermal characteristics, SLG devices function in open atmosphere and are establishing themselves as an irreplace-

able part of novel nano-electro-mechanical systems (NEMS), which are widely used as sensors. Extremely sensitive transducers, based on NEMS with graphene membranes, nowadays capable of resolving the mass of single proton, are the key element aiming to satisfy the requirements of quantum metrology. Neither should one underestimate the high transparency of this material together with its flexibility, which gives us a big hope that innovative flexible and transparent electronics soon will be accessible for general society. After recent success in growing a large-scale SLG, world leading companies like "Samsung" have already started to introduce modern technologies based on graphene materials for the development of a new generation of TV-screens.

Apart from the enormous potential in electronic applications, graphene is a new base for fundamental research in solid state physics, because of the unique nature of charge carriers in this 2D electronic system. In graphene, the particles behave likewise photons, which is a manifestation of quantum electrodynamics in condensed matter. This is revealed in many captivating phenomena, such as anomalous integer quantum Hall effect (QHE) or Berry phase of π. The enormous scientific interest in this material eventually has led to the Nobel Prize award to its pioneers - K. Novoselov and A. Geim - in 2010.

Along with monolayer graphene its few-layer (FLG) counterpart recently attracted research attention due to unprecedented properties, like an electric field- and stacking-dependent band structure, that are not present in the single layer. In spite of being an exceptional material, monolayer graphene is a gapless semiconductor. This prevents the use of SLG in transistor electronics. The tunability of low-energy bands in multilayer graphene is a promising solution of the arisen problem. In order to measure directly in transport an electric field dependent energy gap in FLG, the samples with a reduced level of disorder are necessary. In addition to this, intriguing interaction effects are expected in FLG, such as new broken symmetry states in the QHE, and are of interest for study. The fabrication of high-quality suspended samples allows one to access low-energy states in the band structure and observe novel interaction phenomena in FLG. Also, graphene suspended membranes are core elements in future NEMS, which is on its own a promising area of research. Thus, a reliable method of production of mechanically stable, free-standing graphene samples is important for further study of electromechanical properties in SLG and FLG systems, which is the most challenging part of the growing NEMS research area.

The issues considered in the last paragraph are addressed in this work. The thesis is organized as follows:

Chapter1 introduces the main theoretical concepts of mono- (MLG) and few-layer graphene required for comprehension of the investigated transport phenomena. Considering the tight-binding approximation, we start by deriving the linear dispersion relation in MLG that result from atomic arrangements of carbon atoms in the crystallographic structure. The band structures of trilayer graphene is also considered within the tight-binding model. Unusual transport properties of charge particles in graphene-based systems lead to astonishing effects, like tunable low-energy bands and the Lifshitz transition in trilayer graphene (TLG) as well as an unconventional integer quantum Hall effect, which are discussed in detail.

In ***Chapter2*** we discuss the basic fabrication approach and characterisation of graphene devices - necessary steps in experimental study. Main accent is made on different methods of determination of the layers number and stacking arrangements of graphene flakes, since the distinction between two types of trilayers is crucial for our research. It is shown that the most reliable way to distinguish required samples is to combine Raman spectroscopy and optical contrast methods, analysing carefully the 2D-peak in the former. The basic principles of work of graphene-based field effect transistors (FET) and low-temperature transport measurements are also discussed.

Chapter3 is dedicated to a detailed description of the fabrication method of ultra-clean graphene samples with bridge-like gate electrodes. Starting with an outline of various techniques of production of high-quality samples, we analyze advantages and disadvantages of these fabrication approaches. A reliable and effective technique of making free-standing graphene membranes with suspended top-gate, which are the key part of our experiments, is presented. A particular emphasis is put on the improvement of the quality of our samples after fabrication steps, focusing mainly on current-induced cleaning method. Successful results obtained on our good-quality samples are demonstrated in the end of the chapter.

Chapter4 reports on the direct measurements in transport of an electric field-tunable band gap in ABC trilayer graphene. These observations stem from the high quality of our devices which results in the absence of any hopping mechanisms contributing to the conduction. We observe a large increase of the resistance as a function of external electric displacement and an increasingly nonlinear behavior of the current-

voltage characteristics consistent with the opening of an energy gap (Δ). At the same time, the temperature dependence of the conductivity is described by thermally activated transport over the energy-gap. The estimated values for Δ from the temperature dependence and from the current voltage characteristics follow the theoretically expected electric field dependence with critical exponent 3/2. Our findings indicate that we directly probe a bare gate-tunable energy gap in ABC TLG in electrical transport measurements.

In ***Chapter5*** we study TLG devices in the quantum Hall regime at various transversal external electric fields. New sequences of quantized plateaus are detected in trilayer samples of both types of stacking arrangement. Some resolved QH states are revealed to be independent of external out-of-plane electric field. We explore transitions between broken symmetry states of ABC trilayer at the neutrality point. Also, the observed splitting of Landau levels into three branches in rhombohedral TLG can be a signature of the Lifshitz transition. With this experiment we emphasize the importance of investigation novel broken symmetry states in multi-layer graphene samples due to their demonstrating fascinating interaction phenomena.

The last chapter summarizes obtained results and contains several suggestions for future experiments aiming to elucidate observed physical effects, which relate to the presented work and are of interest.

Chapter 1

Theoretical background

1.1 Crystallographic structure of single layer grephene

Graphene is a one-atomic plane of bulk graphite [1] which consists of sp^2 hybridized carbon atoms arranged on a two-dimensional honeycomb structure and bonded together via strong σ - bonds. The hexagonal lattice is not a simple Bravais lattice and the unit cell of graphene has two inequivalent atoms (Fig. 1.1(a)) A and B corresponding to the two different sublattices. The coordinates of the lattice vectors for a given sublattice are

$$\overrightarrow{a}_1 = \frac{a}{2}\left(3, \sqrt{3}\right), \overrightarrow{a}_2 = \frac{a}{2}\left(3, -\sqrt{3}\right), \tag{1.1}$$

where a is the distance between neighbouring carbon atoms and is approximately 0.142 nm.The lattice constant is then $a_L \sim 0.246$ nm. In the reciprocal space vector's coordinates are given by

$$\overrightarrow{b}_1 = \frac{2\pi}{3a}\left(1, \sqrt{3}\right), \overrightarrow{b}_2 = \frac{2\pi}{3a}\left(1, -\sqrt{3}\right). \tag{1.2}$$

There are two inequivalent points K and K' in the first Brillouin zone, that are called Dirac points and will be discussed later.

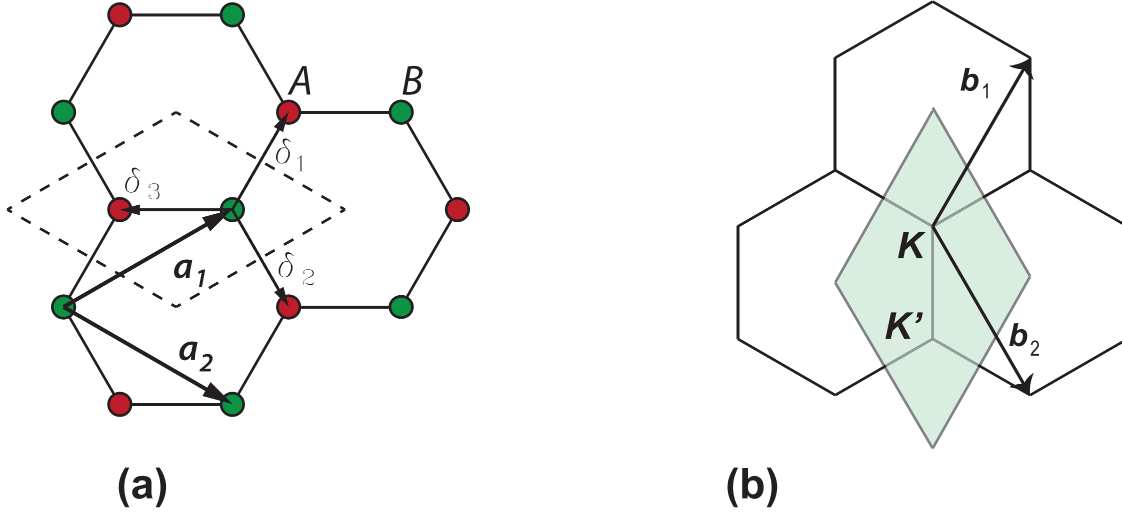

Figure 1.1: Graphene lattices in real (a) and reciprocal (b) space with unit vectors. Dashed and shadowed diamonds correspond to a unit cell and first Brillouin zone respectively. δ_1, δ_2 and δ_3 in (a) are vectors from one atom to the nearest neighbours.

1.2 Tight-binding approximation

The band structure of graphene was first calculated in 1947 [2] using tight-binding model. A carbon atom has 4 valence electrons on the outer shell with $2s$, $2p_x$, $2p_y$ and $2p_z$ orbitals. One s and two p ($2p_x$ and $2p_y$) valence electrons are responsible for the sp^2 hybridization and their in-plane σ - orbitals do not contribute to the conduction. The π - orbitals (electrons in $2p_z$ state) are perpendicular to the atomic plane and give the main contribution to the conduction mechanism at low energies. Following the tight-binding model one can consider the wave-function of the system as the linear combination of atomic orbitals of the Bloch wave functions which correspond to the sublattice carbon atoms A and B :
$\psi = \phi_A + \lambda\phi_B$, where

$$\phi_j = \frac{1}{\sqrt{N}} \sum_n e^{i\vec{k}\vec{r}_{jn}} \chi(\vec{r} - \vec{r}_{jn}), \quad j = A, B. \tag{1.3}$$

N is the number of the unit cells, $\vec{r}_A$ and $\vec{r}_B$ are lattice translation vectors of A and B atoms respectively, $\chi(\vec{r})$ is the electron wave function of an isolated carbon atom. The summation is taken over all the atoms in the crystal of A and B sublattices. The coefficient λ can be found as follows. At first we substitute the given wave function

into the Schrödinger equation and multiply both sides of the equation by ϕ_A and ϕ_B. Upon integration we obtain the system of two equations :

$$\begin{pmatrix} H_{AA} & H_{AB} \\ H_{BA} & H_{BB} \end{pmatrix} \begin{pmatrix} 1 \\ \lambda \end{pmatrix} = \begin{pmatrix} ES_{AA} & ES_{AB} \\ ES_{BA} & ES_{BB} \end{pmatrix} \begin{pmatrix} 1 \\ \lambda \end{pmatrix}. \tag{1.4}$$

Here integrals $H_{ij} = \int \phi_i{}^* H \phi_j d\overrightarrow{r}$ and $S_{ij} = \int \phi_i{}^* \phi_j d\overrightarrow{r}$ $(i, j = A, B)$. Atoms on sublattices A and B are indistinguishable since their on-site energies are equal, so $H_{AA} = H_{BB}$ (it is only in case of broken symmetry between atoms A and B that $H_{AA} \neq H_{BB}$, this might take place in bilayer and trilayer graphene). Let's notice also that $H_{AB} = H_{BA}{}^*$. Within the tight-binding model $S_{AB} = S_{BA} = 0$ and the normalization condition of the wave functions imposes $S_{AA} = S_{BB} = 1$. Finally the solution for the equation (1.4) is

$$E = \frac{1}{2S}(H_{AA} + H_{BB} \pm \sqrt{(H_{AA} - H_{BB})^2 + 4|H_{AB}|^2}), \tag{1.5}$$

which can be simplified into the form

$$E = H_{AA} \pm |H_{AB}|. \tag{1.6}$$

Sign "+" corresponds to electrons and "−" to holes. The matrix elements H_{AA} and H_{AB} can be calculated by substituting the wave function (1.3) into the corresponding integrals and taking into account the coordinates of the nearest neighbours $\overrightarrow{\delta_1} = \frac{a}{2}(1, \sqrt{3})$, $\overrightarrow{\delta_2} = \frac{a}{2}(1, -\sqrt{3})$, $\overrightarrow{\delta_1} = a(-1, 0)$:

$$H_{AA} = \frac{1}{N} \sum_{A,A'} e^{-i\overrightarrow{k}(\overrightarrow{r}_A - \overrightarrow{r}_{A'})} \int \chi^*(\overrightarrow{r}_A - \overrightarrow{r}_{A'}) H \chi(\overrightarrow{r}_A - \overrightarrow{r}_{A'}) d\overrightarrow{r}, \tag{1.7}$$

$$H_{AB} = \frac{1}{N} \sum_{A,B} e^{-i\overrightarrow{k}(\overrightarrow{r}_A - \overrightarrow{r}_B)} \int \chi^*(\overrightarrow{r}_A - \overrightarrow{r}_B) H \chi(\overrightarrow{r}_A - \overrightarrow{r}_B) d\overrightarrow{r}. \tag{1.8}$$

Atoms of the same sublattice A' are separated from A by a translation vector (4.1). If we neglect next nearest neighbour hopping, i.e. $\gamma_0{}' = -\int \chi^*(\overrightarrow{r} - \overrightarrow{a}_{1(2)}) H \chi(\overrightarrow{r}) d\overrightarrow{r} = 0$, then $H_{AA} = E_0 = \int \chi^*(\overrightarrow{r}) H \chi(\overrightarrow{r}) d\overrightarrow{r}$, which is the on-site energy for the electrons and holes. Similarly H_{AB} can be written as

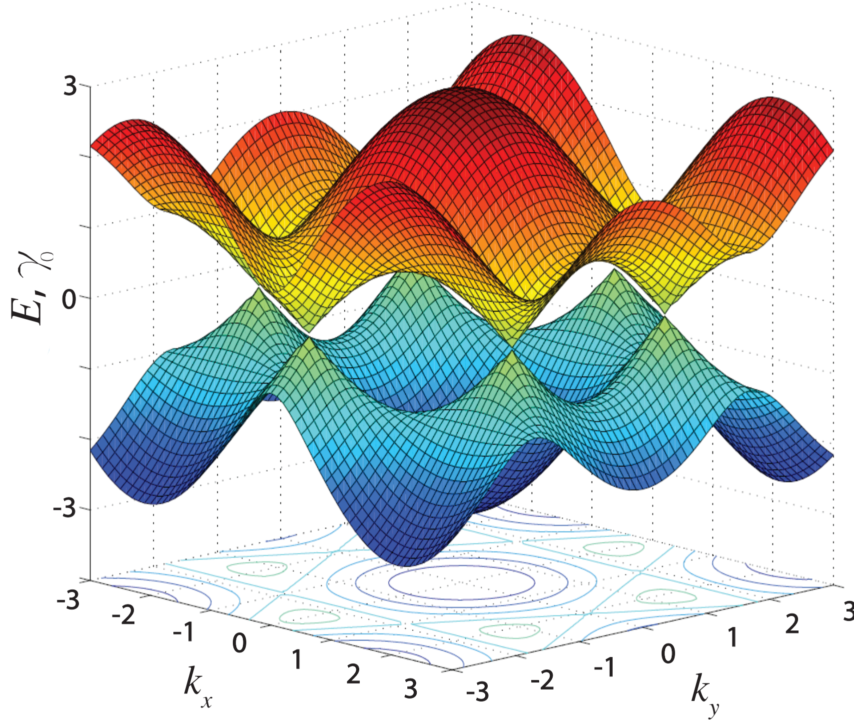

Figure 1.2: Graphene's energy dispersion.

$$H_{AB} = -\gamma_0(e^{-ik_xa} + 2\cos{(k_ya\sqrt{3}/2)}e^{ik_xa/2}), \tag{1.9}$$

where $\gamma_0 = \int \chi^*(\overrightarrow{r} - \overrightarrow{\delta}_{1(2,3)})H\chi(\overrightarrow{r})d\overrightarrow{r}$ is the hopping integral between nearest neighbours (from the *ab initio* calculations [3] $\gamma_0 \approx 2.8eV$ and $\gamma_0{}' \approx 0.02\gamma_0$). Hence the solution for energy is

$$E = E_0 \pm \gamma_0\sqrt{1 + 4\cos\frac{\sqrt{3}k_ya}{2}\cos\frac{3k_xa}{2} + 4\cos^2\frac{\sqrt{3}k_ya}{2}}. \tag{1.10}$$

The low-energy band structure is represented on the Fig. 1.2. There are two points in the first Brillouin zone (Fig. 1.1(b)) where conductance (π^*) and valence (π) bands are touching each other. In the vicinity of these K and K' points in k-space the spectrum is linear :

$$|E - E_0| = \pm\frac{3}{2}\gamma_0a|\overrightarrow{k} - \overrightarrow{k}_D|, \tag{1.11}$$

where $\overrightarrow{k}_D = \pm(\frac{4\pi}{3\sqrt{3}a}, 0)$ are the coordinates of K and K' points, also known as Dirac points due to linear shape of the energy spectrum (similar to Dirac relativistic particles). This property is unique to monolayer graphene and makes it easily-distinguishable from other 2-dimensional electron systems. Later experiments [4, 5]

demonstrated good agreement with this model.

In case when next nearest neigbour hopping is taken into account ($\gamma_0{}' \neq 0$) the $E(\overrightarrow{k})$ dependence will became asymmetric. It is also worth noticing that linear dispersion relation is valid at the energies $|E| \ll |\gamma_0|$, i.e. close to Fermi energy (for neutral system), which is usually set to zero.

In the representation of creation and annihilation operators the effective tight binding Hamiltonian, similar to (1.4), can be written as:

$$\widetilde{H} = \begin{pmatrix} 0 & -\gamma_0 \sum_{n=1}^{3} e^{i\overrightarrow{k}\overrightarrow{\delta}_n} \\ -\gamma_0 \sum_{n=1}^{3} e^{-i\overrightarrow{k}\overrightarrow{\delta}_n} & 0 \end{pmatrix}, \tag{1.12}$$

where $\widetilde{H}$ corresponds to the Hamiltonian in k-space. The expression (1.12) can be expanded near K and K' points (see coordinates of $\overrightarrow{k}_D$) in order to derive low-energy effective Hamiltonian, which will have the following form :

$$H^{K,K'} = -\gamma_0 \frac{3}{2} a \begin{pmatrix} 0 & \pm k_x - ik_y \\ \pm k_x + ik_y & 0 \end{pmatrix}. \tag{1.13}$$

This expression can be rewritten as

$$H = \hbar v_F (\alpha_1 k_x + \alpha_2 k_y), \tag{1.14}$$

where

$$\alpha_i = \begin{pmatrix} \sigma_i & 0 \\ 0 & -\sigma_i \end{pmatrix}, \tag{1.15}$$

and σ_i are Pauli matrices [6]. $v_f = 3a|\gamma_0|/2\hbar \approx 10^8 cm/s$ - the Fermi velocity [4]. Even though Pauli matrices are presented in Eq.(1.14), unlike in non-relativistic quantum mechanics they actually do not correspond to the real spin but rather pseudospin. They are attributed to the presence of two sublattices in the unit cell and refer to the different pseudospin projections, bringing the new concept in condensed matter physics.

Since in coordinate representation $k_x = -i\frac{\partial}{\partial x}$ and $k_y = -i\frac{\partial}{\partial y}$ the Hamiltonian for

one of the valley is then

$$H = \hbar v_F \begin{pmatrix} 0 & -i\frac{\partial}{\partial x} + \frac{\partial}{\partial y} \\ -i\frac{\partial}{\partial x} - \frac{\partial}{\partial y} & 0 \end{pmatrix}. \tag{1.16}$$

One can see the analogy with quantum electrodynamics (the equation (1.16) resembles one for relativistic Dirac particles), where v_F plays the role of the speed of light c. For this reason the touching points in the energy spectra are named Dirac points.

Introducing a two-component wave-function $\psi = (\chi_1, \chi_2)^T$ and substituting it into the Schrödinger equation gives us the system of differential equations :

$$\begin{cases} -i\hbar v_F(\frac{\partial \chi_2}{\partial x} + i\frac{\partial \chi_2}{\partial y}) = E\chi_1, \\ -i\hbar v_F(\frac{\partial \chi_1}{\partial x} - i\frac{\partial \chi_1}{\partial y}) = E\chi_2. \end{cases} \tag{1.17}$$

Substitution of χ_1 from the second equation of (1.17) into the first one gives us

$$\frac{\partial^2 \chi_1}{\partial x^2} + \frac{\partial^2 \chi_1}{\partial y^2} = -E^2 \chi_1 / \hbar v_F, \tag{1.18}$$

which has the solution $\chi_1 = (1/\sqrt{2}) \exp i(k_x x + k_y y)$ and together with the second equation (1.17) the final answer is

$$\chi_2 = \hbar v_F / (\sqrt{2}E)(k_x + ik_y)e^{i(k_x x + k_y y)} = \pm e^{i\theta}/\sqrt{2}e^{i(k_x x + k_y y)}. \tag{1.19}$$

Here we took into account linear dispersion relation (1.11). Sign "+"($-$) corresponds to electrons(holes) and $\theta = \arctan(k_y/k_x)$ introduce the phase. Thus two component wave function has the form :

$$\Psi = \frac{1}{\sqrt{2}} \begin{pmatrix} 1 \\ \pm e^{i\theta} \end{pmatrix} e^{ik_x x + ik_y y}. \tag{1.20}$$

1.3 Band structure of trilayer graphene

1.3.1 Introduction

When a single atomic layer of carbons is coupled to another one (or few) then a new electron system is formed which is called multilayer graphene (starting from bilayer).

π-orbitals in carbon atoms are responsible for this weak (compared to strong in-plane σ-bonds) interlayer bond [7]. For the given reason it is easy to separate thin graphene

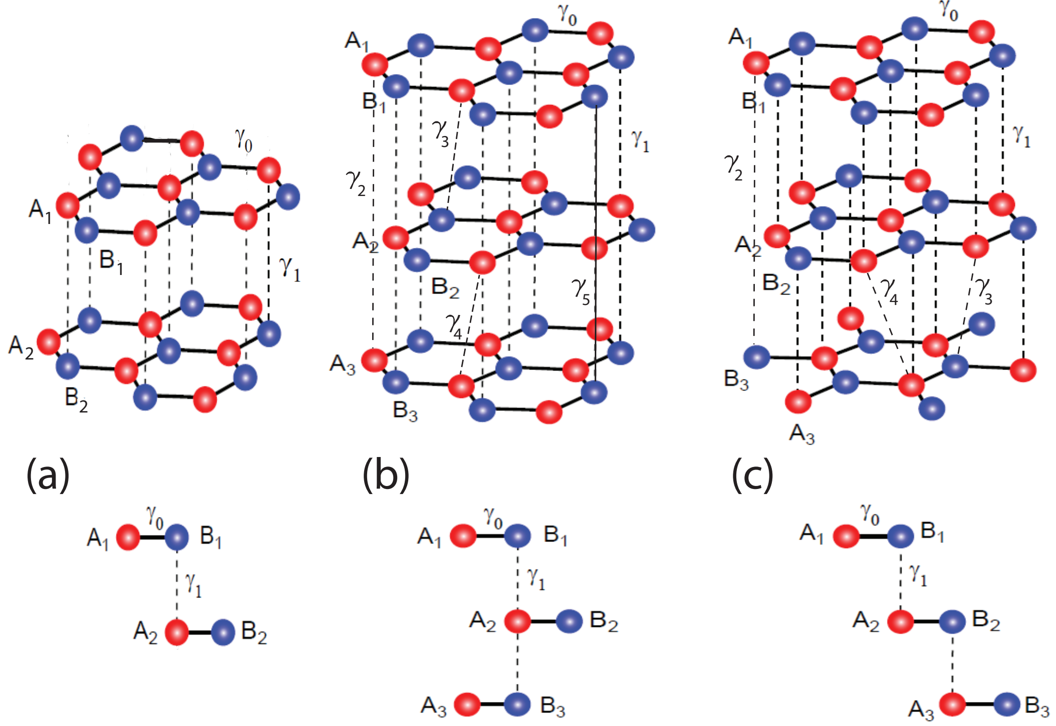

Figure 1.3: Schematic of atom arrangements in crystallographic structure of : (a),(b) Bernal-stacked bilayer and trilayer respectively, (c) rhombohedral trilayer. γ_0 and γ_1 are coupling constants.

flakes out of bulk graphite experimentally by mechanical exfoliation [1]. There might be several possibilities in arrangements of atoms of two sublattices A and B on different layers. Considering bilayer graphene, the most probable and energetically favourable stacking order is when A_1 atoms lay in the centre of hexagon with respect to the second layer and atoms B_1 coincide with the position of A_2, where 1 and 2 indices correspond to the top and bottom layer respectively (Fig. 1.3(a)). This stacking arrangement is known as AB- or Bernal- stacking and commonly takes place in graphite. However, recent experiments [8–10] reported twisted bilayer graphene - a different multilayer system, where one atomic plane was rotated with respect to another along the transversal axis, so the symmetry of the crystallographic structure was changed. Transport data (in particular Quantum Hall measurements [11]) revealed dissimilar behaviour compared to that in usual AB-bilayer.

Similarly, trilayer graphene thus far demonstrated two most thermodynamically stable layer arrangements : Bernal (also known as ABA) and rhombohedral (ABC)

trilayer [12]. From Fig.(1.3) one can see that multilayer systems with various stacking arrangements possess different types of symmetry. Bernal bilayer and ABC trilayer have inversion symmetry, whereas ABA trilayer has mirror symmetry plane. This mainly reflects a difference in band structure and thereby in transport properties of those electron systems.

In this section we will discuss the band-structure of trilayer graphene with two types of stacking order and show how it reflects their transport properties.

1.3.2 Bernal-stacked trilayer

In order to calculate the band structure of trilayer graphene one needs to consider sets of wave-functions, similar to Eq.(1.3), on each sublattice for all layers : $|\psi_{A1}\rangle, |\psi_{B1}\rangle, |\psi_{A2}\rangle, |\psi_{B2}\rangle, |\psi_{A3}\rangle, |\psi_{B3}\rangle$. Also it has to be taken into account coupling constants between sites for nearest atoms within one layer and in-between the layers as well. Following McCann [13], within the tight binding model the low-energy Hamiltonian at the K valley of ABA-stacked trilayer has the following form :

$$H_{ABA} = \begin{pmatrix} H_1 & V & & \\ V^\dagger & H_2 & V^\dagger & \\ & V & H_3 & V \end{pmatrix}, \tag{1.21}$$

where

$$H_i = \begin{pmatrix} U_i & v\pi^\dagger \\ v\pi & U_i \end{pmatrix}, \qquad V = \begin{pmatrix} -v_4\pi^\dagger & v_3\pi \\ \gamma_1 & -v_4\pi^\dagger \end{pmatrix}. \tag{1.22}$$

Here $\pi = \pm p_x + ip_y$ (signs "$\pm$" are for different valleys), U_i is the potential at the ith layer which is assumed to be uniform within the layer, $v = 3a\gamma_0/2\hbar$ is the band velocity of monolayer graphene. Other velocities are $v_3 = 3a\gamma_3/2\hbar$, $v_4 = 3a\gamma_4/2\hbar$. γ_0 and γ_1 are coupling constants between atoms shown on Fig.1.3, γ_3 referred to hopping between B_2 and A_1, γ_4 corresponds to hopping between B_1 and B_2 [7]. The hopping between next-nearest neighbouring layers γ_2 and γ_5 were not considered in (1.21).

Taking into account mirror reflection symmetry of the plane of the central layer (Fig.1.3(b)), the unitary transformation to a basis consisting of linear combinations of atomic wave-functions $(\psi_{A1} - \psi_{A3})/\sqrt{2}, (\psi_{A1} + \psi_{A3})/\sqrt{2}, (\psi_{B1} - \psi_{B3})/\sqrt{2}, \psi_{B2}, \psi_{A2}$ and

$(\psi_{B1} + \psi_{B3})/\sqrt{2}$ can be performed. If we do not allow for interlayer asymmetry $\Delta = (U_1 - U_3)/2$ (which can be realized in experiment by applying external perpendicular electric field) the new transformed effective Hamiltonian breaks into two parts :

$$\mathscr{H}_{ABA}{}^{eff} = \begin{pmatrix} H_m & \\ & H_b \end{pmatrix}, \tag{1.23}$$

where

$$H_m = \begin{pmatrix} 0 & v\pi^\dagger \\ v\pi & 0 \end{pmatrix}, \qquad H_b = \begin{pmatrix} 0 & \sqrt{2}v_3\pi & -\sqrt{2}v_4\pi^\dagger & v\pi^\dagger \\ \sqrt{2}v_3\pi^\dagger & 0 & v\pi & -\sqrt{2}v_4\pi \\ -\sqrt{2}v_4\pi & v\pi^\dagger & 0 & \sqrt{2}\gamma_1 \\ v\pi & -\sqrt{2}v_4\pi^\dagger & \sqrt{2}\gamma_1 & 0 \end{pmatrix}. \tag{1.24}$$

One of the parts, H_m, corresponds to monolayer-like Hamiltonian, another H_b is very similar to bilayer one, except some multipliers like $\sqrt{2}$. Indeed, considering only hopping terms γ_0, γ_1 gives us two bands at the K point (Fig.1.4(a)). One is the linear band and another has quadratic dispersion relation and correspond to bilayer.

Pioneer experimental work on trilayer graphene [14] demonstrated that Bernal-stacked one behaves as a semimetal and its band overlap is tuned with transversal electric field. Tight-binding calculations that includes parameters like γ_2 and γ_5 along with another hopping constants and taking into account interlayer asymmetry Δ gives us a slightly more complicated picture (Fig.1.4(c)). One can see that even with $\Delta = 0$ (Fig.1.4(b)) monolayer-like bands are no longer linear in the vicinity of K point; they split apart and are shifted up to higher energies.

In an applied external electric field, when $\Delta \neq 0$, the lower bands become hybridized with electron and hole branches not touching each other at the K point. The "linear" bands are shifted away from the Fermi level and their shapes resembles rather parabolic dependence. However, quadratic dependence for the energy dispersion relation in case of Bernal trilayer can be a good approximation when we are around Fermi energy :

$$E \approx \pm \frac{v^2 p^2}{\sqrt{2}\gamma_1}. \tag{1.25}$$

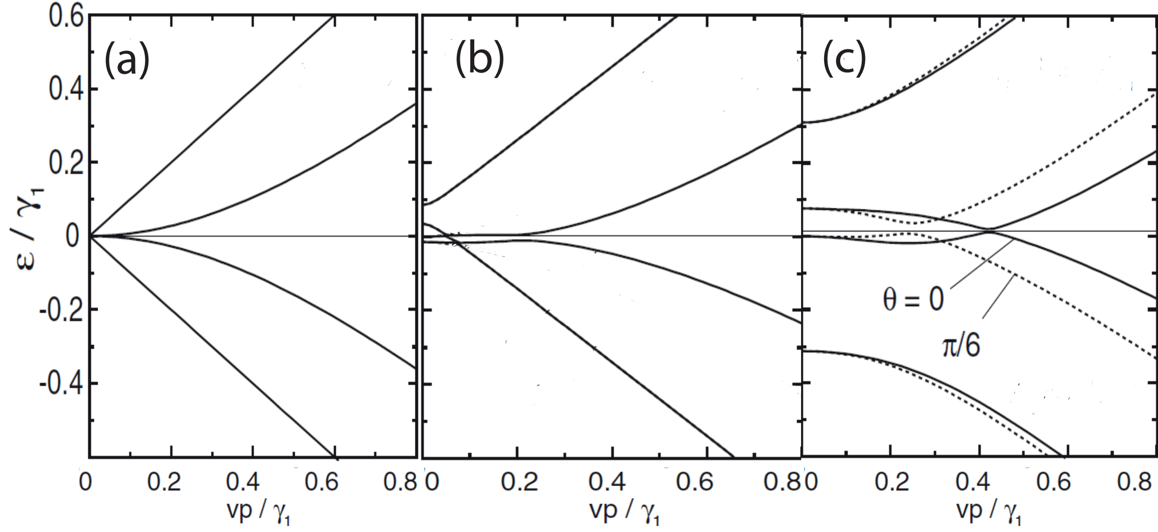

Figure 1.4: Band structure of ABA trilayer graphene near the K point : (a) calculation includes only γ_0 and γ_1, $\Delta = 0$; (b) γ_0, γ_1, γ_2, γ_3, γ_4 and γ_5 are considered, $\Delta = 0$; (c) same as be with $\Delta = 0.5\gamma_1$, $\theta = \tan^{-1}(p_y/p_x)$. Adapted from [13]

1.3.3 ABC-trilayer

As one may notice from the bottom part of Fig.1.3(c), due to the symmetry reasons, rhombohedral trilayer can not be simply represented as monolayer-like and bilayer-like parts. It will be demonstrated that due to a difference in coupling constants low-energy bands are not comparable with any of those discussed above. The main difference here with Bernal trilayer is the coupling γ_2 between two sublattices A and B on the outer layer which is absent in the former.

In a basis of atomic wave-functions $\psi_{A1}, \psi_{B1}, \psi_{A2}, \psi_{B2}, \psi_{A3}$ and ψ_{B3} the Hamiltonian for ABC-trilayer is [15]

$$H_{ABC} = \begin{pmatrix} D_1 & V & W \\ V^\dagger & D_2 & V \\ W^\dagger & V^\dagger & D_3 \end{pmatrix}. \tag{1.26}$$

Here

$$D_i = \begin{pmatrix} U_i & v\pi^\dagger \\ v\pi & U_i \end{pmatrix}, \qquad (i = 1, 2, 3) \tag{1.27}$$

$$V = \begin{pmatrix} -v_4\pi^\dagger & v_3\pi \\ \gamma_1 & -v_4\pi^\dagger \end{pmatrix}, \qquad W = \begin{pmatrix} 0 & \gamma_2 \\ 0 & 0 \end{pmatrix}, \tag{1.28}$$

where all parameters denoted in (1.27),(1.28) have the same form as described in

Sec.1.3.2, except the fact that now γ_2 introduces coupling not between the same sublattices on outer layers (A_1 and A_3) but rather between A_1 and B_3. In order to obtain dispersion relationship for low energies we derive an effective two-component Hamiltonian that describes hopping between A_1 and B_3. Let us denote $\chi_1 = (\psi_{B1}, \psi_{A2}, \psi_{B2}, \psi_{A3})^T$, $\chi_2 = (\psi_{A1}, \psi_{B3})^T$, H_{χ_2} and H_{χ_1} are the diagonal 2×2 and 4×4 blocks of (1.26) corresponding to χ_2 and χ_1 respectively, F is the off-diagonal 2×4 block coupling χ_2 and χ_1. All the parameters of the Hamiltonian (1.26) are treated to be small compared to interlayer coupling γ_1. Then the Schrödinger equation for χ_2 can be expanded in E as $[H_{\chi_2} - FH_{chi_1}^{-1}F^{\dagger}]\chi_2 = ES\chi_2$, where $S = 1 + FH_{\chi_1}^{-2}F^{\dagger}$. The effective Hamiltonian for $\tilde{\chi_2} = S^{1/2}\chi_2$ can be written as $H^{eff} \approx S^{-1/2}[H_{\chi_2} - FH_{\chi_1}^{-2}F^{\dagger}]S^{-1/2}$.

In a basis of $A_1 - B_3$ atomic sites the two-component effective Hamiltonian for ABC trilayer has now the form

$$\hat{H}_{ABC}^{eff} = \hat{H}_3 + \hat{H}_{3w} + \hat{H}_{3c} + \hat{H}_{\Delta}, \tag{1.29}$$

with

$$\hat{H}_3 = \frac{v^3}{\gamma_1^2} \begin{pmatrix} 0 & (\pi^{\dagger})^3 \\ \pi^3 & 0 \end{pmatrix}, \tag{1.30}$$

$$\hat{H}_{3w} = \left(-\frac{2vv_3p^2}{\gamma_1} + \frac{\gamma_2}{2} \right) \begin{pmatrix} 0 & 1 \\ 1 & 0 \end{pmatrix}, \tag{1.31}$$

$$\hat{H}_{3c} = \frac{2vv_4p^2}{\gamma_1} \begin{pmatrix} 1 & 0 \\ 0 & 1 \end{pmatrix}, \tag{1.32}$$

$$\hat{H}_{\Delta} = \Delta \left(1 - \frac{v^2p^2}{\gamma_1^2} \right) \begin{pmatrix} 1 & 0 \\ 0 & -1 \end{pmatrix}. \tag{1.33}$$

The term $\hat{H}_3$ describes hopping between A_1 and B_3 cites via other atomic cites that are coupled by γ_1. If we consider only this term it will give $E = \pm v^3p^3/\gamma_1^2$, which is a cubic dispersion. The second term $\hat{H}_{3w}$ is responsible for the trigonal warping (see next Subsection), $\hat{H}_{3c}$ introduces electron-hole asymmetry. The last term in (1.29) leads to opening a band gap around K point when the interlayer asymmetry between the outermost layers is finite ($\Delta \neq 0$).

By solving the secular equation $|\hat{H}_{ABC}^{eff} - E| = 0$ we find that the low-energy dis-

persion relation is

$$E \approx \pm\sqrt{f(p)^2 + 2\xi f(p)g(p)\cos(3\phi) + g(p)^2 + h(p)^2}, \tag{1.34}$$

where $\xi = \pm 1$ is the valley index, $f(p) = v^3p^3/\gamma_1^2$, $g(p) = \gamma_2/2 - 2vv_3p^2/\gamma_1$, $\phi = \tan^{-1}(p_y/p_x)$ and $h(p) = \Delta(1 - v^2p^2/\gamma_1^2)$. The energy dispersion relation for ABC trilayer is shown on Fig.1.5. When Δ is increasing the bands become hybridized producing Mexican hat-like shape. As one may see, close to zero energy level energy dispersion is not simply cubic, as was considered in [16, 17], but resembles rather the shape similar to monolayer graphene. The former is valid only for energies higher than $|\gamma_2|/2$, i.e. at higher carrier concentrations.

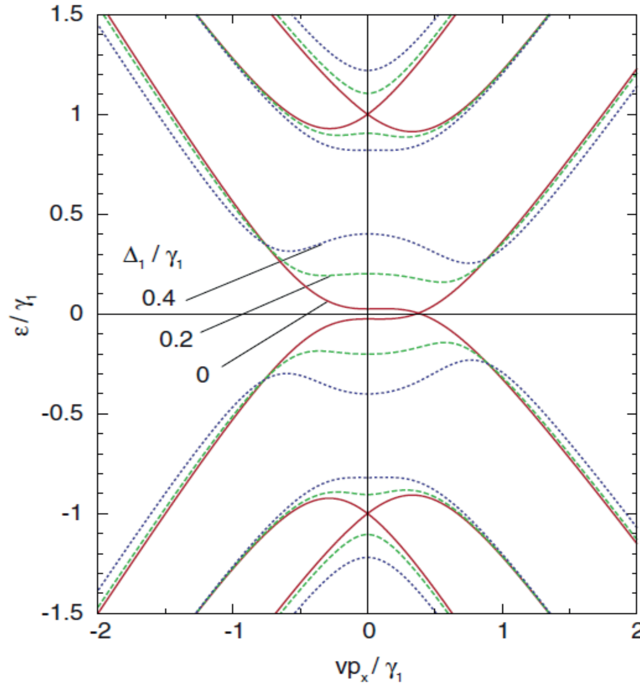

Figure 1.5: Band structure of ABC-stacked trilayer graphene around the K_+ point along p_x axis plotted for different values of interlayer asymmetry . Adapted from [15]

1.3.4 Lifshitz transition

From the previous section one may notice that the trigonal warping plays an important role in forming the low-energy electron-hole bands in ABC trilayer. Trigonal warping is a deformation of the Fermi surface around a degeneracy point in the first Brillouin zone [18]. In monolayer graphene, for example, it leads to modification of a conical

shape (in $(k_x, k_y, E)-$ space) to a tetrahedron-like shape with trigonal symmetry. For Bernal-stacked bilayer and ABC trilayer graphene the interlayer coupling enhances the trigonal warping and leads to much stronger effect, when the Fermi line about each K point is broken into several pockets [15, 19–21]. As a consequence of this,the equienergy surface undergoes the Lifshitz transition [22]. The Lifshitz transition is the change in the Fermi surface topology which occurs under continuous change of external parameters of the system, such as magnetic field, tension or doping.

Let's consider $E(p)$-dependence for ABC trilayer (1.34). In the absence of interlayer asymmetry the last term $h(p) = \Delta(1 - v^2p^2/\gamma_1^2)$ goes to zero and the expression now modifies to

$$E \approx \pm\sqrt{f(p)^2 + 2\xi f(p)g(p)\cos(3\phi) + g(p)^2}. \tag{1.35}$$

Trigonal symmetry in ϕ arises from acquired factor $e^{3i\xi\phi}$ that comes from $\hat{H}_3$ in

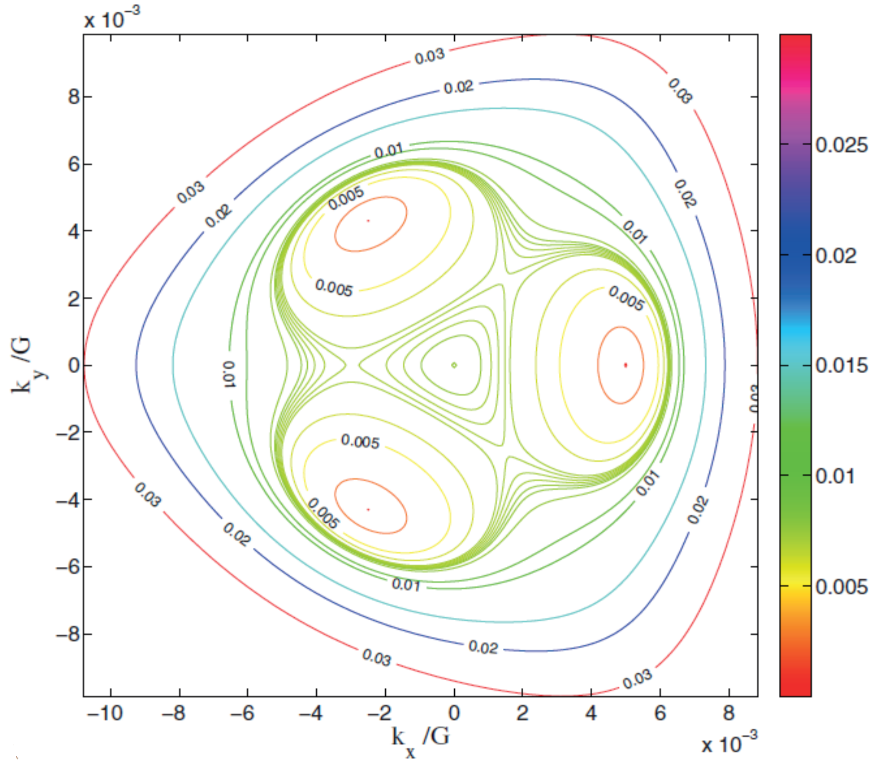

Figure 1.6: Constant energy contour plot of the conduction band near zero energy. The units of energy are eV. $G = 4\pi/(3a)$ is a reciprocal vector's length. Adapted from [23]

eq.(1.29) and a factor of 1 from $\hat{H}_{3w}$ when electrons are hopping from A_1 to B_3 cite. In two cases, when $\cos(3\phi) = 1$ and $g(p)$ is negative and when $\cos(3\phi) = -1$ and $g(p)$ is positive, the gap between conduction and valence band disappears. Because of

that in the neutral ABC trilayer the Fermi line splits into three similar pockets separated in direction by $2\pi/3$ from $k = 0$. The warping is significantly pronounced when $|g(p)| \sim f(p)$, that is at $p \sim (\gamma_1/v)(\gamma_2/2\gamma_1)^{1/3} - \gamma_1 v_3/(3v^2)$.

First, we consider low energy electron band (Fig.1.6). With the increase in carrier concentration, Fermi surface undergoes two Lifshitz transitions [23] (Fig.1.6, see also Fig.1.14(a)). As Fermi level reaches the first critical energy of about $6.7\,meV$, three electron pockets which initially had elliptical shape start to combine creating, thus, a central triangle-like pocket. The second transition starts at energy $7.2\,meV$. At this level the central pocket and three initially separated pockets merge into a single one, which has now smoothed and more pronounced triangle shape. It was calculated [23] that for low energy valence band those two transitions occur at the energies $-7.9\,meV$ and $-9.9\,meV$ respectively.

Unlike bilayer graphene, where constant energy surface has three remote pockets and one in the center around zero energy level, in rhombohedral trilayer there is no central pocket. The latter is missing because of the contribution of interlayer hopping γ_2 in $\hat{H}_{3w}$ that does not go to zero at $p = 0$. Also, the major difference from the bilayer is the energy level where the Lifshitz transition occurs. In bilayer graphene this happens at $E_{tr} \approx \gamma_1 (v_3/v)^2/4 \sim 1$, whereas for ABC trilayer this transition is estimated to be at $E_{tr} \approx |\gamma_2/2|$ which is roughly $10\,meV$. For this reason trigonal warping has greater effect on low-energy band structure in ABC trilayer. Nevertheless, Lifshitz transition is more pronounced in graphite than in trilayer due to larger hopping parameter γ_2 in the former. We will see later that broken degeneracy and, as a result, the appearance of the additional Quantum Hall plateaux (see Chapter5) can be a manifestation of the Lifshitz transition.

1.4 Band-gap engineering in graphene-based systems

1.4.1 Introduction

The absence of an energy gap in the the energy dispersion of graphene limits its potential application in logic circuits or photonic devices (the on-off current ratio in monolayer at room temperatures is < 10 [24]). Thus, engineering an energy gap in the

graphene spectrum is an open challenge.

Thus far, there are known three possible solutions of this problem. The first one is to create nanoconstrictions in graphene, like nanoribbons with armchair edges [25]. Those devices revealed the energy gap depends on the width of the constriction. The second suggestion was to chemically functionalize graphene, for instance fluorographene [26], where the functionalization with fluorine adatoms leads to sp^3-hybridization. Fluorine atoms are situated on opposite sides of graphene plane for different sublattices. This, in turn, brings the difference to onsite energies of atoms on two sublattices A and B, and changes the energy spectrum around Dirac point (see Section1). Experiments on fluorographene revealed an energy gap $\sim 68meV$ [27].

These two techniques allow to open relatively high band-gap. However both nanoribbons and chemically functionalized graphene are still highly disordered. This means that electron transport at higher temperatures will take place via hopping conduction mechanism and the charge carrier mobility will diminish appreciably. The alternative to the aforementioned solutions is to deal with multilayer graphene samples that possess inversion symmetry in their crystallographic structure, for example AB bilayer. The theory predicted electric field dependent energy gap for such systems [15, 28, 29]. Also, theoretical expectation for the energy gap was very inspiring - up to 300 meV in ABC trilayer [30]. Since an intrinsic mobility in these devices is still high, the latter approach makes them very promising for further applications in transistor electronics.

1.4.2 Symmetry breaking and the role of screening in multilayer devices

As was shown previously, Bernal bilayer and rhombohedral trilayer have the same type of symmetry. This symmetry can be broken when the potential difference between top and bottom layers is non zero. This can be realized experimentally in two possible ways : external doping of the top layer or application of transversal electric field. When inverse symmetry is broken the energy gap appears in the spectrum of AB bilayer or ABC multilayers. The contribution of the screening effect to the gap dependence on electric field in these systems is essential, especially for rhombohedral stacked graphene with $N > 3$ (N is the layers number). For this reason experimentally observed values

of the gap in bilayer and trilayer, when applied electric field was comparable, were roughly the same despite expectations of bigger values for the latter [31, 32].

Considering multilayer graphene as a set of parallel plates with zero thickness, one can calculate self consistently electron densities n_j and layer potentials U_j (j = 1,2,3...) knowing the strength of external field F_0. The density difference between top and bottom layers causes the screening field that is opposite to the external F_0. The latter is taken into account and giving the expression for the potential difference [30] (self-consistent equation):

$$\Delta U = U_1 - U_N = e(N-1)d\left(F_0 - \frac{e}{2\epsilon}\frac{g_v g_s}{2\pi}\left(\frac{\gamma_1}{\hbar v}\right)^2\left(\frac{\Delta U}{2\gamma_1}\right)^{2/N} f_N\right). \tag{1.36}$$

Here ϵ is the permittivity of graphene, $g_s = g_v = 2$, and f_N depends only on N. When $N \geq 3$, ΔU become much smaller than $\Delta U^{2/N}$, if the former is not high, f_N is approximately 1/2 and the eq.1.36 can be solved as follows:

$$\Delta U \approx 2\gamma_1 F_0^{N/2}\left[\frac{1}{2}\frac{e}{2\epsilon}\frac{g_v g_s}{2\pi}\left(\frac{\gamma_1}{\hbar v}\right)^2\right]. \tag{1.37}$$

Remarkably, the influence of screening becomes more enhanced with increasing the number of layers. Up to certain value of electric field the energy gap is bigger in trilayer than in bilayer. However, there is an existence of a "saturation point", after which further increase of external field leads to reduction of the band-gap due to considerable impact of the screening field. The estimated characteristic carrier density associated with this value of saturation point for external field is $n_c \approx 1.2 \times 10^{13}$ cm^{-2} [30].

1.4.3 Related experiments

Until now, there were several experiments verifying the opening of an energy gap in ABC trilayer with transversal electric field. In Ref. [32] infrared absorption experiment showed the splitting of the optical conductivity peak, measured as a function of photon energy, into two separate ones. By measuring the energy difference between two peaks for given external fields the values of energy gap were extracted (Fig.1.7(b)). The experimental setup is shown on the inset of Fig.1.7(b) - electrolytic polymer was used as the top gate and the only source of the field. The electron transitions are shown on Fig.1.7(a) where the difference in energies between transitions "1" and "2" was

detected. This transitions occured when the Fermi level was above the band-gap. With this experimental setup it was very difficult to probe the size of energy gap at lower fields, since electrolytic gate enabled sharp increase of carrier concentration with only small change in the applied gate.

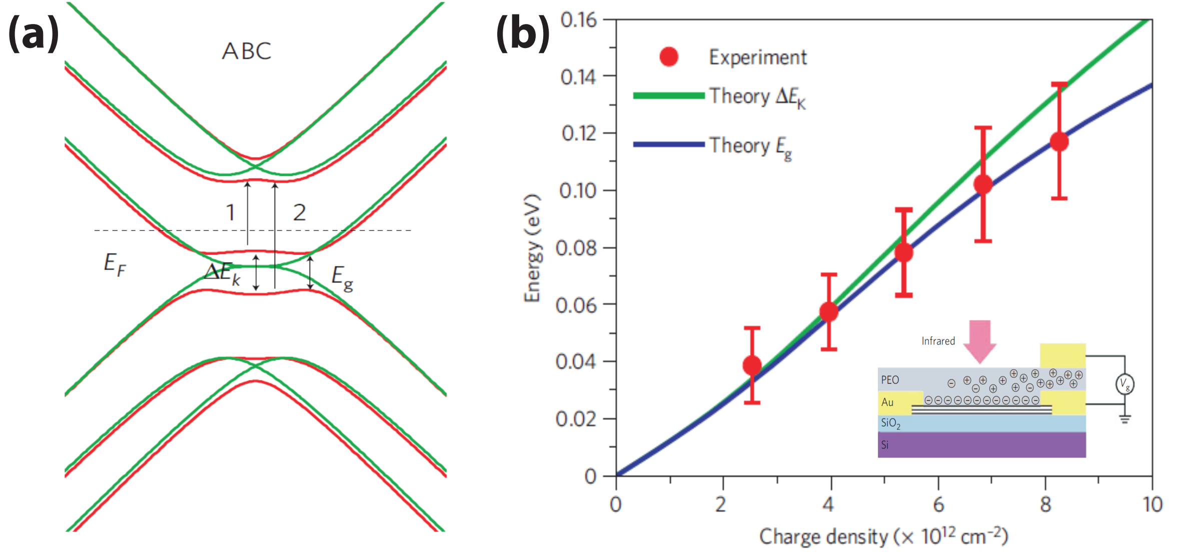

Figure 1.7: Adapted from [32]:(a)The band structure of ABC trilayer graphene with (red) and without (green) the presence of a perpendicular electric field, calculated within the tight binding model. Transitions 1 and 2 are the strongest optical transitions near the K-point for electron doping. Inset: schematic representation of the trilayer device used in experiment. (b) Energy gap as a function of carrier concentration. The symbols are experimental data and the solid lines are the results of the TB model for ΔE_K(green) and E_g(blue), as indicated in (a).

S.Jhang *et.al.* [33] observed the increase of the resistance at the neutrality point with increasing applied top-gate voltages, indicating opening of an energy gap in ABC trilayer. This experiment was performed with the double gated samples on top of SiO_2 where top gate was gold electrode separated with Al_xO_y layer. There was no attempts to extract values of energy gap however.

In 2011 C.N. Lau [16] reported the energy gap of the value ~ 6 meV in suspended rhombohedral trilayer graphene at zero electric field. This result was not expected according to theory and was explained by spontaneous symmetry breaking due to strong electronic interactions.

To summarize, we note that due to lack of experiments there were no direct evidence of tunable band-gap in ABC trilayer graphene, leaving this problem yet unsolved. We address this question to the detailed analysis in Chapter4.

1.5 Properties of 2D graphene based structures

1.5.1 Density of states

The density of states (DOS) is the number of states per unit energy and per unit volume :

$$D(E) = \frac{dN_{st}}{VdE} = g\frac{VdV_k}{V\,(2\pi\hbar)^\rho\,dk|dE/dk|} = g\frac{dV_k}{(2\pi\hbar)^\rho\,dk}\mid\frac{dk}{dE}\mid, \tag{1.38}$$

where N_{st} is the total number of states containing the degeneracy factor g, volumes V and V_k in real and $k-$space respectively and a phase volume per state $(2\pi\hbar)^\rho$, with ρ denoting the dimension of the system. In a two-dimensional case $V_k = \pi(\hbar k)^2$ and $\rho = 2$. For a conventional 2DEG with parabolic energy dispersion relation $E = \hbar^2 k^2/(2m^*)$, where m^* is the effective mass of the charge carriers, DOS is constant $D(E) = g2\pi\hbar^2 kdk/(4\pi^2\hbar^2 dk\hbar^2 k(m^*)^{-1}) = gm^*/(2\pi\hbar^2)$ (Fig.1.8(a)). If we consider monolayer graphene, linear $E(k)-$dependence leads to $|dE/dk| = \hbar v_F$ and thus to linear DOS $D(E) = gE/(2\pi\hbar^2 v_F^2)$ with $g = g_s g_v = 4$ due to spin and valley degeneracy. In the simplified model for the N-layer case system [23] the DOS can be represented as: $D(E) \sim E^{(2-N)/N}$. One may see that the DOS for $N > 2$, like in ABC trilayer (when $E \geq 7\,meV$) $E(k) \sim k^3$, diverges as E approaches to zero (Fig.1.8(c)). The carrier concentration at low temperatures can be calculated for two-dimensional systems using their DOS :

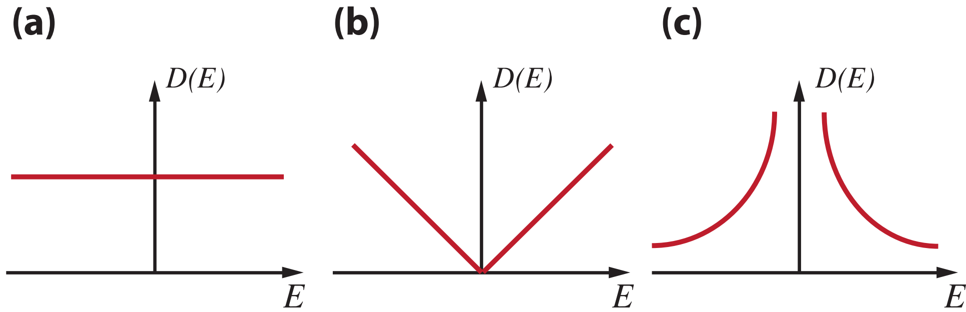

Figure 1.8: The schematic of the density of states as a function of energy for : (a)conventional 2DEG, (b) monolayer graphene, (c) multilayer graphene with N> 2

$$n_e = \int_0^{E_F} D(E)f(E)dE \approx \frac{g}{2\pi}\int_0^{E_F} k\frac{dk}{dE}dE, \tag{1.39}$$

where $f(E)$ is the Fermi-Dirac distribution, which is simply a unity when $T \approx 0$, E_F is the Fermi energy. Thus for monolayer graphene one can find $n_e = E_F^2/(\pi\hbar^2 v_F^2)$, so $E_F = \hbar v_F\sqrt{\pi n_e}$. Similarly, for bilayer graphene $E_F = \pi\hbar^2 n_e/(2m^*)$, and ABC trilayer

$E_F = (4\pi)^{3/2}\, v_0^3 \hbar^3 n_e^{3/2} / \gamma_1^2$.

It is worth pointing out interesting fact that depending on number of layers in graphene, we deal with different types of particles : in monolayer graphene, for instance, the transport is carried out by massless particles, the effective mass of bilayer graphene, nevertheless, is constant ($m^* \approx 0.035 m_e$, where m_e is the mass of electron) and is energy independent. In case of ABC trilayer, since $m^* = p\,(\partial E/\partial p)^{-1} \sim E^{-1/3}$, we have an energy dependent effective mass [17], which is divergent once $E > E_{Lif}$ (E_{Lif} is the energy of the Lifshitz transition).

Let's consider low energy DOS in ABC trilayer in a range below the Lifshitz transition. To calculate the density of states one needs to solve first the secular equation with $\hat{H}^{eff}_{ABC}$ from (1.29), but neglecting the higher order cubic term (1.30). In this case the energy dispersion becomes

$$E \approx \frac{2vv_4p^2}{\gamma_1} \pm \sqrt{(\Delta^2 + \frac{\gamma_2^2}{4}) - 2v\frac{p^2}{\gamma_1^2}(\Delta^2 v + v_3\gamma_1\gamma_2) + \frac{v^2p^4}{\gamma_1^4}(4v_3^2\gamma_1^2 + \Delta^2 v^2)}, \quad (1.40)$$

and when $E \ll E_{Lif}$ it can be written as $E \approx \pm\sqrt{\alpha_1 + \alpha_2 p^2 + \alpha_3 p^4}$, where parameters $\alpha_1, \alpha_2, \alpha_3$ are the corresponding terms in (1.40) at 1, p^2 and p^4 respectively. Thus the DOS for low energy range can be written as

$$D(E) \sim \frac{E}{\sqrt{1 + \beta E^2}}. \quad (1.41)$$

The parameter β consists of other parameters in Eq.(1.40) (including interlayer asymmetry Δ) and is nothing but constant.

1.5.2 Berry's phase

Another important characteristic of graphene-based 2D materials that distinguishes them out of other electronic systems is the Berry's phase [34]. Berry's phase (also known as geometric phase) is a phase of the wave-function acquired over a cycle, when the system is subjected to cyclic adiabatic processes. This phase is the result of the geometrical properties of the parameter space of the Hamiltonian.

If we apply the gauge transformation for the two-component wave-function around

K point, Eq.(1.20), the latter will modify into

$$\Psi = \frac{1}{\sqrt{2}} \begin{pmatrix} e^{-i\theta/2} \\ e^{i\theta/2} \end{pmatrix} e^{i\vec{k}\vec{r}}. \tag{1.42}$$

When an electron in graphene completes the full circle, the acquired shift in the phase factor is $\phi = 2\pi$. Thus, electron wave-function will be

$$\Psi \to \frac{1}{\sqrt{2}} \begin{pmatrix} e^{-i(\theta+2\pi)/2} \\ e^{i(\theta+2\pi)/2} \end{pmatrix} e^{i\vec{k}\vec{r}} \to \Psi \begin{pmatrix} e^{-i\pi} \\ e^{i\pi} \end{pmatrix}. \tag{1.43}$$

The phase change of the wave-function is the factor of π, which is the Berry's phase.

Berry's phase plays an important role in many quantum phenomena of graphene-based systems. In a monolayer, for example, when an electron approaches the scattering potential at an incident angle being $\alpha = m\pi$, $(m = 0, 1, 2...)$, i.e. normally to the boundary, due to additional factor in the wave-function attributed to the geometrical phase the transmission coefficient through this barrier equals one (Klein paradox [35]). The result was shown to be independent on the shape and the width of the potential barrier [36]. This explains the effect of suppression of the backscattering for massless Dirac particles.

Related to the multilayer graphene, the influence of the geometrical phase is crucial in the trigonal warping and, in particular, in the Lifshitz transition. When an electron is hopping from A_1 to B_3 cite in ABC trilayer graphene it acquires a factor $e^{3i\xi\phi}$ ($\xi = \pm 1$ is the valley index) in the wave-function. For this reason, around zero level, constant energy lines possess trigonal symmetry ($\cos 3\pi$ term in eq.1.35 contributes mainly). This symmetry is also present in bilayer graphene, but in this case there is a central pocket at $p = 0$ and related to it an additional contribution $e^{-i\xi\phi}$. One may say that the total geometrical phase integrated around the equienergy line should be conserved at the Lifshitz transition. Indeed, bilayer and ABC trilayer graphene are considered as systems with the Berry's phases of 2π and 3π respectively [15, 19]. Hence, in trilayer graphene the geometrical phase that is integrated around the constant energy line in each pocket is $\xi\pi$, like in single layer graphene, giving in total $3\xi\pi$. Whereas in bilayer graphene, the contribution of three remote pockets gives $3\xi\pi$, but the central pocket contributes with $-\xi\pi$ factor, thus giving us $2\xi\pi$.

From the semiclassical point of view the acquired geometrical phase in the momentum space can explain the shifts in Shubnikov-de-Haas (SdH) resistance oscillations [37, 38] (ρ_{xx} as a function of B) and related to this the unconventional sequence of the plateaux of Hall conductivity σ_{xy} and additional degeneracy factors of zeros Landau level in bilayer [39, 40] and trilayer [15, 17] graphene samples. Further, we refer this to the section about Quantum Hall Effect in graphene.

1.6 Quantum Hall Effect in 2DEG systems

1.6.1 Introduction

Quantum Hall Effect (QHE), firstly discovered by Klaus von Klitzing [41] in metal-oxide-semiconductor field-effect-transistor (MOSFET) in 1980, is one of the most astonishing quantum phenomenon in condensed matter physics. It was measured in 2DEG at strong magnetic field and low temperature and disclosed quantum nature in confined systems.

To bring main concepts for understanding Quantum Hall Effect in two dimensional electron gases we start first from the consideration of the classical case. Then we will consider the formation of energy levels in a presence of magnetic field in two-dimensional systems including graphene. The theoretical expectations and recent experimental results of QHE in graphene samples will be discussed.

1.6.2 Classical Hall Effect

In the presence of a perpendicular magnetic field the electrons, moving with the velocity $\overrightarrow{v}$, are subjected to Lorenzian force $\overrightarrow{F}_M = -e\left[\overrightarrow{v} \times \overrightarrow{B}\right]$ and their trajectories are bended. Here e is the absolute value of the electron charge. Under this force electrons start to move along the cyclotron orbits with the radius $r_c = m_e|v|/(eB)$ and with the cyclotron frequency $\omega_c = eB/m_e$, where m_e is the electron mass. In the sample (Fig.1.9), when electric field is applied, current flows from the source to drain contact introducing the net external force $\overrightarrow{F} = \overrightarrow{F}_M + \overrightarrow{F}_E$, with $\overrightarrow{F}_E = -e\overrightarrow{E}$. The drift velocity has X and Y components governed respectively by electric ($\overrightarrow{F}_E$) and magnetic ($\overrightarrow{F}_M$) forces. Substitution of the total external force into the equation of motion when the system is at the equilibrium ($d\vec{p}/dt = 0$) and taking into account the scattering,

leads to the following expression for electric field components :

$$\begin{cases} E_x = \dfrac{m_e j_x}{ne^2\tau} + \dfrac{B j_y}{en}, \\ E_y = \dfrac{m_e j_y}{ne^2\tau} - \dfrac{B j_x}{en}, \end{cases} \tag{1.44}$$

where τ is a characteristic relaxation time due to scattering of electrons on the imperfections.

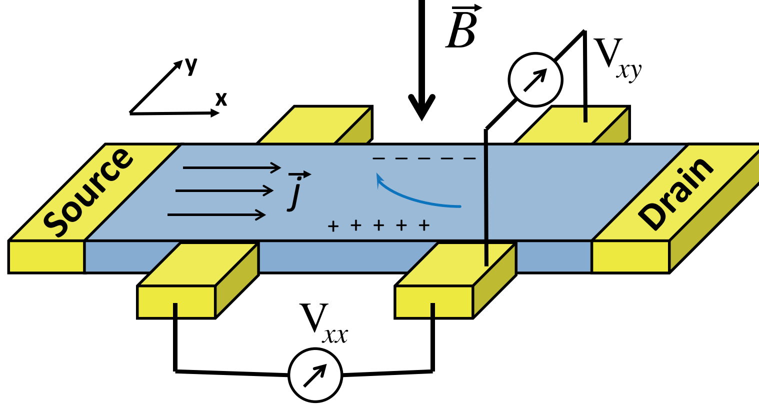

Figure 1.9: The schematic of the circuit for Hall Effect measurements. Black arrows along the sample indicate the current flow $\vec{\jmath}$ from the source to drain. The blue arrow shows the bend of the trajectories in the presence of a perpendicular magnetic field $\vec{B}$. Pluses/minuses signs at the edges demonstrate the negative/positive charge accumulation. V$_{xx}$(V$_{xy}$) is the voltage along(across) the sample.

In equilibrium $\vec{F}_M$ is compensated by $\vec{F}_E$, since the current flow in Y direction is zero ($j_y = 0$). Considering the relation between electric field and the resistivity $E_i = \rho_{ij} j_j$ we obtain main expression for classical Hall effect :

$$\begin{aligned} \rho_{xx} &= \frac{m_e}{ne^2\tau}, \\ \rho_{xy} &= \frac{B}{en}, \end{aligned} \tag{1.45}$$

where $\rho_{xy} = -\rho_{yx}$.

The voltage drop across the sample is $V_{yx} = -\dfrac{B}{end} I_x$, called Hall voltage, depends linearly on magnetic field, where d is the depth of the sample. There are two major keys in the eq.(1.45) that correspond to classical case : longitudinal resistivity ρ_{xx} is constant and does not depend on external fields, and transversal component ρ_{xy} is proportional to magnetic field with the coefficient (known as Hall coefficient R_H) that depends only on the carrier concentration. However, for confined two-dimensional system this does

not take place and both components of the resistivity become quantized with magnetic field.

1.6.3 QHE in 2DEG

The behavior of electrons in external magnetic field must be described using the language of quantum mechanics which requires solving of the Schrödinger equation :

$$\frac{1}{2m_e}\left(\hat{p}-e\vec{A}\right)^2\Psi(\vec{r}) = E\Psi(\vec{r}), \tag{1.46}$$

where $\vec{A}$ is the vector potential so that $\vec{B} = \vec{\nabla}\times\vec{A}$.

For the particles confined in $x-y$ plane the solution of eq.(1.46) is well known [42] and leads to the quantized energy levels:

$$E = \hbar\omega_c\left(N+\frac{1}{2}\right), \quad N = 0, 1, 2, ... \tag{1.47}$$

As one may see in a magnetic field the DOS is a set of $\delta-$functions separated in energy space by $\hbar\omega_c$ (Fig.1.10) (note that spin was not taken into consideration in eq.(1.46)). This is in sharp contrast with the DOS of 2DEG with parabolic energy dispersion relation (Fig.1.8(a)), discussed earlier. Here the energy levels (also called Landau levels) do not depend on $k-$vector.

For the given spectrum the electronic states are now accommodated on Landau levels (LL) and thus degenerate [42]. In the real sample that have finite sizes L_x and L_y the degeneracy factor for each LL is $N_L = \dfrac{L_xL_yeB}{2\pi\hbar}$. The number of occupied LL - the filling factor ν - is the total number of electrons divided by the number of states in LL:

$$\nu = \frac{N_e}{N_L} = \frac{2\pi\hbar N_e}{eBL_xL_y} = \frac{n_e}{B}\phi_0, \tag{1.48}$$

where n_e is electron density and $\phi_0 = h/e$ is the magnetic flux quanta.

The situation described above with the series of $\delta-$functions is the ideal case, since we did not consider the disorder which is the key point in the nature of Quantum Hall Effect. In the presence of disorder Landau levels become broadened. The width of the broadening can be estimated as $\Gamma \sim \hbar/\tau_0$, where τ_0 is the characteristic scattering time. The condition for LL to be well-resolved is then $\hbar\omega_c \gg \hbar/\tau_0$. The picture for the DOS in disordered system (Fig.1.10) now looks different. There are two regions :

localized states at the tales of the Landau subbands and delocalized (extended) states in the middle of the distribution. When the Fermi energy lies in-between extended states, the transversal resistivity has constant value which depends on the number of filled LL $\rho_{xy} = h/(\nu e^2)$ ($\nu = 1, 2, 3...$), whereas longitudinal resistivity ρ_{xx} drops to zero revealing the dissipation less transport.

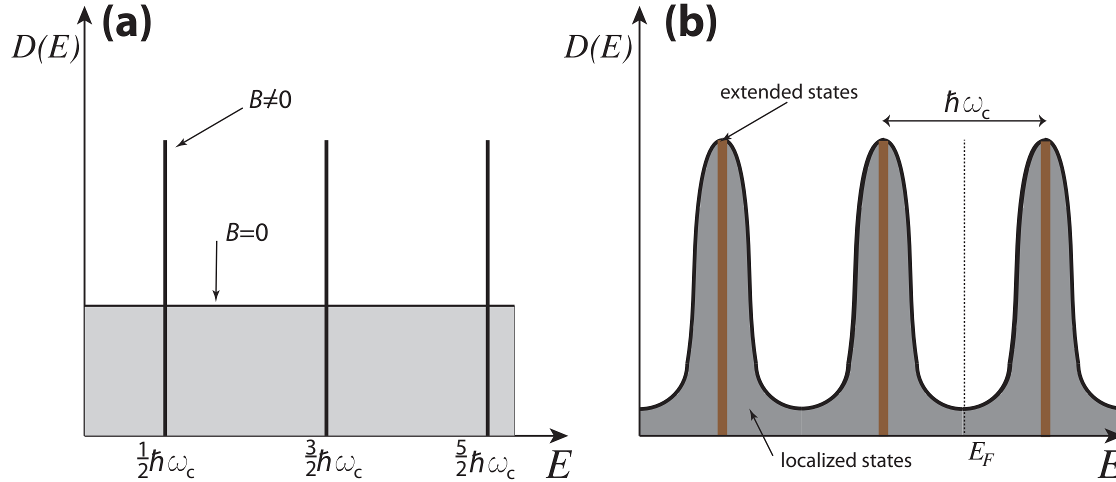

Figure 1.10: (a) The density of states for the particles in magnetic field when the disorder and the spin is not taken into account. For comparison the shaded area shows the DOS when magnetic field is zero. (b) The schematics of the DOS of Landau levels for the real sample in the presence of disorder. Two regions of localized and extended states are labeled .The dashed line is the position of the Fermi level.

To understand this, one need to employ the concept of edge states [43]. These states are analogous to 1D channels where charge carriers can propagate along them without being scattered. As the size of the sample is finite, the energy of Landau levels rise up near the boundary of the sample due to confining potential (Fig.1.11(c)): $E' = E_N + U(x)$, where E_N are the energy levels from (1.47) and $U(x)$ is the potential energy. When the Fermi level is located between the extended states then there are certain amount of LL that are occupied and there is no carrier transport through the bulk. However the extended states exist at the edges of the sample due to bending of the energy levels [44].

Consider 2DEG with bottom and top electrodes attached to the sample with chemical potentials μ_1 and μ_2 respectively, such that $\mu_1 > \mu_2$. Suppose, the Fermi level is situated between two Landau subbands in the bulk. Electrons in the left edge states flow from the bottom to the top electrode and in the opposite way in the right edge states. So the states in the left edge channels are occupied up to μ_1 and those in the

right edge channel up to μ_2 (see the direction of the current flow on Fig.1.11(b)). One may calculate the total current carried by electrons through these edge channel. In a two-dimensional device with the confining potential, that is assumed to be smooth along the sample (in $y-$direction) the Hamiltonian can be written as

$$H = \frac{1}{2m_e}\left[p_x^2 + (p_y - eBx)^2\right] + U(x). \tag{1.49}$$

The contribution to the current density of an electron in a channel is $j_y = (e/L_y)v_y$, where the velocity can be calculated as follows :

$$\begin{aligned} v_y &= \langle\psi(x,y)|\frac{1}{m_e}\left(p_y - eBx\right)|\psi(x,y)\rangle = \langle\phi(x)|\frac{1}{m_e}\left(eBx_0 - eBx\right)|\phi(x)\rangle \\ &= \frac{1}{eB}\langle\phi(x)|\frac{\partial H}{\partial x_0}|\phi(x)\rangle = \frac{1}{eB}\frac{\partial}{\partial x_0}E(x_0). \end{aligned} \tag{1.50}$$

Where $x_0 = p_y/(eB)$. In order to find the current per Landau level flowing in one direction, say in the left edge, we need to calculate the contribution of all the electrons with energies up to μ_1 over all x_0 that satisfy the condition $E_F < E(x_0) < \mu_1$. Thus we have

$$I_1 = \sum_{x_0}\frac{e}{L_y}v_y = \frac{L_y eB}{h}\int dx_0\frac{ev_y}{L_y} = \frac{e}{h}\int\limits_{E_F<E(x_0)<\mu_1}\frac{dE}{dx_0}dx_0 = \frac{e}{h}(\mu_1 - E_F). \tag{1.51}$$

Similarly $I_2 = \dfrac{e}{h}(\mu_2 - E_F)$. The net current is $I = I_1 - I_2$. Since the voltage drop between the edge states is $V = (\mu_1 - \mu_2)/e$, the final expression for the total current per LL is

$$I = \frac{e}{h}(\mu_1 - \mu_2) = \frac{e^2}{h}V. \tag{1.52}$$

Hence in a Quantum Hall regime the transversal conductivity is quantized $\sigma_{xy} = (e^2/h)\nu$. As described above, ν is the number of occupied Landau levels, which is nothing but the number of the edge channels participating in transport.

There is qualitative explanation to obtained result. The electron wave-function is extended over the distance that is typically an order of magnetic length $l_B = \sqrt{\hbar/eB}$. This length can characterize the width of the edge channel and at strong B magnetic length become small (an order of 10 nm at 1 T), so that each edge state can be considered as a 1D channel. Assume the Fermi level lies between delocalized states,

thus all Landau levels below this energy are populated. In this case all the states in the bulk are occupied, and unoccupied ones exist only at the edges of the sample (see Fig.1.11(c)). When the electron is moving along the edge it can not be scattered back, because the only available state for scattering with the conservation of momentum is the edge state at the opposite side of the sample, where $\vec{k}$ has a different sign. However, at high magnetic field the wave-functions of the edge states at opposite boundaries do not overlap due to their exponential decay on the distance of magnetic length, which is significantly small compared to the width of a real sample ($L_x \gg l_B$). Thus, the aforementioned states are spatially separated over the large distance. For this reason the backscattering is strongly suppressed, allowing ballistic transport of the charge carriers along the edge channels. The former explains the drop of the longitudinal resistivity ρ_{xx} almost to zero and distinctively flat plateaus in the transversal resistivity

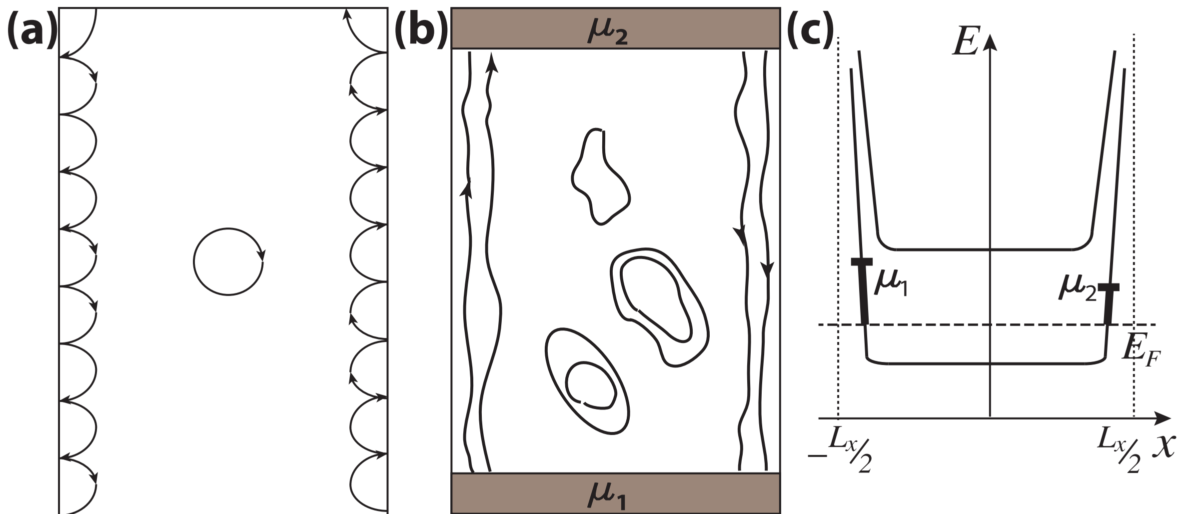

Figure 1.11: (a) A semiclassical view of the skipping orbits. (b) The schematic picture of two-terminal sample with chemical potentials μ_1 and μ_2 of the electrodes. The loops and curly lines demonstrates the equipotential line pattern of localized (in the middle) and extended (edge) states respectively determined by disorder. Black arrows indicate the current direction along the edge channels .(c) The energy landscape of the LL in the direction across the sample. The dashed line shows the position of the Fermi level.

ρ_{xy}. When the Fermi energy crosses a Landau level, more states become available for an electron to be scattered back. This, in turn, leads to finite longitudinal resistivity and raises the Hall resistivity by increasing the filling factor ν. This picture can be also understood from the semi-classical point of view. In the sample all electrons move along enclosed cyclotron orbits with the radius $r_c = m_e|v|/(eB)$ and there is no net drift in the bulk of the sample when the disorder is present. Nevertheless, at the edges

the situation is different, where electrons recoil from the boundary and continue moving along the side forming so-called skipping orbits(see Fig.1.11(a)). Even if an electron faces an impurity close to the edge, its scattered orbit is never further away from the edge then the cyclotron radius, which become smaller as the magnetic field increases. These semi-classical skipping orbits might be considered as an analogue of the edge states.

1.6.4 LLs in graphene

The formation of energy levels in magnetic field (eq.1.47) for 2DEG systems allowed for parabolic energy dispersion is not the same for single layer graphene. Moreover, we will see that not only the dispersion relation, but the presence of two valleys in the BZ is also crucial and bring the difference into Quantum Hall nature of graphene samples with unconventional quantization sequence.

We start from the consideration of the Schrödinger equation with the Hamiltonian (1.16). In magnetic field it can be rewritten as

$$H = \hbar v_F \begin{pmatrix} 0 & -i\frac{\partial}{\partial x} + \frac{\partial}{\partial y} - \frac{eBy}{\hbar} \\ -i\frac{\partial}{\partial x} - \frac{\partial}{\partial y} - \frac{eBy}{\hbar} & 0 \end{pmatrix}. \tag{1.53}$$

Here we followed the same logic as was used for the solution of eq.(1.46) [42] and chose Landau gauge $\vec{A} = (By, 0, 0)$. In similar manner we note that the Hamiltonian does not depend directly on x, therefore it commutates with $\hat{k}_x$ and the x-component of generalized momentum is therefore conserved. This allows to choose two-component electron wave-function for graphene as follows $(\phi_1(y), \phi_2(y))^T e^{ik_x x}$. With this wave-function the Schrödinger equation becomes now the system of equations for two components:

$$\begin{cases} -\dfrac{E}{\hbar v_F}\phi_1 + k_x\phi_2 + \dfrac{\partial \phi_2}{\partial y} - \dfrac{eB}{\hbar} y\phi_2 = 0, \\ -\dfrac{E}{\hbar v_F}\phi_2 + k_x\phi_1 - \dfrac{\partial \phi_1}{\partial y} - \dfrac{eB}{\hbar} y\phi_2 = 0. \end{cases} \tag{1.54}$$

Lets introduce new parameters: $\xi = l_B^{-2} y - k_x$ and $\lambda = -\dfrac{E}{\hbar v_F}$. This simplifies eq.(1.54)

to the form

$$\begin{cases} \lambda\phi_1 - \xi\phi_2 + \dfrac{1}{l_B^2}\dfrac{\partial\phi_2}{\partial\xi} = 0, \\ \lambda\phi_2 - \xi\phi_1 - \dfrac{1}{l_B^2}\dfrac{\partial\phi_1}{\partial\xi} = 0. \end{cases} \tag{1.55}$$

Substitution of ϕ_2 from the second equation of (1.55) into the first one gives

$$\lambda^2 l_B^2 \phi_1 - l_B^2 \xi^2 \phi_1 + \phi_1 + \frac{1}{l_B^2}\frac{\partial^2\phi_1}{\partial\xi^2} = 0. \tag{1.56}$$

With a new variable $\theta = \xi l_B$ the last equation can be rewritten as

$$\frac{\partial^2\phi_1}{\partial\theta^2} + \left(\left(\lambda^2 l_B^2 + 1\right) - \theta^2\right)\phi_1 = 0. \tag{1.57}$$

This is identical to the equation for the harmonic oscillator

$$\frac{\partial^2\psi}{\partial x^2} + \left(\frac{2\varepsilon}{\hbar\omega} - x^2\right)\psi = 0, \tag{1.58}$$

which has the solution (1.47). By comparing eqns. (1.47) and (1.58) we obtain

$$\lambda^2 l_B^2 + 1 = \frac{2\varepsilon}{\hbar\omega} = 2N + 1. \tag{1.59}$$

Substitution of the values that correspond to λ and l_B in (1.59) finally leads to the quantized energy levels [36, 38] in graphene

$$E = \pm v_F\sqrt{2\hbar eBN}, \quad N = 0, 1, 2, ... \tag{1.60}$$

Sign $+/-$ correspond to electrons/holes. The main difference between the LL's spectrum of graphene and other conventional 2DEGs is the absence of zero-energy state ($N = 0$) in the latter. The presence of $N = 0$ state in graphene leads to the observation of anomalous integer QHE. Indeed, if one assumes the standard quantization sequence for conductivity, i.e. $\sigma_{xy} = 4\nu e^2/h$, it would predict a plateau at $\nu = 0$ giving $\sigma_{xy} = 0$, when the Fermi level is at the charge neutrality point. However, this is impossible for graphene due to the existence of extended state at zero Landau level, when $N = 0$. At the Dirac point this state is shared by electrons and holes and there are $2(2\nu + 1)$ occupied states. The factor of 2 comes due to presence of two Dirac points in the first Brillouine zone. Therefore, the expected quantization sequence for

graphene is $\sigma_{xy} = 4(\nu + \frac{1}{2})\frac{e^2}{h}$, where the plateau at $\nu = 0$ is missing. This result was first measured experimentally by Novoselov *et.al.* [4]. The Hall conductivity and the density of states as functions of energy are represented on Fig.1.12. In comparison with the 2DEG case the distance between LLs is not constant and diminishes in graphene for higher carrier concentration. Since the energies of LLs are proportional to $\sqrt{N}$, those states close to the Dirac point are widely separated which allows the plateaus at $\nu = \pm 2$ to be observed even at room temperature [45] when the magnetic field is strong. The estimation of the cyclotron energy for 2D electron gas and monolayer graphene (scales as $\sqrt{B}$) at magnetic field approximately 10 Tesla gives us equivalent temperatures of about 10 and 1000 K respectively [36]. Also, comparing to this energy scale the Zeeman splitting energy is relatively small [37] ($\sim$ 5K), so the degeneracy factor of each LL is $g = 4$.

The unique manifestation of QHE in graphene is not determined mainly by massless nature of the charge carriers, but rather attributed to the presence of two sublattices in the unit cell. The low-energy Landau levels dispersion in bi- [19] and ABC multilayers can be approximately described by generalized formula [38] :

$$E_n = \pm\gamma_1^{1-N}\left(\frac{\sqrt{2}v\hbar}{l_B}\right)^N \sqrt{n(n-1)...(n-N+1)}, \quad n = 0, 1, 2, ... \tag{1.61}$$

with N being the number of layers. In bilayer graphene the separation between extended states is proportional to $\omega_c = eB/m^*$ ($m^* \approx 0.035m_e$ is an effective mass) and like in 2DEG systems it is constant (Fig.1.12(c)). Even though we deal here with massive particles, we still have zero LL which is now 8-fold degenerate (due to equal contribution of $n = 0$ and $n = 1$ in eq.1.61) and $\nu = 0$ plateau is also absent [46].

Similarly, for trilayer graphene we have 12-fold degeneracy of $n = 0$ LL (see eq.1.61), but the LL's spacing for higher energies become larger (Fig.1.12(d)). This degeneracy is preserved for both Bernal- and rhombohedral-stacked trilayers. In first case low-energy LLs can be well described by the combination of energy levels attributed to mono- and bilayer graphene [47]. For ABC trilayer, however, $E \sim B^{3/2}\sqrt{n(n-1)(n-2)}$ and 12-fold degeneracy at lower energies arises from the contribution of the trigonal warping, when the Fermi line above the points where conduction and valence bands are touching splits into three legged-pockets, as described previously. This degeneracy

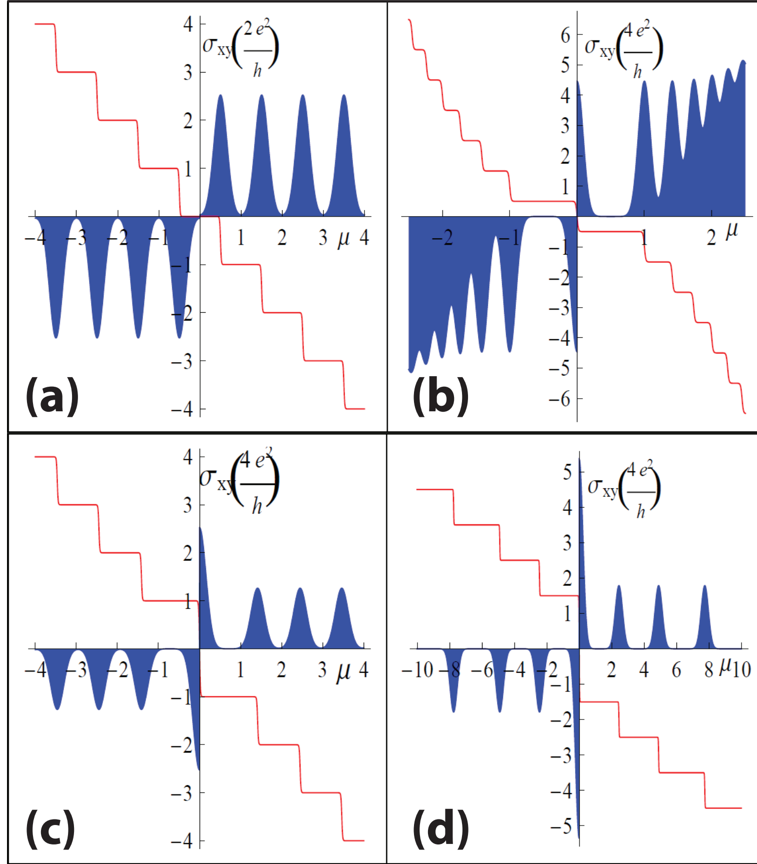

Figure 1.12: Schematic illustration of the quantum Hall effect in (a) conventional 2DEGs, (b) monolayer graphene, (c) bilayer graphene and (d) ABC stacked trilayer graphene as a function of chemical potential μ at fixed magnetic field. The red line on each figure represents transversal conductivity σ_{xy} and blue shaded regions correspond to the DOS (it is inverted for holes for clarity). The chemical potential μ is measured in units of $1/\gamma_1^{N-1}\left(\sqrt{2}\hbar v/l_B\right)^N$ with $N = 1, 2, 3$ for mono-,bi- and ABC trilayer graphene respectively and in units of $\hbar^2/(m^* l_B^2)$ for conventional 2DEG. Adapted from [38].

is broken when the energy surface undergoes the Lifshitz transition (see below).

1.6.5 Related experiments and theoretical expectations

Since the pioneering works on QHE in monolayer graphene [4, 37, 48], the multilayer samples recently started to attract more interest. It was necessary to understand the nature of broken symmetry states in those systems. The careful analysis was performed by group of P.Kim [46] on bilayer graphene. The authors completely lifted up the degeneracy in the zeros LL, showing the plateaus at $\nu = 0, \pm1, \pm2, \pm3$. The measurements of the activation energy gaps demonstrated that this level splitting was independent of spin and attributed to electron-electron interaction. The applied mag-

netic field, however, required for this experiment was extremely high - up to 35 T.

One of the first experiments on trilayer graphene, both ABA and ABC, also required very high magnetic field [33] (more than 20 T). The reason for this was the reduction of the sample's quality due to graphene being stacked in-between two oxide layers (for top and bottom gates). In this work new QH plateaus were resolved, in particular $\nu = 2, 4, 6, 8$ states in Bernal trilayer sample were clearly developed. Those states were referred to monolayer ($\nu = 2, 6$) and bilayer ($\nu = 4, 8$) parts, in the regions where Landau level's crossing is absent. In an ABC sample instead they observed expected quantization sequence, except the manifestation of $\nu = 12$ QH state. Nevertheless some plateaus were still missing.

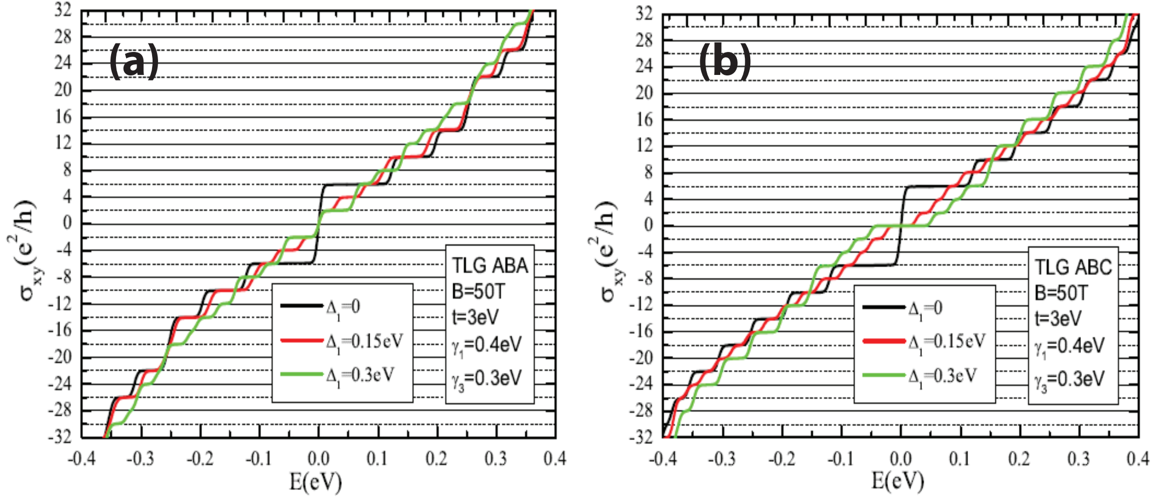

Figure 1.13: Hall conductivity of (a) ABA- and (b) ABC- stacked trilayer graphene calculated for different values of the interlayer asymmetry δ_1 induced by external perpendicular electric field. Adapted from [47].

Theoretical predictions for the quantization sequence at magnetic field for ABA and ABC trilayers is shown on Fig.1.13(a) and (b) respectively [47]. The QH plateaus are expected to appear at filling factors $\nu = \pm 6, \pm 10, \pm 14...$ in both types of stacking. As one may see, the plateaus at $\nu = \pm 18$ should not be present in Bernal trilayer graphene and is a distinctive feature of ABC-stacked graphene. Yet, it was observed once in experiment with high mobility ABA trilayer sample placed on top of hexagonal Boron Nitride [49]. This plateau was not well resolved even at $n = 5\ 10^{12}$ cm^{-2} and $B = 9$T and following to Ref [47] corresponds to the case of interlayer asymmetry δ_1 being 0.15 eV. However, this was not assumed by authors in Ref [49] in their model (δ_1 was set to 0) and thus there is a slight contradiction between theoretical expectations

and the experiment that leave open questions in this regard.

As was discussed previously, in rhombohedral-stacked trilayer graphene the trigonal warping produces strong impact on low-energy band structure. The appearance of Lifshitz transition and the warping effect can be probed by quantum Hall measurements. The LL energy spectrum for ABC trilayer was calculated in Ref [15]. The energy as a function of $\sqrt{B}$ is represented on Fig.1.14(b). When the magnetic field is small enough,

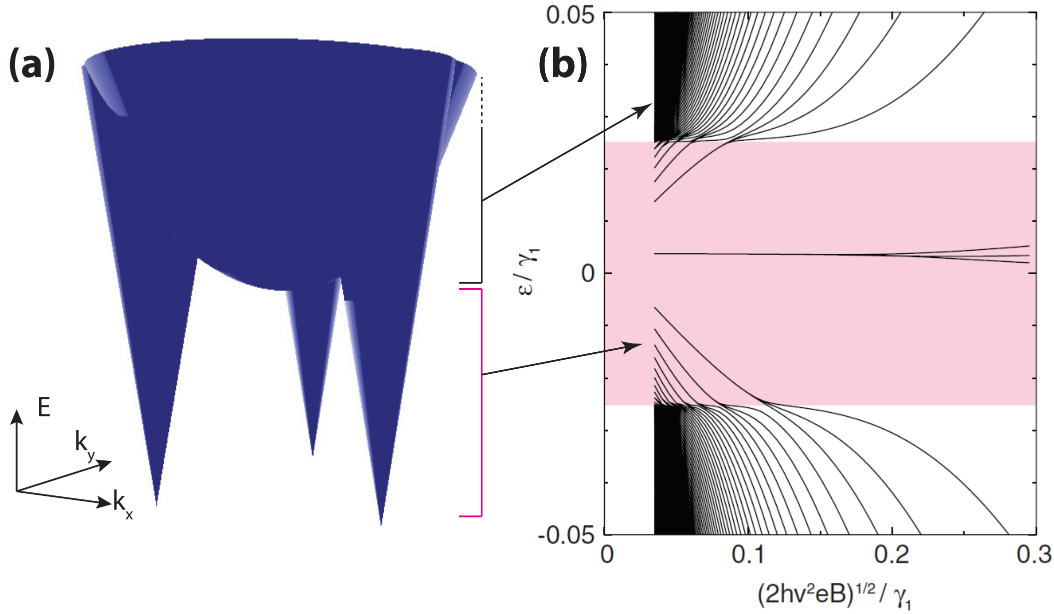

Figure 1.14: (a) Illustration of energy surface in ABC trilayer.(b) Adapted from [15]. Landau levels of ABC trilayer, plotted as a function of $\sqrt{B}$. Value of $(2\hbar v^2 eB)^{1/2}/\gamma_1 = 0.1$ corresponds to $B \sim 1$ T. The region where Landau levels are triply degenerate is shaded. The arrows show the corresponding areas in (a) below and above the Lifshitz transitions when degeneracy is broken.

each of the leg pocket accommodate an equal number of LLs, contributing, therefore, with a factor of 3 to the degeneracy. Below the Lifshitz transition point energy levels follow a similar sequence as in single layer graphene ($\sim \sqrt{B}$). This degeneracy can be broken at higher magnetic field or at energies $E_n \geq E_L \sim |\gamma_2|/2$ and each Landau level splits into three separate levels (see unshaded region in Fig.1.14(b)). The Landau level around zero energy, that is triply degenerate, corresponds to $n = 0$ level in each leg pocket. This degeneracy splits at slightly higher magnetic field.

The first experiment that demonstrated broken degeneracy states in the quantum Hall regime in ABC trilayer due to Lifshitz transition has been done by group of C.N. Lau [16]. The splitting of energy levels was clearly observed on the fan-diagram (differential conductance as a function of magnetic field and carrier concentration).

Nevertheless, the quantization sequence was rather odd - instead of predicted $\nu = \pm 6$, and $\pm, 10$ they claimed the appearance of $\nu = 9$. The authors attributed this fact to the influence of electron-electron interaction.

Chapter 2

Fabrication and characterization of samples. Experimental techniques

2.1 Introduction

The manufacture of graphene-based devices, including the characterization and determination of quality, thickness, stacking arrangement etc., is an essential step when performing experiments. In this chapter we describe the basic steps of the fabrication process, consider various methods of determination of the number of layers and approaches of analysing the quality of the samples. The principles of low-temperature transport measurements will be also discussed.

2.2 Graphene-based transistors

Over decades in the nanotechnology research field there were two different approaches in fabrication of nanoscale devices. They are so-called "top-down" and "bottom-up" ways, where depending on the aims, a sample could be made respectively either by separation of atomic planes from a bulk material or by grow on a substrate with successive arrangement of atoms on it.

Since 2004 up to now the common way in fabricating graphene samples is the "top-down" approach involving mechanical exfoliation of graphite pieces with a scotch-tape [1]. It starts from placing graphite chunk on one side of precut sticky tape. Then by stacking together and separating both sides of the tape several times (usually more

than 10) one can obtain the area with monolayer graphene on it. After that the part of the tape with high density of thin domains, that visually look more transparent, is pressed with a finger onto a Si/SiO_2 substrate. The latter should be clean enough to provide the good adhesion with respect to the sticky tape. Despite this method is not suitable for commercial production, the best quality devices are produced using the exfoliation technique. There are various substrates that are used as a sample base, like Si_3N_4, SiC or SiO_2. In a field-effect-transistor (FET) the substrates consist of two layers : conductive material (metal or doped semiconductor) and dielectric. In this case the bottom part of a substrate can be used as a gate that changes the types of charge carriers and controls the carrier concentration. The most commonly used substrate is p-doped Si with thermally grown oxide layer on top. All the experiments described in this thesis were performed on Si/SiO_2 substrates with the oxide thickness approximately 300 nm.

The fabrication steps are shown on Fig. 2.1. After depositing the flakes on a substrate one needs to find the one with required size and determine the number of layers. Although the exfoliation method does not allow to control the shape and the thickness of individual flakes it is possible to obtain graphene samples of relatively big size (up to 10^3 μm^2). The next step is to spin-coat consequently two layers of polymethylmethacrylate (PMMA)- positive electron beam resists - with different concentrations of anisole in it. These two layers are called soft (1st layer) and hard (2nd layer) PMMA with approximate thicknesses 300 nm and 100 nm respectively (these polymers are described in Appendix-I). Two different layers are necessary to give good lift-off profile for the contacts (will be discussed later). The deposition of resists is followed by soft baking to evaporate the solvent.

The next step in the fabrication process is e-beam lithography. The areas of PMMA resist exposed to electrons can be removed in a developer mixture of isopropanol (IPA), methyl isobutyl ketone (MIBK) and ethyl methyl ketone (EMK) with the proportion respectively 15:5:1. Then two metals of Cr ($\sim$ 10 nm) and Au ($\sim$ 80 - 100 nm) are thermally evaporated on top of the substrate under high vacuum. The auxiliary layer of chromium metal aims to improve the bond between conductive gold and the substrate. After, the whole sample is soaked in acetone. This procedure called "lift-off", when acetone dissolves all the PMMA layers under metal leaving only contact areas that have been deposited onto graphene and bare SiO_2. The importance of usage of

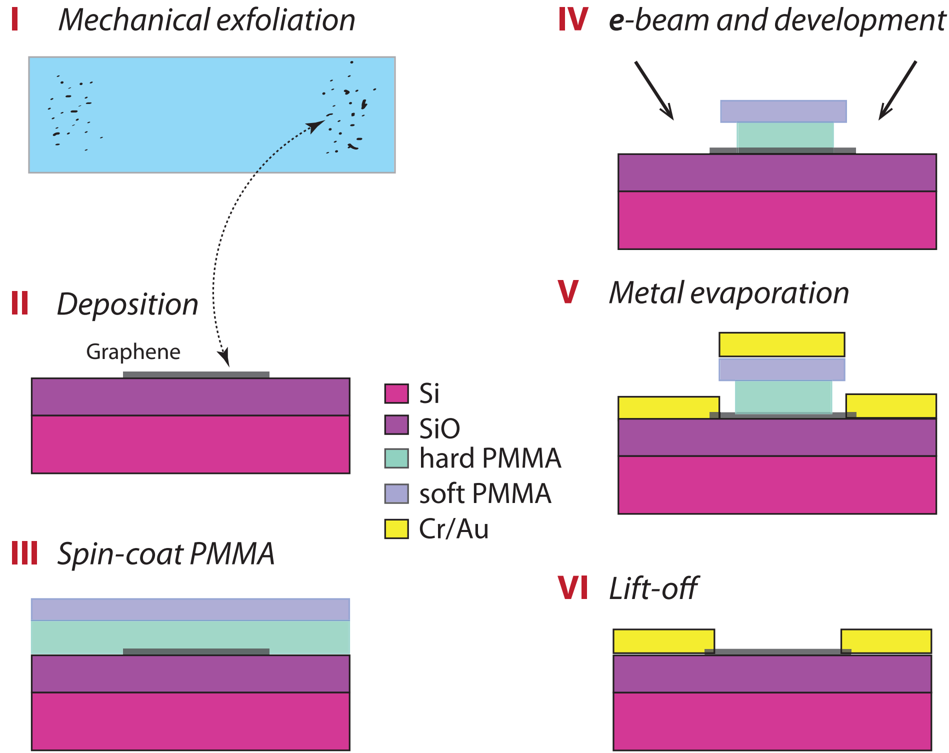

Figure 2.1: Schematic image of the fabrication process of a standard device.

two resists is that under the same dose of exposure, soft PMMA is more soluble in the developer than hard PMMA which is on top. This leads to an undercut profile (Fig. 2.1) which prevents an overlap between evaporated metal films on the substrate and on adjacent PMMA layers, thus making "lift-off" process easier. Finally we need to mount the sample inside standard chip and proceed with ultrasonic wire bonding to connect the contact pads on the substrate and the chip, which can be fixed inside the probe and put into cryogenic station for low-temperature measurements.

The fabricated device can be used as a field effect transistor. The schematics of the sample is illustrated on Fig. 2.2(c). The system − p-doped Si/SiO_2/graphene acts as a plane capacitor. So, by changing the potential difference between Si and graphene via applied back-gate voltage with respect to drain contact, which is grounded, one can control the charge on graphene. The measurements are usually performed in a constant current regime, when the ballast resistor $R_B \gg R_{Gr}$ and R_{Gr} is the resistance of graphene (R_B is typically 1 $M\Omega$ and R_{Gr} usually an order of kOhms). The current flowing from source to drain contact passes the ballast resistor which reduces its amplitude down to $\sim 10^{-7}$A, thus current maintains almost the same across the sample. A

voltage drop along the flake is measured by lock-in amplifier and 4-terminal geometry aims to exclude contact resistance (at the interface between graphene and chromium layer) in the measurements. In an ideal case of neutral single layer graphene, for example, the Fermi level is positioned at the Dirac point, where there are no states. At this stage the measured resistance is maximal, because no electrons are excited in the conduction band. When we apply positive voltage to the gate the negative charge starts to accumulate on the flake lifting the Fermi level up in the conduction band. By increasing V_g further the density of states increases and more electrons in the conduction band are involved in transport, thus the resistance drops down. It starts to saturate due to presence of short-range scattering [50]. A similar situation happens when we apply negative V_g, but in this case Fermi level lover down to the valence band and the transport is determined by holes. Typical $R(V_g)$ dependence is shown on Fig.2.2(a) Knowing the geometry of a sample and using experimental $R(V_g)$ dependence, one can

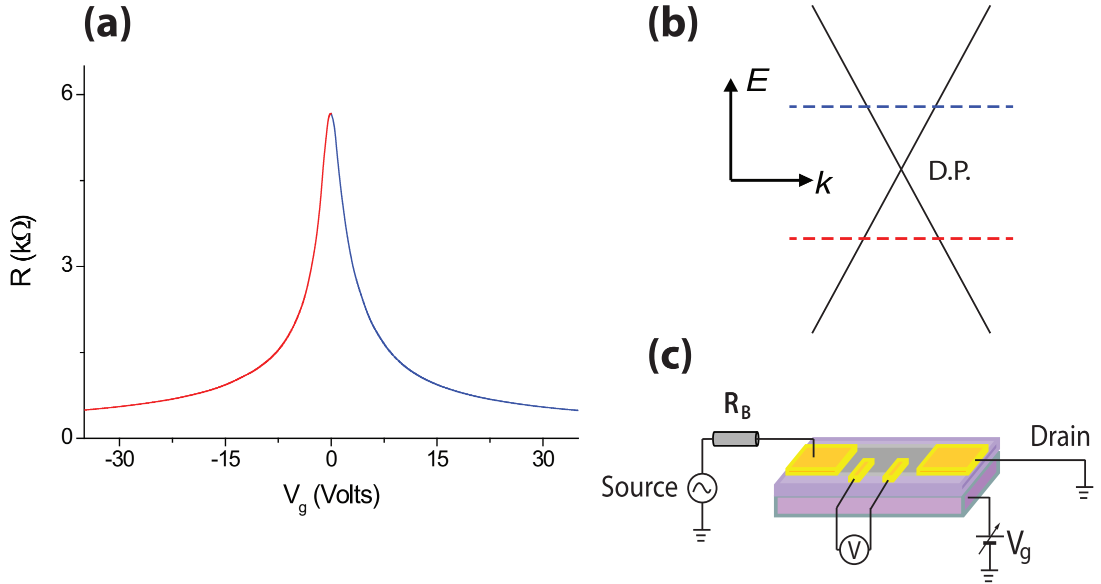

Figure 2.2: (a) Typical $R(V_g)$ dependence. Blue(red) part of the curve corresponds to electron(hole) current. (b) Energy spectrum around Dirac point (D.P.- on the graph). Blue and red dashed lines represent the position of the Fermi level at positive and negative gate voltages respectively (regions on the dependence in (a)). Schematics of the experimental setup.

estimate the carrier concentration and the mobility. Within the Drude's model the carrier mobility is $\mu = \sigma/ne$ (e is electron's charge). The carrier concentration can be written as $n = Q/(eS)$, where Q is the total charge and $S = LW$ is sample area between potential contacts. By employing the plane capacitor model with $Q = C\delta V_g$

and $C = \epsilon\epsilon_0 S/d$, we have the expression for the mobility:

$$\mu = \frac{N_{sq}}{RC^*\delta V_g}. \tag{2.1}$$

Here C^* is the capacitance per unit area; $N_{sq} = L/W$ is the number of squares of the sample; $\delta V_g = V_g - V_0$ (V_0 - gate voltage at maximum resistance); ϵ_0, ϵ and d are respectively electric constant, permittivity and the thickness of SiO_2.

2.3 Thickness and quality determination

All the methods of determining the number of layers discussed below have a degree of inaccuracy which increases with the number of layers. The advantages and disadvantages of various methods will be discussed in this section and examples will be presented.

2.3.1 Optical contrast

Surprisingly, being only one atom thick, single layer graphene can be visualized with an optical microscope [51]. It turned out that monolayer absorbs exactly $\pi\alpha$ (α is the fine structure constant), which is approximately 2.3%, of an incident light [52] and this does not depend on the wavelength. When positioned on the substrate, SiO_2 creates a cavity in a similar way as in Fabry-Perot resonator and the light is reflected multiple times between graphene and Si. Thus, thin flakes can give sufficient contribution to the interference picture. As a result the flakes are contrasted with respect to a bare substrate. An optical contrast defined as $C = (I_{sub} - I_{gr})/I_{sub}$, where I_{sub} and I_{gr} are intensities of the light reflected from the substrate and graphene respectively, depends strongly on a thickness of SiO_2 and a wavelength [51]. Fig. 2.3(b) demonstrates how one can enhance significantly the contrast for certain oxide thickness by cutting a narrow optical band with the aid of suitable filter. Green filter was found to be the best candidate for providing good contrast on a 300 nm SiO_2. For monolayer graphene the value of C is roughly 8-10 % if using green light and approximately 5 % for white light. These values do not change essentially when PMMA layers are spun on top. The optical contrast depends linearly on the number of layers : $C_N \approx NC_{monolayer}$. However, this approximation works well for $N \leq 3$ and then start to diverge from the

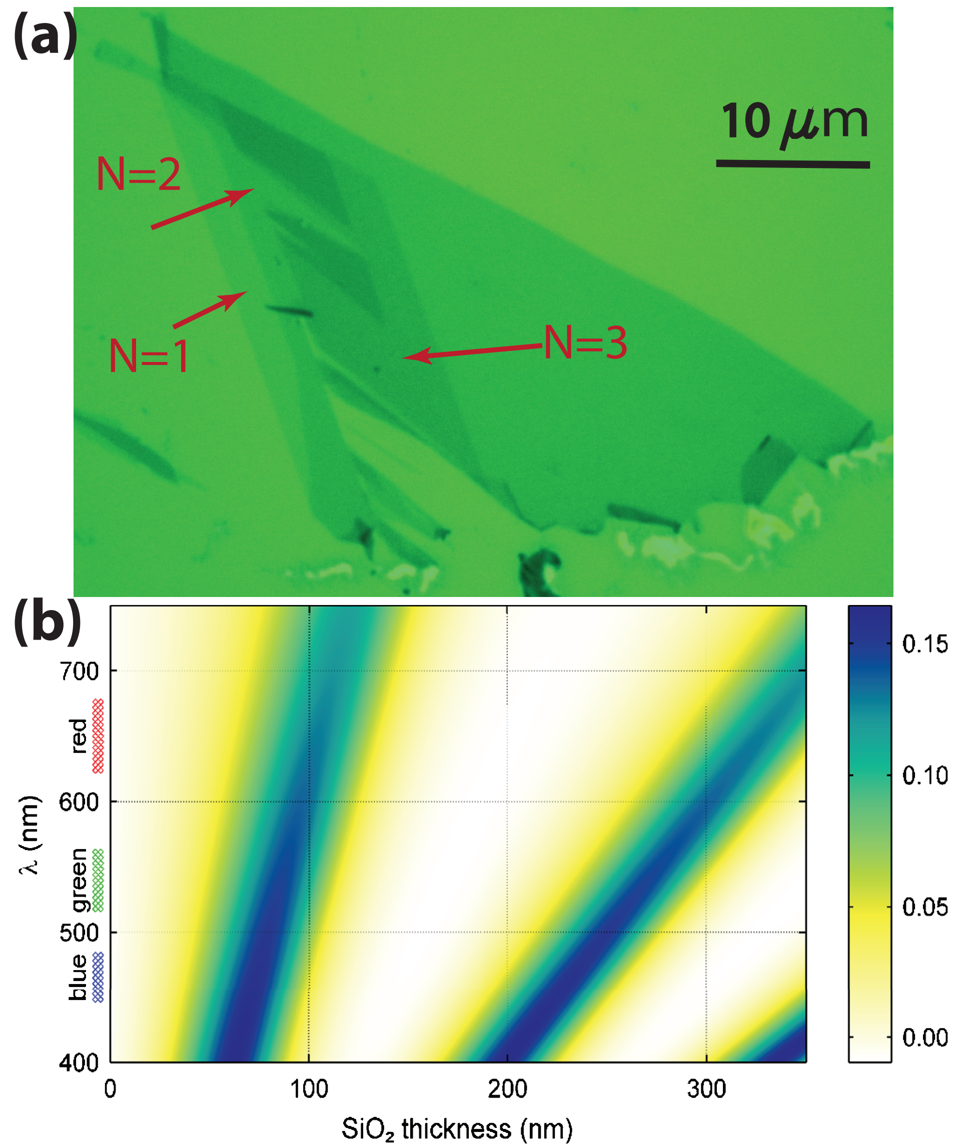

Figure 2.3: (a) An optical image of graphene flakes on top of Si/SiO_2 substrate. The number of layer are indicated by red arrows. (b) Color plot of the contrast as a function of wavelength and thickness of oxide layer (adapted from [51]).

linear dependence for thicker flakes.

To sum up, this technique enables finding the location of thin flakes relatively quickly on large substrates and provides an approximate value for layer numbers. Therefore, it is a good tool for selecting candidates for next fabrication steps. In order to distinguish graphene flakes more accurately one need to employ Raman spectroscopy analysis.

2.3.2 Raman spectroscopy

Raman spectroscopy is a quick, powerful and non-destructive method for characterization of graphene samples and allow to determine the number of layers [53], a relative amount of strain induced [54] and also levels of disorder and doping [55]. Discovered in 1928, this technique is based on inelastic photon scattering process, when an outcoming photon has changed in energy and hence shifted in frequency. When reflected light that consists of elastic (Rayleigh scattering) and inelastic (Raman) components is passing through the filter, the rest of the signal is collected by a detector and the data are represented as intensity peaks for a certain shift in frequency (Raman shift in cm^{-1}). Raman spectroscopy provides with the information about phonon spectra and chemical composition and is used for a wide range of material like gases, liquids and solids.

In graphene there are two main types of scattering mechanisms that participate in the Raman process. They are intra-valley and inter-valley scattering within the first Brillouin zone. Typical Raman spectra for graphene and bulk graphite are shown on Fig. 2.5(a). There are three most prominent features : G-peak at $\sim 1580\ cm^{-1}$, D-peak at $\sim 1350\ cm^{-1}$ (not shown on a graph) and a band (in case of single layer - a peak) at $\sim 2700\ cm^{-1}$ called the 2D band (or G′). The G-peak result from an in-plane vibration of the carbon atoms and is a first order scattering process. When an electron excited by a photon into the conduction band (Fig. 2.4(a)) it scatters a phonon with low momentum, close to the Γ point, and then recombines with the hole, re-emitting a lower energy photon. Alternatively, this scattering process with a phonon of very low momentum is ascribed to the relaxation of an electron to a virtual state before the recombination.

In contrast to G-peak, the D- and 2D- peaks originate from a double-resonance Raman process and involve inter-valley scattering of high energy phonons. In defect-free samples the D-peak in the spectrum is absent. It corresponds to a second-order scattering process with the phonon at the K point in the BZ. An excited electron is scattered into another valley (Fig. 2.4(b)) and can be returned to the original valley for further recombination via interaction with the short-range scatterers that requires large momentum shift. The zone-boundary phonons participating in this process do not satisfy the Raman fundamental selection rule and are not seen in the first order spectra

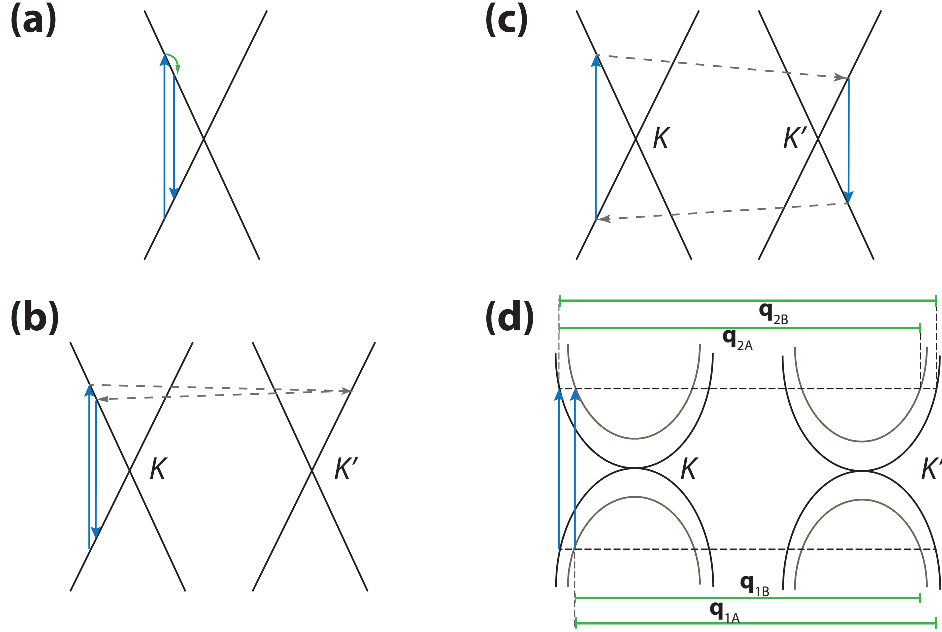

Figure 2.4: The schematic of the electronic transition process for monolayer in: (a) G-peak, (b) D-peak, (c) 2D-peak. (d) The same as (c) but for bilayer graphene. $\vec{q}_{ij}$ (i=1,2; j=A,B) correspond to phonon vectors that take part in scattering process.

in a perfect sample. However, it is observable at the sample edge. In our experiments a small D-peak was usually seen for the narrow samples with $W \leq 400nm$.

As for the G-peak, the 2D mode is always present in Raman spectra of graphene-based materials. Since it is fully resonant process, for single layer this mode requires two phonons of equal energy and opposite momentum (inter-valley scattering, Fig. 2.4(c)). As an example, in bilayer graphene (Fig. 2.4(d)) there are four resonant transitions [53] (indicated as a phonon vectors $\vec{q}_{1A}, \vec{q}_{1B}, \vec{q}_{2A}, \vec{q}_{2B}$ on the figure) due to difference in the band structure. In this case 2D peak is actually a band that consist of four peaks of different intensities. Since it is second order of the D mode its Raman shift is twice the shift of the D-peak position.

Analysis and comparison of these Raman modes makes it possible to distinguish between the layer numbers. The most distinctive cases are monolayer and bilayer samples. In graphene the 2D peak is a single symmetric peak which is much larger in intensity as the G-peak. This makes single layer graphene well distinctive among other samples with larger N. The intensities of the G-peak and 2D band are comparable,though, for bilayer. The shape of the 2D band is quite unique in bilayer (see Fig. 2.5(b)). When $N \geq 3$ the G-peak becomes large compared to the 2D-peak. The important number in the layer determination analysis is the full width at half maximum (FWHM). For

monolayer graphene it is $\sim$ 25-32 cm^{-1}, for bilayer it ranges from $\sim$ 52 to 59 cm^{-1}, in case of trilayer - $w \sim$ 58-67 cm^{-1} etc. However, for thicker flakes the determination becomes more complex and another approach is needed. Usually it relies on comparison of the ratio I_G/I_{Si}, where I_G and I_{Si} are intensities of the G-peak and Si-peak (at $\sim$ 520 cm^{-1}) respectively [33]. This number increases monotonically and discretely with N.

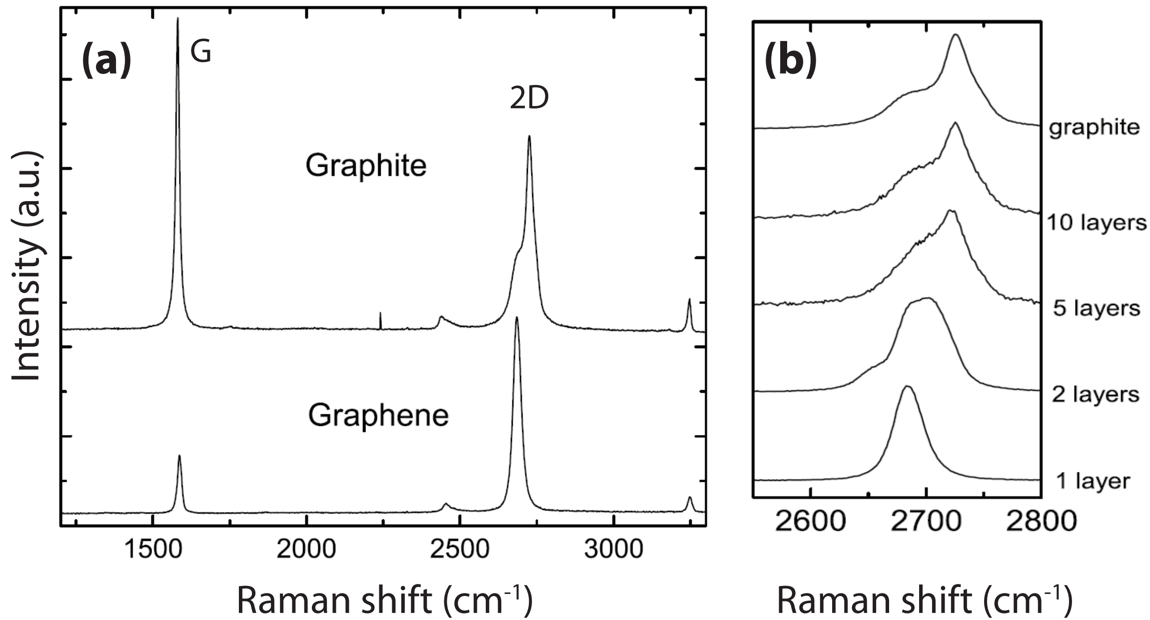

Figure 2.5: (a) Comparison of Raman spectra (λ = 514 nm) for bulk graphite and single layer graphene. The plots are scaled to have similar height of the 2D peaks. (b) Evolution of the 2D band with increasing number of layers. Adapted from [53].

The change in the Raman modes of graphene flakes under various circumstances, such as doping or defects, makes this tool very useful for the sample characterization. By analysing the ratio of the intensity of the D peak to that of the G peak one can estimate the density of defects [56] in disordered sample. Following the position of the G mode the doping level can be identified. Indeed, the shift of the G-peak increases and its FWHM decreases for electron or hole doping. It was also shown that the split of the G-peak characterizes certain amount of strain applied to graphene flake [54].

Finally, most important for our experiments is that Raman spectroscopy makes it possible to distinguish between two different stacking arrangements in trilayer graphene. Pioneering works on Raman analysis for ABA and ABC trilayers [32, 33] demonstrated distinctive features in 2D peak. Typical 2D peaks of Bernal and ABC trilayer are shown on Fig. 2.6. Six Lorenzian functions has been demonstrated to be a

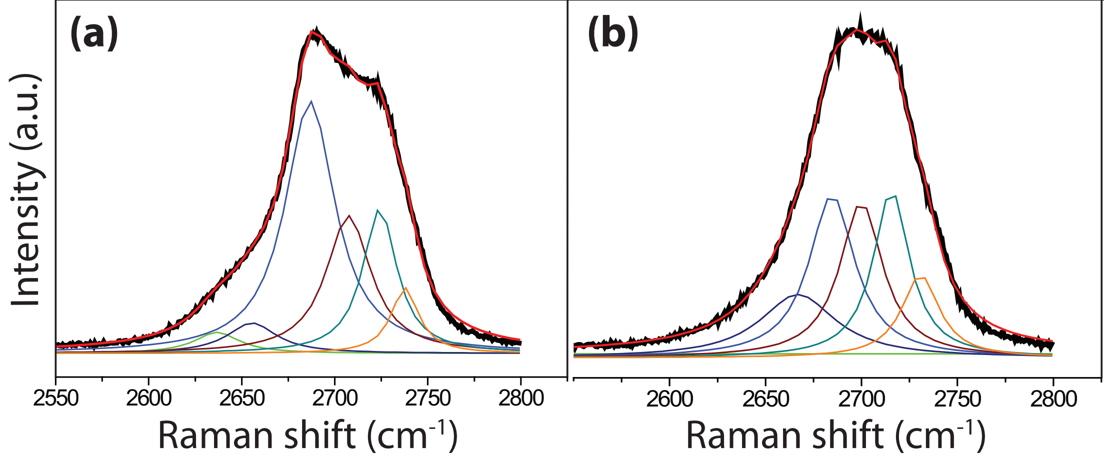

Figure 2.6: 2D Raman peak (black) fitted with 6 Lorenzian functions (red) for : (a) ABC and (b) ABA trilayers.

minimum number of curves required for an accurate fitting of the 2D band [33]. The FWHM of all the Lorenztians were set to be the same as that corresponding to the 2D peak for monolayer graphene ($\sim$28 cm^{-1}). The number of Lorentzian functions depends on the presence of three conduction and three valence bands around K point in both ABA and ABC trilayers. As was mentioned before, 2D Raman band is determined by double-resonance process involving inter-valley scattering. Therefore, many transitions between electronic states of different energy bands between two valleys contribute to the formation of this 2D mode. Some of them are excluded [32] in analysis due to close separation in energy leaving 6 resonant peaks. Analysing two graphs on Fig. 2.6 we notice clear asymmetry in the 2D peak of rhombohedral trilayer compared to those in Bernal trilayer. This distinction can be observed in the height difference of two auxiliary central Lorenzian peaks (blue and olive) - in case of ABA stacking they are similar in size. Nevertheless, the 2D band of both trilayers has almost the same FWHM $\sim$ 63 cm^{-1}. It was found [32] that a well developed asymmetric feature in ABC trilayer become more pronounced as the wavelength of the incident light increases, i.e. when the excitation photon energy diminishes. This fact apparently reflects that the differences in electronic structure at low energies is more conspicuous for different stacking orders.

Hence, as a conclusion, this method is a powerful non-aggressive tool for a quick characterization of the properties of graphene samples. Although, due to strong modifi-

cation of the spectrum and the background, when the flakes are covered with additional layers (PMMA, thin metal film etc.), this analysis becomes difficult and unreliable.

The measurements for this work on the Raman spectroscopy setup were performed using the laser beam with $\lambda = 532$ nm. The spot size of the beam was approximately 1 μm with the power of $\sim$ 5 mW.

2.3.3 Atomic force microscopy

Atomic force microscopy (AFM) is high resolution method of examination of surface topology. Within $\sim$ 5-7% accuracy AFM can resolve features of an order of several angstroms. This method allows to investigate both conductive and insulating samples. The basic parts of the experimental set-up are illustrated on the Fig. 2.7. The sharp tip (in most of cases the material is Si), with the radius $\sim$ 20 nm and main angle $\sim 22^o$, is connected to the cantilever. When approaching the specimen's surface the tip experience atomic forces (repulsion or attraction depending on the regime) that is reflected in the deformation of the cantilever. The bend of the latter is detected using the laser beam that is reflected from the cantilever's surface and recorded in photodetector. The sample is mounted on the stage connected to the piezoelectric scanner. The feedback module, knowing the deflection of the laser beam on the photodetector, controls the distance between the sample and the tip. The outcoming signal is analyzed py PC and data are represented as 2D intensity plot.

There are two main regimes of the AFM: the contact mode and tapping mode, also know as static and dynamic modes, respectively. In the former, the force between the tip and the surface is kept constant during scanning where the tip is pressed onto the sample. The deflection of the cantilever follows the surface corrugation. In the tapping mode the stiff cantilever oscillates around its resonant frequency. In this regime attractive forces are involved and the tip does not touch the sample. When approaching the surface the interaction causes the change in amplitude (or resonant frequency) of the vibrations which is reflected in a feedback signal. Simultaneously with the scan in tapping regime the phase shift of the oscillating cantilever relative to the driving signal can be measured. Changes in the phase can be used to discern between different types of materials on the surface, even though they are on the same height level.

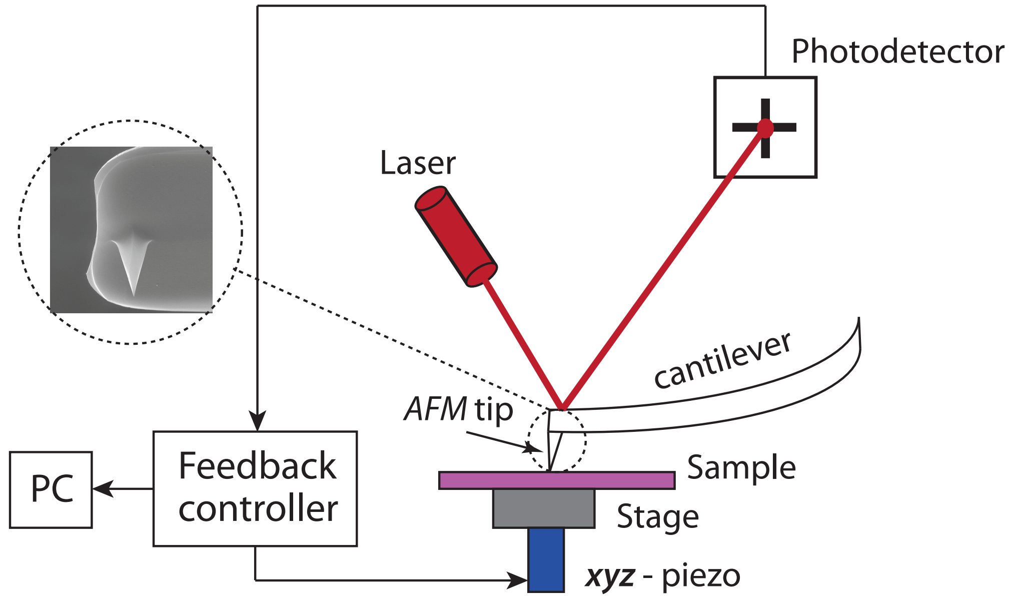

Figure 2.7: Schematic of the atomic force microscope (AFM). The inset shows scanning electron microscopy image of the tip.

The dynamic mode is an accurate, non-invasive way of investigation of the surface profile and was used for the sample characterization in our experiments. The distance between two adjacent layers in a graphene sample is known to be ~ 0.35 nm. Therefore, one may expect the thickness of the monolayer to be the same. However, the mentioned value can be obtained only when measuring the step-height between the bottom and the top layer that are stacked on each other (the measurements along the blue line on Fig. 2.8). If we measure the transition between typical oxide layer and the graphene, the height is approximately $1 - 1.4$ nm (varies from sample to sample) that is larger than expected. There are several facts that attribute this inconsistency. First of all, graphene's atomic lattice does not match the irregular amorphous structure of SiO_2, compared to layer-to-layer stacking case. Also, an additional contribution may arise from the water layer between a flake and the substrate due to hydrophilic nature of graphene on SiO_2. Finally, one can expect the incompatibility of the step-height profile related to the difference in the work functions of the oxide and graphene layer. Thus, the tip interacts differently with the substrate than with a sample. Nevertheless, the technique turned out to be very accurate for the flake determination when the height is measured with respect to bottom graphene layer. Our experimental value is ~ 0.36-0.4 nm per layer. The proper approach to determine the thickness of the flake with respect to substrate, though, relies on measurements statistics and requires at least

one naturally folded flake on the substrate.

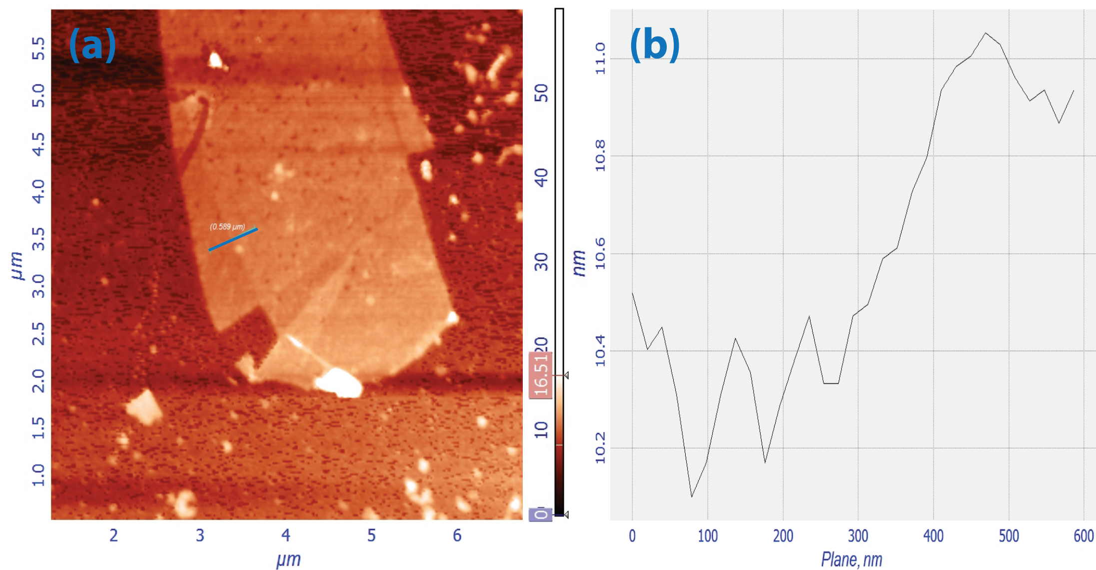

Figure 2.8: (a) Topography of graphene flakes on top of Si/SiO_2 substrate(AFM image); (b) a profile taken along a blue line in (a).

The dirt or residuals from chemicals on the sample can be detected from AFM scan (shiny dots on the flake, Fig. 2.8(a)). It gives us rough estimation of contamination level. For example, one may compare two scans before and after thermal annealing and see the change in the density of the dopants for further calibration of annealing parameters (temperature,time etc.). Remarkably, AFM can be used to clean graphene samples from the contaminations [57] by mechanical removal of doping molecules using contact mode.

2.3.4 Conclusions

As one might see, each method discussed above has some imperfections and restrictions. For example, to perform both Raman spectroscopy and atomic force microscopy it is necessary to predefine the positions of graphene flakes. The best way to determine reliably the number of layers is to combine at least two methods. Experience showed that characteristic values identifying the layers number obtained in measurements may occasionally "overlap" for different samples which brings a confusion in analysis. For example in the optical method the contrast, say 10%, can be the same for monolayer and bilayer graphene. For thicker flakes this occur more often. The possible reason is that the surface of SiO_2, which is grown thermally, is not perfect and atomically flat, that

might lead to a small variation of optical contrast [51]. Similar situation happens when measuring FWHM in Raman spectroscopy. Sometimes, the value 59 cm^{-1} of FWHM corresponds to bilayer and ABA trilayer that are located on the same substrate and on the big-range scan the shape of the 2D-peak for both flakes looks almost identical. Thus, detailed analysis is required. One can perform the following procedure for thin flakes with different contrast that were deposited on one substrate. We subtract the background Raman signal, then normalize the intensity of the 2D-peak and replace the origin with the right part of the curve where FWHM is measured. An example is shown on Fig. 2.9. We notice the split into several groups that have similar range of FWHM. Together with optical contrast measurements this allows to separate accurately the samples with different layer number and minimize the uncertainty conditioned by the data "overlap" mentioned above.

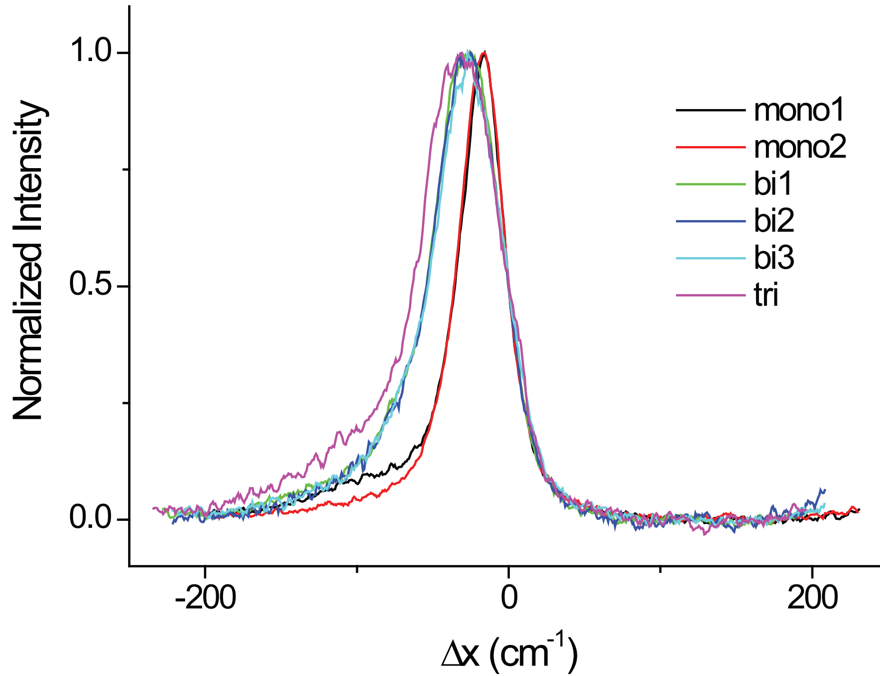

Figure 2.9: Normalized intensity of 2D Raman peaks for different mono-, bi- and tri-layers as the function of frequency Δx (cm^{-1}). The position of the right part of each curve where normalized intensity equals 0.5 was set as the origin for clarity.

Since the investigation of trilayer graphene samples was the major part of our experiments and the identification of such flakes is not straight forward but rather challenging, the statistics was therefore necessary. We performed complex analysis

involving optical contrast measurements and Raman spectroscopy.

In the end, we should mention one more layer determination method by performing low temperatures transport measurements. It is Quantum Hall Effect. As was discussed in Chapter1, due to unique nature of graphene samples the sequence of Quantum Hall plateaus is well distinctive for mono-, bi- and tri- layers. Quantum Hall measurements can be used as an auxiliary step of confirmation the number of layers.

2.4 Low-temperature set-up

To investigate transport properties of graphene systems very low temperature is often required. Our low-temperature experiments were performed in the Helium-3 cryostat from "Oxford instruments". In this section we will discuss the principles of Heliox-TL (top loading) system.

With Heliox-TL system on can reach the temperature as low as 250 mK (base temperature),which maintains stable for about 100 hours, and apply magnetic field up to 12 Tesla. The main principle of cooling down to temperatures below 1 Kelvin is based on the pumping ^{3}He and ^{4}He gases. The schematics of the cryogenic system is illustrated on Fig. 2.10. The sample is mounted inside the probe which is lowered down to the sample space where the liquid ^{3}He is condensed. The cryostat consists of two main vacuum chambers : outer (OVC) and inner (IVC). The first one prevents the heat exchange between the atmosphere and liquid ^{4}He. The second aims to insulate low temperature working space from the main bath (with $T = 4.2$ K). The cooling process comes in two stages. The helium from the main bath is connected through the pipe to the 1K-pot via needle valve. The ^{4}He vapour is pumped from the 1K-pot by rotary pump. This reduce the temperature of liquid helium in the 1K-pot down to 1.2 K (this temperature depends on the flow of liquid that is controlled by the needle valve). When the sorption pump (sorb) is heated to 30 K it releases gaseous ^{3}He inside the IVC. The gas is then cooled down to 1.2 K by the 1K-pot and condensed in the sample space. At this first stage, hence, the temperature of the sample is 1.2 K. The second stage is the cooling down the ^{3}He liquid. When the sorb-heater is switched off and all gas is condensed in the samples space the sorb cools down to the 1K-pot temperature and start to absorb ^{3}He vapor above the liquid. This leads to the cooling of liquid in the sample space down to base temperature. In order to raise the temperature the ^{3}He-pot

and the sorb heaters are used. The temperature can be ranged from 0.25 to 200 K and stabilized via ITC, intelligent temperature controller (Oxford instruments). The magnetic field in the superconducting magnet, located at the bottom of the chamber, is supplied by the IPS-120 controller (Oxford instruments) and is ranged from 0 to 12 T (the polarity can be changed as well).

The advantage of the system is that the experiment can be carried out as long as needed without taking the samples out. The cryostat just need to be filled by transferring liquid ^{4}He through the main tube.

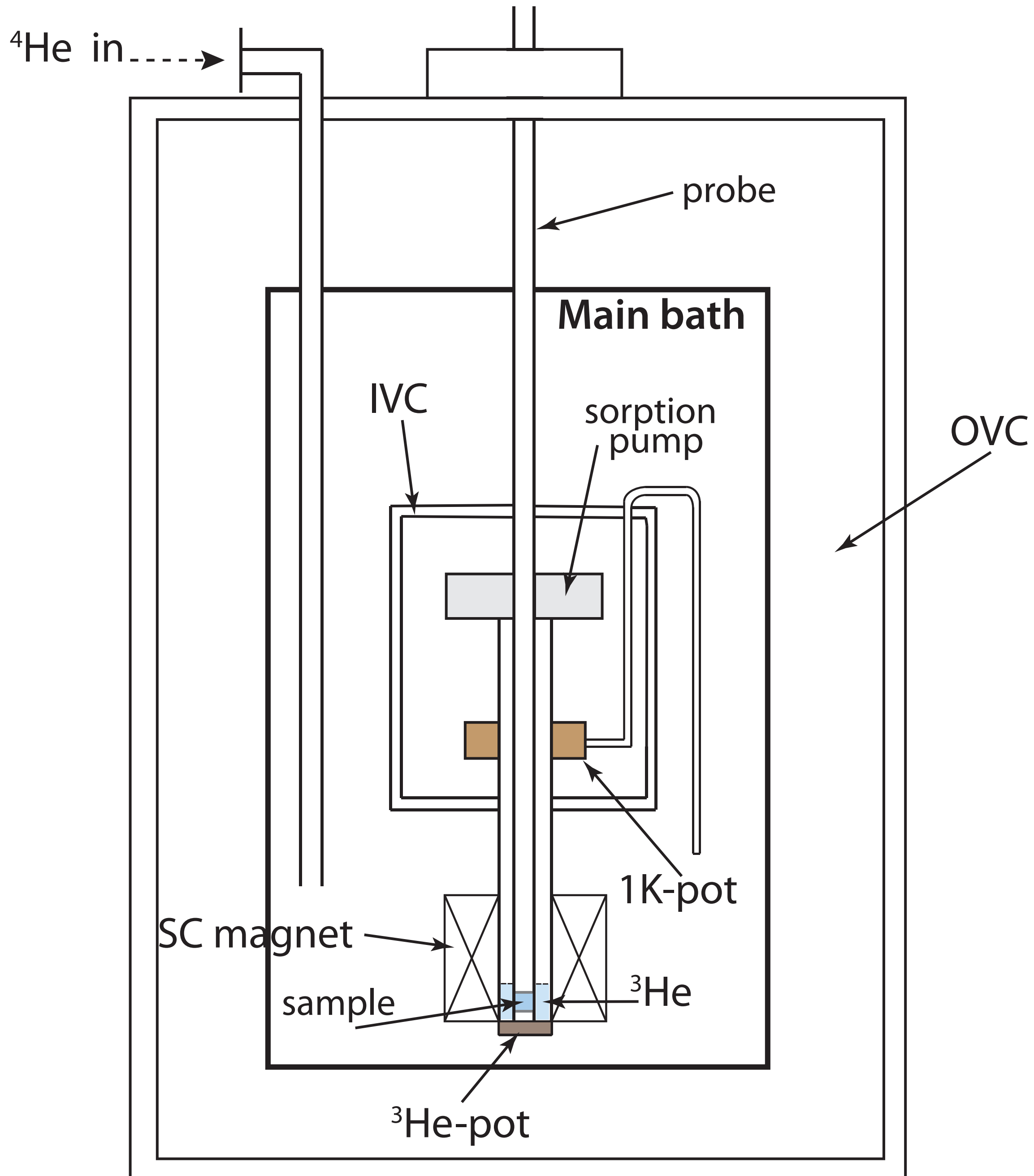

Figure 2.10: Scheme of "Oxford instruments" Heliox-TL cryostat.

Chapter 3

Fabrication of high quality double-gated devices

3.1 Introduction

Typical graphene devices, supported on SiO_2, are restricted in the performance of electrical transport properties due to the effect of a substrate. Indeed, the layer of SiO_2 introduces surface phonons and contains charge impurities and imperfections, as well as introducing a rough surface. These factors cause scattering during electrical transport. Also, water trapped between graphene and the oxide layer [58] introduces charge puddles that make carrier density distribution non-uniform along the sample. Aforementioned factors were predicted to restrict room temperature carrier mobility of the devices on SiO_2 substrate to a maximum value of $\sim$40 000 cm^2/Vs [59]. However, the fabrication of high quality suspended samples enabled reaching ultrahigh carrier mobility, ranging from $2{\cdot}10^5$ up to 10^6 cm^2/Vs [60–62]. This in turn, allowed the observation of fractional quantum Hall effect in graphene [63] (which was never observed on devices on SiO_2), the probing of low energy band structure in bilayer samples [64], the detection of flexural phonons' mode of graphene membranes [65] and the investigation of new broken-symmetry states at low magnetic field in a QH regime [16, 66, 67].

Furthermore, supported samples impede an accurate experimental study of intrinsic thermal, optical and mechanical properties of graphene, whereas the use of suspended sheets allows these properties to be carefully investigated. With the measurements of freestanding graphene membranes many surprising effects were discovered, such as

controlled rippling formation (changes in amplitude, wavelength and orientation) and unexpected negative thermal expansion coefficient [68, 69], high thermal conductivity [70], large Young's modulus [71], very high resonant frequency and room temperature quality factor [72, 73]. In this regard, suspended graphene samples are one of the best candidates to be a part of nanoelectromechanical systems (NEMS) and they hold a big promise.

High quality devices are necessary for probing intrinsic properties of graphene that are of interest both for fundamental physics and electronic applications.

This chapter is dedicated to a complete description of the fabrication process of high-quality suspended and dual-gated graphene samples. All the steps will be carefully described with particular emphasis on the improvement in the sample's quality after fabrication. The experimental results will be also demonstrated.

3.2 High quality samples: fabrication approaches

Since SiO_2 reduces graphene's mobility, many various materials were attempted as an alternative dielectric. Thus far, hexagonal boron nitride (BN) was found to be the best supporting layer. Many nowadays devices are fabricated on top of hexagonal BN and their mobilities revealed to be as high as 25 m^2/Vs [74]. The fabrication consists of several transferring steps followed by common e-beam lithography technique. Similarly to graphene, hexagonal BN can be mechanically cleaved to thin flakes with a scotch tape and deposited onto a substrate - it is used as an additional insulating layer between SiO_2 and graphene. The thickness of boron nitride can be identified with optical contrast or AFM methods. After placing graphene on top of h-BN, conventional fabrication procedure described in Chapter2 is usually applied to make contacts. Additionally, one more transfer step of h-BN flake can be performed for further employing of lithography and metal evaporation in order to obtain top-gated devices.

A second approach to improve transport characteristics of the samples is to remove an oxide layer underneath the flake, leaving free-hanging 2D sheet. So far suspended graphene samples demonstrated the largest carrier mobility, even higher than those on top of h-BN. Following this approach there are several suggested fabrication methods to produce suspended graphene devices.

Substrates of p-Si/SiO_2 can be prepared before the deposition stage, usually, by

means of either optical or e-beam lithography structure with trenches/holes of a certain width/diameter is drawn (like on Fig.3.1(a)). Then protective polymer layer serves as a mask for reactive ion etching (RIE) or wet etching in hydrofluoric (HF) acid (will be discussed later). After dissolving resist layer, exfoliated graphene flakes are rubbed onto a substrate. The flakes that lay between the SiO_2 pillars (or cover the hole) are identified first by optical microscope and after, verified with scanning electron microscope (SEM) or AFM. Once suspended flakes are found, the shadow mask, commonly made by ion beam on Si_3N_4 membranes (about several microns thick), is aligned and positioned on top of substrate. Metal contacts are then evaporated on top of pillars where the flake was found.

A slightly modified method to the one described above is based on the deposition of graphene at the very last step, so that the interplay between graphene and chemicals is minimal. In this case optical lithography is used to predefine the structure similar to interdigital transducer (Fig.3.1(a)). Then Cr/Au metal evaporation followed by lift-off process is done to obtain final structure. The advantage of this is that if we evaporate thick enough metal film, say $\geq$ 200 nm, there is no need to perform etching of the oxide layer. Optionally, one can make deeper trenches by submerging the substrate into HF solution - metal protects the regions with SiO_2 underneath. The last step is the deposition of graphene on top of metal pads. This technique was promising to give the cleanest samples - almost as pure as pristine graphene. Nevertheless, it turned out to be very challenging to fabricate real device. First of all, since graphene is placed on gold electrodes, the contrast is very poor (see Fig.3.1(b)) compared to the case of SiO_2 substrate (less than 6% for trilayer graphene). Another problem come from the fact that finding flakes which lay exactly between gold pillars is a statistical process. Besides, random deposition process can lead to accidental shortage between source and drain contacts by another graphene flake and the current may flow through it as well, which brings uncertainty in the measurements. In order to solve this problem the micromanipulator with a sharp metal tip was used to remove away unwanted flakes.

It is worth mentioning that a size and a shape of predefined trench or hole is important. We obtained flakes on top of SiO_2 substrates with etched holes (Fig.3.1(c)), but in the case of trenches nearly all the flakes were collapsed. Our experience showed that almost in 95% of the cases if the width of the trench exceed 1.5μm the flakes are collapsed (see Fig.3.1(b)). Thus far there was only one report about successful experiment

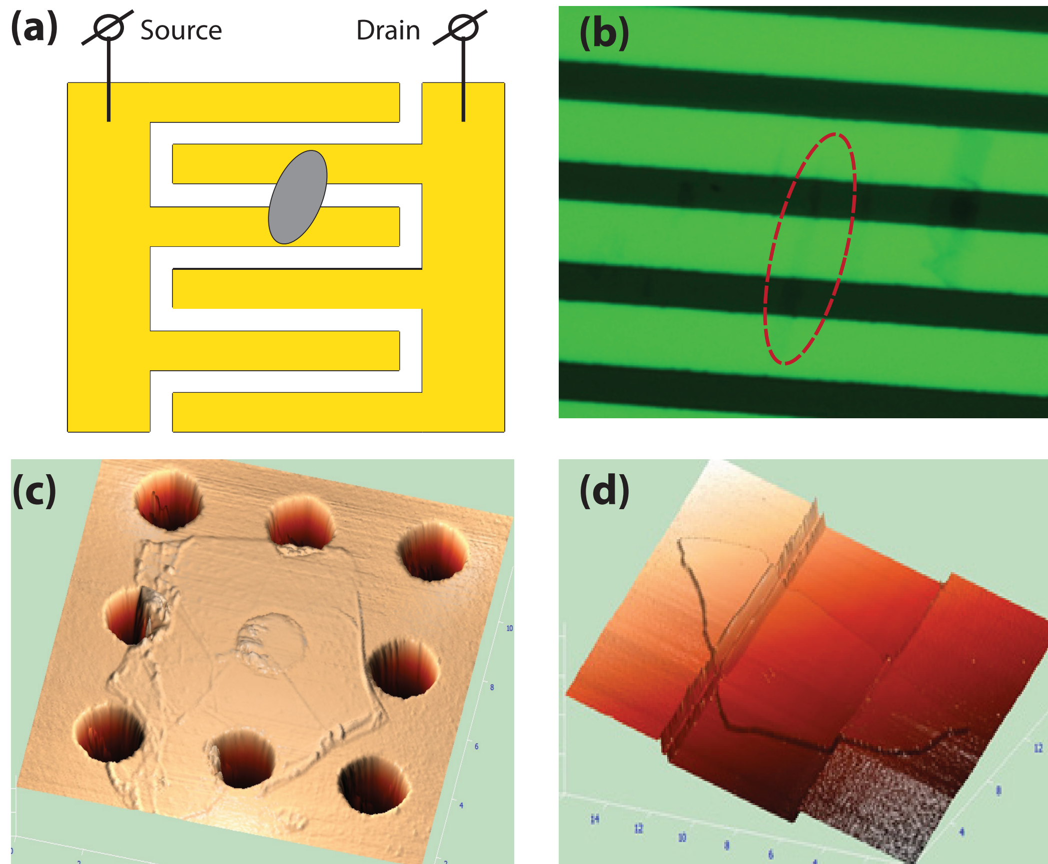

Figure 3.1: (a) Illustration of pre patterned structure with gold electrodes (see the description above). The distance between adjacent metal electrodes ranges from 1 to 3 μm, and the width of the pillars is 4-6 μm. Gray ellipse demonstrates graphene flake laying acros the trench. (b) Optical image of a real device shown in (a). Red dashed line surrounds the area with trilayer graphene flake. Poor contrast demonstrates that it is difficult to visualize suspended graphene on top of this structure. (c) and (d) AFM scan (3D image) of graphene flakes on top of etched holes and trenches, similar to illustrated in (a). The hole's diameter and trench's width are 1 and 2 μm respectively.

that was performed using very similar fabrication approach [75]. In our experiments out of ~100 devices we managed to find one where the flake was partially suspended between golden pillars - it sagged to 200 nm in the middle of the trench, which width and depth were respectively 1.3 μm and 300 nm. Hence, in spite of promising very good quality of samples, this technique was considered to be very challenging and ineffective at this stage and, probably, required further improvements in fabrication steps or change in the technology.

The results demonstrated by shadow mask technique are quite impressive. Since there were no chemicals affecting graphene during the fabrication process, the mobility of as-fabricated samples ranged from 5 to 20 m^2/Vs [76]. However, independent of

sample's quality this approach does not allow to fabricate suspended bridge on top. For this reason another solution was used to prepare clean suspended samples with air-bridge gates.

The fabrication procedure performed in our experiments is based on the process very similar to a widely used flake suspension with an aid of wet chemical etching followed by critical point drying, elaborated in 2008 [60, 61]. Standard substrates of p-Si with 300 nm oxide layer on top are carefully cleaned before graphene deposition (for detailed information see Appendix-I) in order to provide a good adhesion of the surface and, therefore, increase the density of the flakes on a specimen. Thin flakes are detected by means of optical contrast and then confirmed by Raman spectroscopy. For the majority of our devices it is not necessary to obtain large area flakes. It will be explained later that this method is suitable when their width is typically less than 2.5 μm (for top-gated samples) and the separation between the contacts usually do not exceed 1 μm. Below we describe step by step the manufacture of our suspended samples starting with the fabrication of an air-bridge electrode.

3.3 Suspended gate fabrication

The main idea of making an air-bridge, that is used as a top gate, is based on the use of a sacrificial layer. This layer and e-beam resists should be sensitive to different etchants and developers. In our experiments we tried two materials as a sacrificial layer: Al metal film and PMGI-SF6 resist (chemically modified LOR - lift-of resist).

Fabrication of bridges using Al is rather straight forward. We start from a step when Cr/Au contacts are patterned on graphene. We then spin subsequently two layers of PMMA (soft and hard) on the specimen and expose the area on the flake where the bridge part (which is hanging over) should be. After development of PMMA resists, Al metal is thermally evaporated under high vacuum. The advantage here is that we have a good control (up to 1 nm) on the evaporated thickness of the sacrificial film, that basically determines the distance between the gate and graphene (so does capacitive coupling constant). After lift-off process, the metal remains only on exposed area and the sample is coated by e-beam resists again for final lithography step. Here we expose and develop the whole regions that will be a gate electrode, including contact pad area and pillars part, aiming to support the bridge. Thick metal film is thermally

evaporated: depending on Al thickness deposited Cr and Au layers are ranging between 30-70 nm and 100-130 nm respectively. It is worth mentioning the relative ratio between the thicknesses of sacrificial layer and evaporated metal - about 3:4 ; thus metal should be at least 25% thicker, otherwise bridges are not mechanically stable. After lift-off process, Al layer can be removed by submerging the device into MF-319 photoresist developer. Metal bridges with a length up to 6 μm can be reproducibly fabricated in this way without the need for critical point drying (CPD).

The method, aimed to manufacture the bridges with Al film, has certain advantages. Due to flat surface of thermally evaporated Al metal the bottom of the bridge is uniformly even, which guarantees homogeneous charge distribution across the flake when applying a gate voltage to the electrode. As was mentioned, the thickness can be controlled very accurately and there is no need in further calibration of the height of the bridge. However, this material significantly dopes graphene, shifting the Fermi level far away from the neutrality point, and it is more difficult to remove it's residuals after the fabrication*.

An alternative sacrificial layer which can be used in this case is PMGI resist. We follow a procedure similar to that suggested in Ref. [77]. The fabrication steps are summarized on Fig.3.2. At first metal contacts are obtained by standard electron-beam lithography in positive PMMA bi-layer (soft and hard) followed by development, thermal evaporation (10nm/90nm of Cr/Au) and lift-off (see Fig.3.2). We subsequently cover our device with PMGI and PMMA1/PMMA2 layers. Compared to the method where Al metal is used, the thickness of this polymer sacrificial layer depends on the concentration of PMGI-SF6 with respect to "T-thinner" diluter, as well as on the spin time and speed. The calibration of the thickness, which was done with a surface profiler after spin-coating, can be found in Appendix-II. The areas denoted as "I" and "II" on the inset of Fig.3.2(b), which correspond to supporting pillars for the bridge, are exposed by the electron beam and developed first in PMMA-developer and then in MF-319 photo-developer. MF-319 does not act as a standard developer for PMGI, it etches this polymer uniformly in all directions, independent on whether the area has been exposed with electrons or not. Here, PMMA layers on top act as a mask to protect sacrificial layer from being etched away completely. Yet, the same amount that

*It was also noticed, that standard thermal evaporation of Al metal under high vacuum can degrade the quality of SiO_2 - in almost 50% cases the leakage current through the back-gate was detected during the transport measurements of these devices.

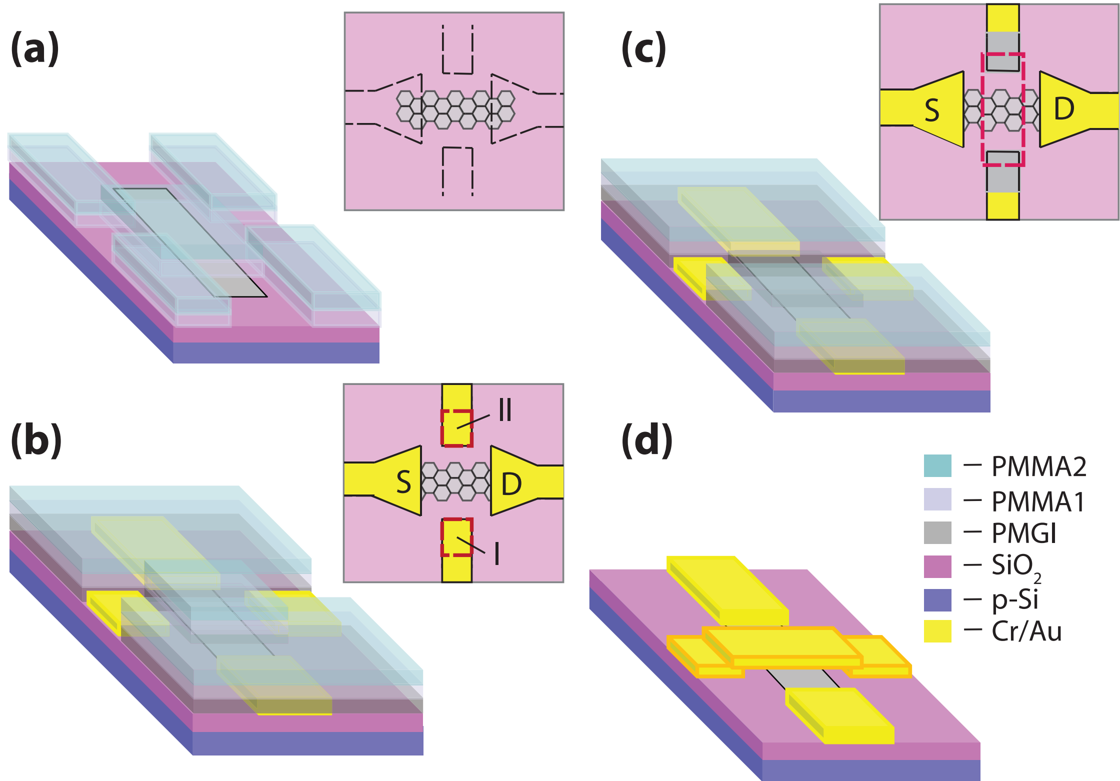

Figure 3.2: Fabrication process for air-bridge gate electrode. (a) Spin-coating the sample with two subsequent layers of soft and hard PMMA (1 and 2 respectively) followed be e-beam lithography. Inset: schematics of the top-view of patterned structure. (b) Metal evaporation and lift-off. Covering the sample with PMGI/PMMA1/PMMA2 polymers and electron beam lithography of the areas denotes as I and II on the inset. (c) Exposure of and development in PMMA developer only of the area marked by dashed rectangular on the inset. Shaded gray rectangles correspond to regions of developed polymers in step (b).(d) Evaporation of metal bridge and lift-off followed by removal of PMGI resist.

is etched down is etched along the sample plane and this factor (basically the thickness of span PMGI) should be taken into account during the e-beam patterning step. We diluted MF-319 developer with purified water in a proportion of 1:1 for better control of the development time. The calibration of the etching time is presented in Appendix-II. Straight after the development step electron beam lithography is performed on the region related to the bridge (dashed red rectangular on the inset of Fig.3.2(c)). Typical thickness of PMGI layer used in our experiments is 150 nm, accordingly we evaporate subsequently about 30 and 110 nm of chrome and gold respectively (added to about 100 nm of metal pillars evaporated on a first stage) and then submerge the substrate into acetone for lift-off. Finally, we remove the layer underneath the bridge in MF-319 and dilute it in purified water. Similarly to method discussed previously, we dry the

device with nitrogen gun.

The final shape of the bridge is rather arch-like, because the development in MF-319 smoothes edges of the region which protects graphene. Thus, the uncertainty in height along the bridge, that has been estimated, varies between 10 and 20 nm. The problem might be solved by making bridges slightly longer (plus extra 200 nm) - the distance between the flake and the bridge then remains almost the same. This technique turned out to be very reliable, produced less contaminated samples and was used for all our double gated structures in the experiments.

At last we want to mention that the manufacture of top electrodes allows to produce gate-defined quantum dots in bilayer and ABC trilayer graphene by introducing potential barrier on a short-scale area with aid of external perpendicular electric field (see Chapter1). We can draw a hole with the diameter of about 100-200 nm inside 250-300 nm wide bridge. The example is shown on Fig.3.3. Furthermore, when thick enough metal film is evaporated for the gate electrode, the bridges with length up to 2 μm revealed to be suspended even without having a support on another side. This gives the possibility to produce split suspended gates on top, similar to one produced by Yacoby's group [78], or with sharp tip-like edges, creating 1D ballistic channel.

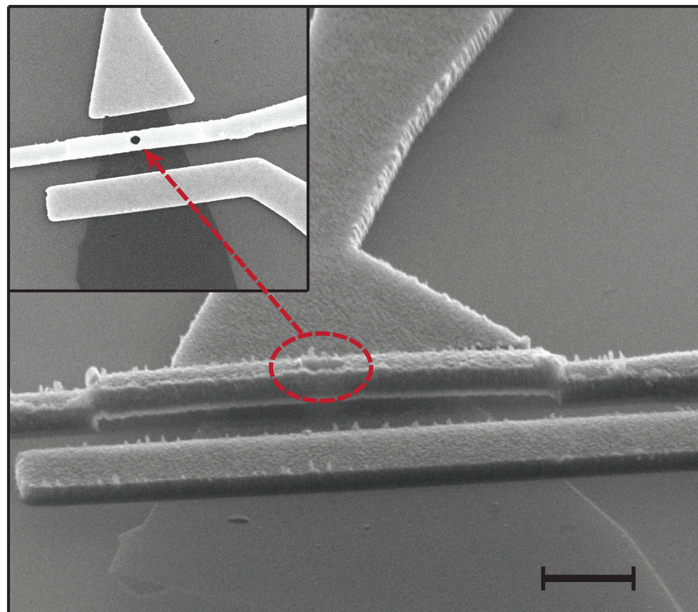

Figure 3.3: SEM micrograph of suspended metal bridge over the graphene flake. The region highlighted with dashed ellipse corresponds to the area with the hole, shown on the inset. Inset: top-view of the same device - the hole's diameter is about 150 nm and the width of the bridge is 350 nm. The scale bar corresponds to length of 1μm.

3.4 Etching of SiO2

Following the most common approach of producing suspended devices we remove the support underneath graphene with metallic contacts on it by etching SiO_2 layer with hydrofluoric acid (HF). In our experiments we tried two methods of etching oxide with HF : wet etching in liquid acid and with it's vapors. In the second case the sample is placed into an enclosed chamber where liquid acid is thermally evaporated from the bath. The process is controlled by adjusting three parameters: pressure, temperature and time. Being etched at gaseous conditions, graphene flake is not affected by any external tension forces like in the liquid case and, hence, special care is not required for it. The main problem with this method is that etching happens non uniformly (see Fig.3.4), the process produces very rough surface. The etch-rate varies along the sample and may not be the same in different directions. This happens because the process can not be controlled very accurately and the conditions may change during the etching, so there is a need in regular calibration. The technique works well for Si-based devices used in commercial production and is not suitable for our purposes.

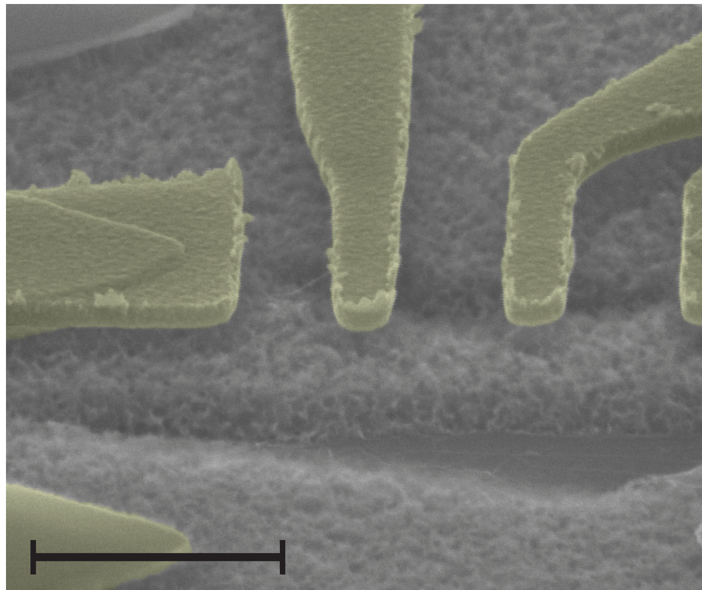

Figure 3.4: False color SEM micrograph a device etched with HF vapor. Yellow colored parts represent metal contacts. Scale bar corresponds to 3μm.

For the majority of our devices we performed wet chemical etching in buffered oxide etching (BOE) solution, that contains hydrofluoric acid and ammonium fluoride (NH_4F). These two components, NH_4F and HF, have the concentrations in water of 40% and 49% respectively and are mixed in BOE solution in the 6:1 proportion, so the

total concentration of HF is then 7 %. Compared to concentrated HF, BOE has slower etching rate allowing better control of the process. When the sample is submerged into BOE solution, the reaction takes place as follows:

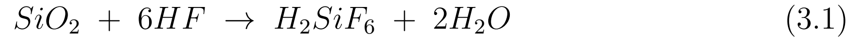

$$SiO_2 + 6HF \rightarrow H_2SiF_6 + 2H_2O \tag{3.1}$$

This etching procedure is known to be dangerous due to toxicity and harming effect of HF on bones and should be performed under certain conditions following all the safety precautions. For this reason we used beakers with HF resistive material: the material is polytetrafluoroethylene (PTFE) is usually recommended for this purpose.

Our experiments were done using the set-up shown on the Fig.3.5. Three beakers, respectively for BOE solution, ultra-clean water and Isopropanol (IPA) are set on the tray. We use sample holder made from PTFE material that has flat support at the bottom where the device is situated (illustrated on the left). On the support the device

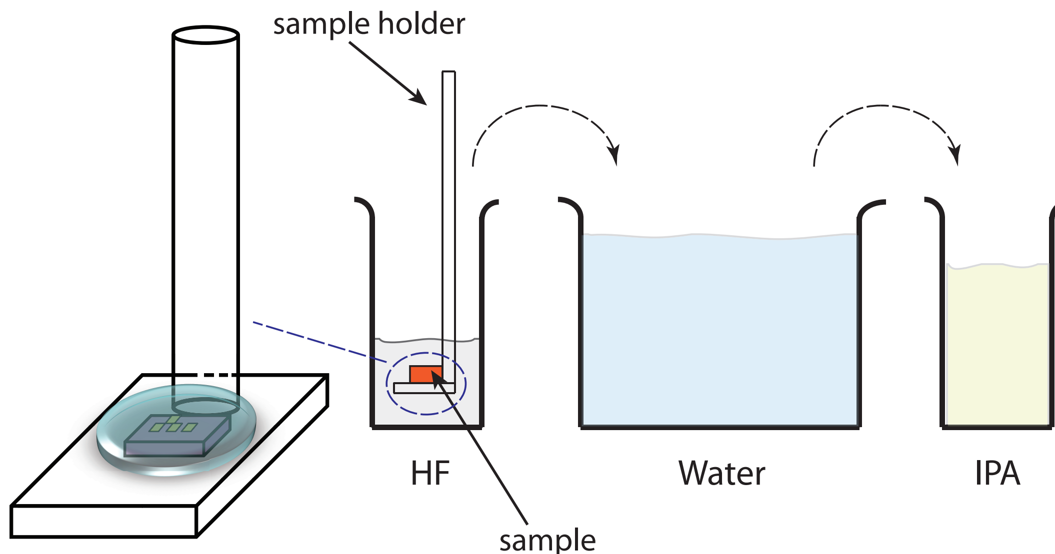

Figure 3.5: Illustration of the set-up used for etching oxide layer in HF solution. The sample holder is shown on the left in the figure. The blue semi-sphere demonstrates the full coverage of the sample with a liquid droplet.

is placed close to handle in order to reduce the effect of capillary forces (explained below). The holder is gently submerged into the beaker with HF. At this stage one need to know the time to etch SiO_2 up to a wanted depth. Usually the calibration of etching time is done on test samples; the step-height is calibrated with AFM or surface profiler. We need to mention that etching speed depends on the ambient temperature.

The calibration curve, i.e. penetration depth as a function of etching time, is shown in Appendix-III. The measurements were done at room temperature ($\sim 20\ ^0$C). Also, one should take into account that buffered oxide etching solution has a trend to degrade with time and the etching rate may change. Therefore, the calibration need to be done periodically. To our expertise, if the bottle with HF solution was not used within one year it is required to be replaced by freshly new one.

Once the time is settled, we gently agitate the sample holder to assure uniform etching while keeping the device inside HF beaker. Then, the sample is transferred to the beaker(made from PTFE) containing purified water. It is better to use shallow beaker with big volume for quicker dissolving of remained HF and residual product of the reaction (eq.4.1). After keeping in water for some time, the next transfer is done to the beaker with IPA (does not need to be PTFE material). The surface tension of water is known to be very strong ($\sim$72 dyn/cm at room temperature) and can easily rupture the flake. However, when the sample is placed next to the handle, capillary forces interacting with handle's surface maintain the big liquid droplet that completely covers the whole device (demonstrated on Fig.3.5 on the left) preventing, thus, pulling down the membrane.

Special care has to be taken during the final drying process of the sample in order to prevent a collapse of the graphene by capillary forces. A common solution to this problem is to dry the samples in a critical point dryer (CPD) [60] - making use of the zero surface tension in the supercritical transition of CO_2. Instead, we used an alternative route to dry the samples, which produces much cleaner devices compared to those dried by CPD. It is based on a fact that both surface tension and capillary forces tend to decrease with increasing the temperature. For instance, room temperature IPA has surface tension 21.7 dyn/cm and at $T = 70^0$C it drops down to about 15 dyn/cm. Therefore, in order to reduce the surface tension the beaker containing the sample in IPA is wormed up on a hot-plate to 80^0C (this temperature is close to the boiling point of isopropanol). The sample is kept inside for 5-7 min. Then it is slowly removed with tweezers and placed on a thick peace of clean glass slide, that was heated up to the same temperature, and leave the device dry in atmosphere while the glass is slowly cooling down. This procedure invariably delivers suspended graphene samples with flakes as large as 3μm wide and up to 2μm long. We have also applied this drying method with n-Hexane, which has lower surface tension at room temperature (18.4 dyn/cm).

However, thus far IPA delivered the cleanest samples after HF etching process.

In some cases we observed the formation of small crystals ($\sim 1\mu$m size) on the sample (see Fig.3.6a). Some of them may accidentally seat on a flake and damage it. The crystals likely originate from the reaction of remains HF or H_2SiF_6 molecules with isopropanol components and have an organic nature, because when shone with an electron beam they evaporate within several seconds. The level of contaminations

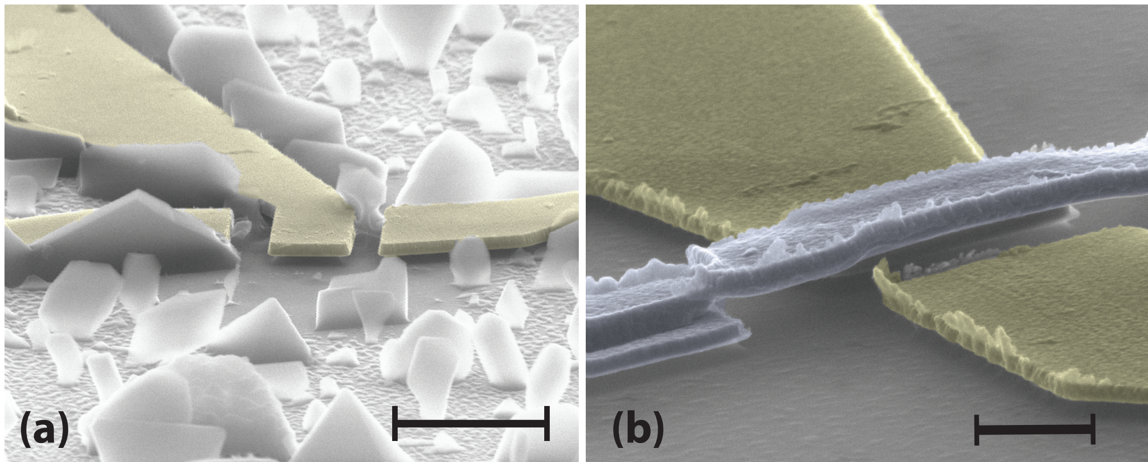

Figure 3.6: False-color SEM micrograph of the samples after final step of wet chemical etching. Two different samples in (a) and (b) were kept in ultra-clean water to dilute BOE for less than 1 minute and 3.5 minutes respectively. The parts painted with yellow/green color represent contact/top-gate electrodes. Crystal-like structures on (a) correspond to organic residue after HF reaction in water and IPA. Scale bars on (a) and (b) are respectively 3μm and 500nm.

was found to be correlated with water volume and the dilution time when the sample is kept in the middle beaker. On the Fig.3.6(a) and (b) one may compare the results of two different dilution time. The sample on (a) was kept in water for less than 1 min, whereas another one, represented on (b), was submerged into water for 3.5 minutes. As one can see there are no "crystal"-like structures on the specimen indicating that big portion of the residue after chemical reaction was dissolved in water.

It was also found [60, 79] that HF reacts differently with bare SiO_2 and one covered by graphene flake. The acid etches the regions, covered by graphene, much faster than the bare SiO_2 regions, even if the flakes are masked with chrome/gold metals. Hence, this fact should be taken into account when patterning contact electrodes. It is recommended to make source and drain contacts at least 700 nm (350 nm from each side) wider than the width of the flake allowing for the isotropic wet etching of bare SiO_2. Due to complete underetching of graphene, in order to make the system

mechanically stable thick metal layers are evaporated : 10/100 nm of Cr/Au*. On the

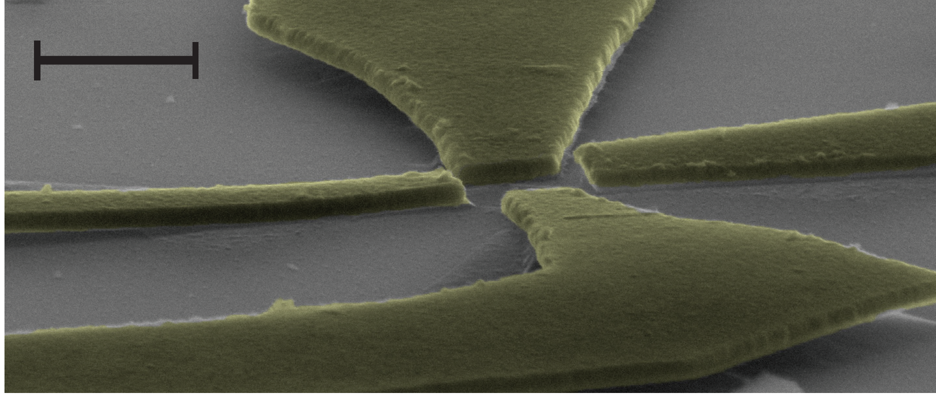

Figure 3.7: False-color SEM micrograph of collapsed contacts. Scale bar corresponds to 1μm.

Fig.3.7 one can see the example when the contacts are collapsed after wet etching of SiO_2. They pulled down by graphene.

The technique of making suspended membranes was proven to be very reliable when the distance between contacts is $\leq$1 μm. Remarkably, we can produce suspended samples larger than this size provided that we pattern auxiliary contacts aimed to support the flake. An example of suspended six-terminal bilayer device is shown on Fig.3.8(a). The length of the flake is about 3 μm and the width is 1.5 μm. Moreover, the samples with specific shapes like Aharonov-Bohm (AB) rings (Fig.3.8(b)), which were shaped beforehand by reactive ion etching, can be also suspended. Being stretched and supported simultaneously these devices demonstrated mechanical stability (there was no signature of rolled up edges).

3.5 Improving the quality of the samples

Generally, as-fabricated, samples are not of good quality. It is reflected immediately when implementing $R(V_{bg})$ measurements - the neutrality point is usually slightly shifted away from zero-voltage point. Often, additional peaks appear on the curve indicating sample's inhomogeneity due to impurities and charge puddles (see black curve on Fig.3.14). Besides, the presence of electron-hole puddles is responsible for

*Chromium is known to be strong metal, whereas gold is soft. When evaporated for leads, one should allow for contact resistance that will be higher for thicker Cr layer. 10 nm was found to be an optimal thickness.

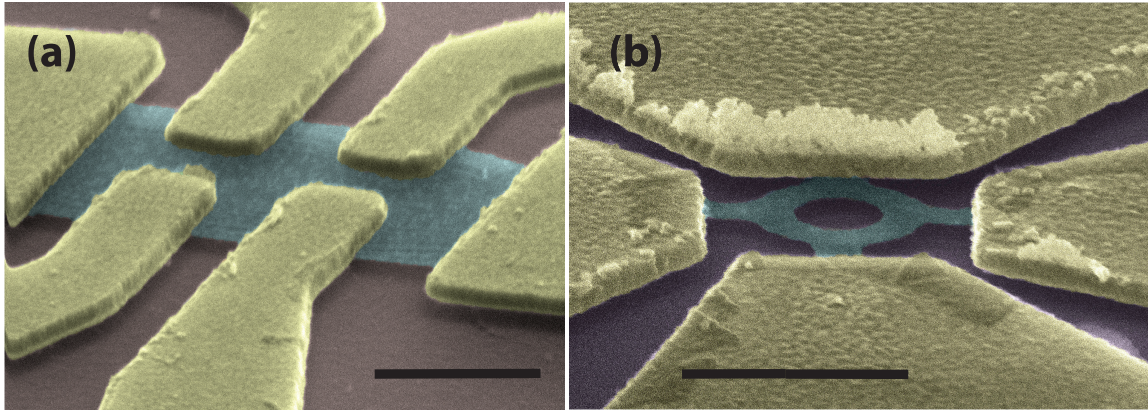

Figure 3.8: False-color SEM micrograph of (a) suspended bilayer sample with Hall-bar geometry of the contacts, (b) suspended Aharonov-Bohm graphene ring. Scale bars correspond to 1μm.

the reduced resistivity at the neutrality point [80, 81] and the modification of density of states at low carrier concentration (around maximum resistance the R-V_{bg} curve is spread) as well as the decreased carrier mobility. The chemical residuals left on graphene during the fabrication, i.e. undissolved polymers (PMMA/PMGI), MF-319 developer (sparingly soluble in water), organic solvents (IPA, Acetone), and the last - remained components of wet chemical etching process are the most likely cause of surface contamination. Therefore, in order to improve the quality of the samples which still remain relatively poor after the fabrication steps one need to perform an annealing procedure. Here we consider two different annealing methods.

3.5.1 Thermal annealing

In the experiments we tried thermal annealing processes in different environments: under high vacuum, in helium or H_2/Ar atmosphere. In the latter case, the device is placed into big glass tube which is covered by the lead of an annealing furnace (Fig.3.9). The annealing temperature ranges from 20 to 1100 ^{0}C. The gas mixture of 5%:95% hydrogen/argon (alternatively 10%:90% mixture can be used) comes through PTFE tube into the main tube with the sample where it is heated. The outcoming gas is passed through a liquid scrubber in order to stop a back stream. The pressure is monitored via gauge and controlled by the valve. The temperature is gradually swept from RT to 250-300 ^{0}C and then left to anneal for 2 hrs at final temperature. We do not exceed this range, otherwise the contacts might be damaged. This annealing technique, however,

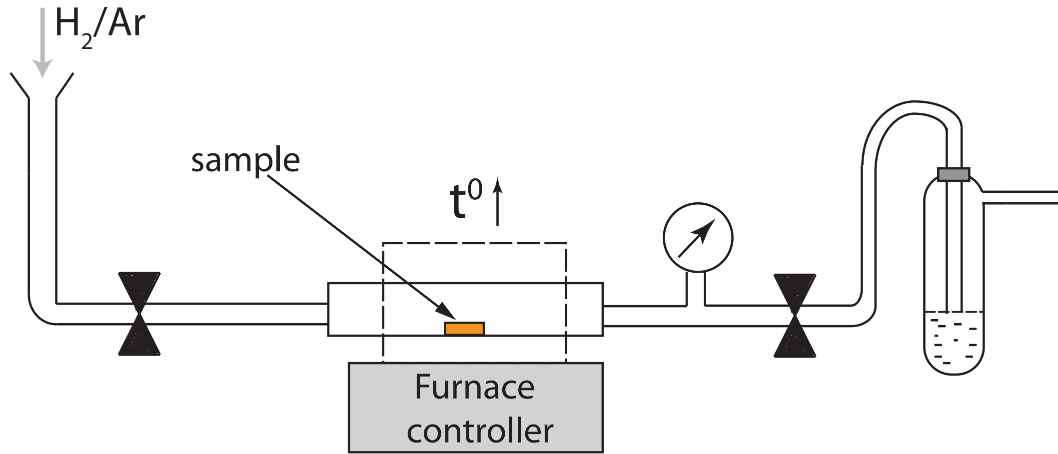

Figure 3.9: Scheme of thermal annealing set-up in furnace.

did not show noticeable improvement in transport properties of after-fabricated samples and, perhaps, need to be investigated thoroughly. Nevertheless, the AFM topography analysis done in our lab [82] showed that the annealing in furnace at 350^{0}C removes PMMA molecules (according to estimated step-height) and the surface roughness after the annealing was very close to that of pristine graphene. This method is suitable to clean the flakes that do not have metallic contacts on it, when the temperatures higher than 400 ^{0}C can be used for a long time. Many groups employ it for cleaning boron nitride and graphene flakes as an intermediate step in transferring fabrication technique of high-quality devices.

Thermal annealing in vacuum or in clean helium atmosphere, instead, is performed in a sample probe and does not involve very high temperatures. A sample in a chip carrier is mounted into the probe which contains a heater under the chip holder. The probe can be then placed either in a metal shell with a clamp and pumped further to high vacuum ($\sim 10^{-5}$-10^{-6} mbar) or at the very top of a helium dewar. The temperature is gradually increased up to 100-120 ^{0}C by applying voltage to the heater. While keeping at this temperature for $\sim$ 1-3 hrs the resistance is constantly monitored. Depending on the sample, the evolution of the resistance (i.e increasing/decreasing) as a function of time might be different. The annealing is usually stopped when the saturation region is reached (see Fig.3.10). If we continue the heating after reaching the saturation region for longer time, we observe oscillations of the resistance (with an amplitude of $\sim$ hundreds Ohms), indicating the degradation of the contacts. The advantage of this annealing approach is that the measurements can be done in situ,

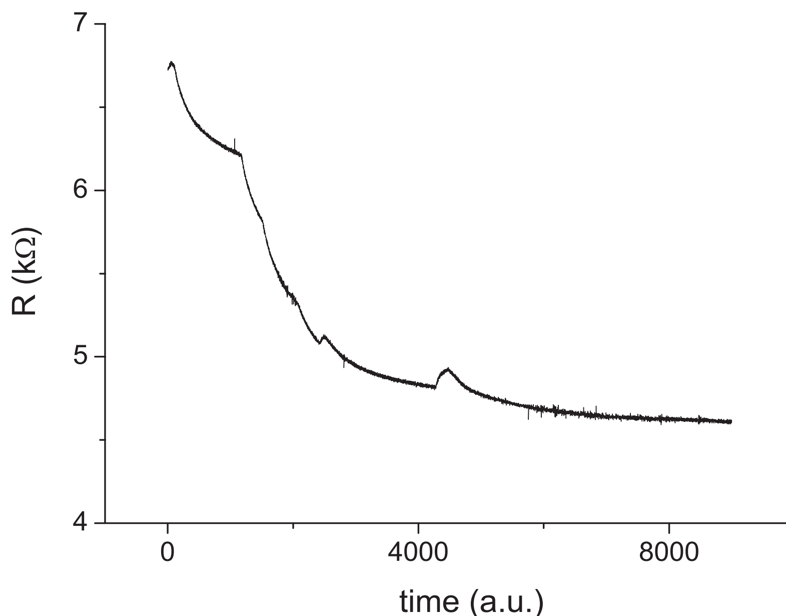

Figure 3.10: Typical "annealing curve": resistance as a function of time during thermal heating at 120 ^{0}C.

unlike the method with H_2/Ar gas, where, after the annealing, the sample is taken out and exposed to the atmosphere. On Fig.3.11 the R(V_g) curves, measured at $T = 4.2$K, before(red) and after(black) annealing performed in helium environment are shown.

This cleaning process makes the samples more homogeneous and reduces the doping level by shifting the charge neutrality point closer to zero gate voltage. Unfortunately, it does not significantly increase the mobility (usually not more than the factor of 2). The reason is that during the thermal annealing the temperature distribution is uniform over the whole surface and we usually do not exceed 300 ^{0}C in order to avoid damaging contacts. However, this low annealing temperature might be not high enough to remove all the remnant contaminants that require higher energies to be desorbed from the graphene's surface. The problem can be solved by implementing current annealing, where released Joule heating introduces locally much higher temperatures on the flake while the temperature on the contacts is substantially smaller due to heat dissipation determined by heat transfer process * and radiative losses.

*Metal contacts act as a heat sink

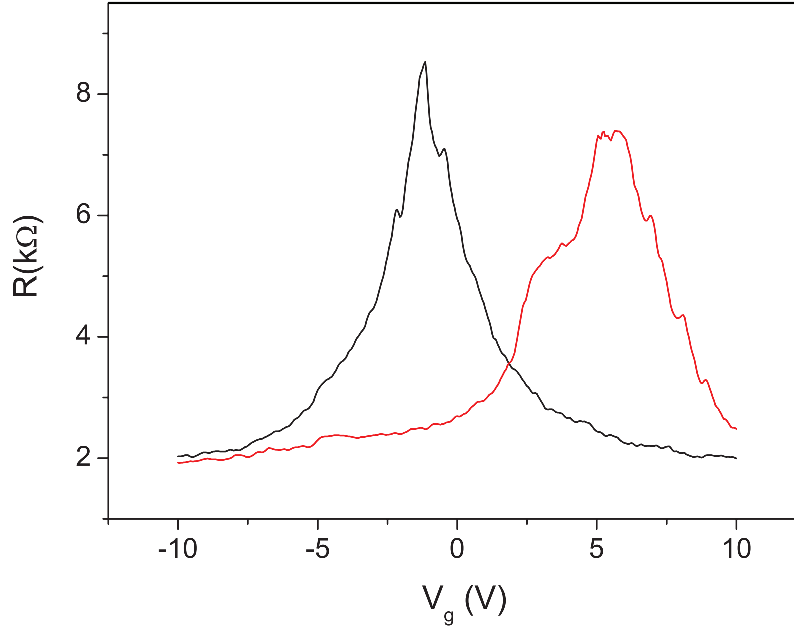

Figure 3.11: Resistance vs back-gate voltage for the sample before(red) and after(black) thermal annealing at T = 120^{0}C. The measurements were performed at T = 4.2K.

3.5.2 Current annealing

Current-induced cleaning technique was suggested to improve the quality of supported [83] and suspended [60, 61, 65] graphene devices. It is realized by passing very large current between source and drain electrodes. Compared to thermal annealing, this method is not safe for the device and can not guarantee for sure that it will survive after this procedure. Nevertheless, the technique was demonstrated to be a successful way of the device treatment and is used by many experimental groups [62, 63, 84, 85]. The graphene's temperature reached in the process can be higher than $\sim 600^0$C [83,86].

The circuit for current annealing, used in our experiments, is represented on the Fig.3.12. We have tried two slightly dissimilar ways of implementing this technique. The first one is done by ramping the voltage (DC source) across the flake with a sweeping rate $\sim$ 10 mV/s up to a predefined set-point, waiting for several seconds and then decreasing the voltage to zero using the same rate. The applied current is constantly monitored via "Keithley 2400" which we used as a voltage source. After the cycle is finished, we measure the sample's resistance as a function of back-gate voltage to see the effect of annealing. Similar approach is commonly used by other groups [60, 84, 85].

At the beginning of the development of this method we tested it first on the sup-

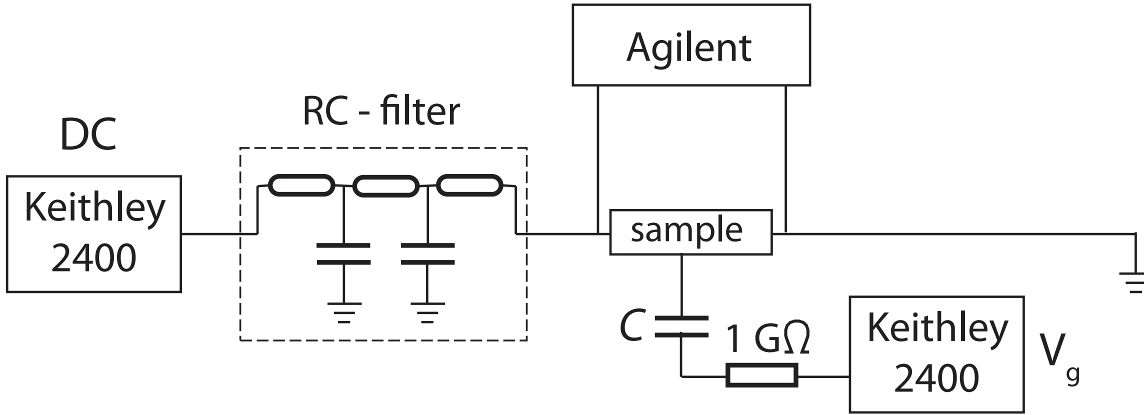

Figure 3.12: Circuit for current-induced cleaning method. The RC-filter has total resistance 30 kΩ and the time constant ∼300 ms. The back-gate voltage is applied by "Keithley 2400" (voltage source) through 1GΩ resistor, served as a filter.

ported samples. Overall, six supported bilayer graphene devices were tested. The result of current annealing demonstrated the opposite effect - the curve's peak was shifted far from its initial position towards higher negative gate voltages, indicating considerable n-doping. There was no sign of the mobility increase as well. Typical picture for a post-annealed device is shown on Fig.3.13. Our results are contrasted to those obtained by Bachtold *et.al.* [83], who suggested this cleaning method first for supported samples. They successfully removed most of the residues remaining on the surface of the flake (was checked by AFM topography scan) and improved the performance of electrical transport, but the mobility was not appreciably enhanced. Most probably, the impurities are trapped between the sample and the oxide layer, precluding desorption, evaporation or sublimation etc. of dopants. Also, an additional n-doping can arise from the degassing of the chemical impurities, oxygen and water molecules, trapped into SiO_2 during the fabrication steps and released from the oxide surface due to Joule heating. This current annealing method, though, works well for suspended devices.

The second approach of current annealing technique is implemented by sending short (∼ 1-3 sec.) current pulses across the device, similar to Ref. [87]. At the beginning, R-Vbg characteristic of a non-annealed sample is measured in the following configuration(see Fig.3.12). Small DC voltage (∼3mV) is applied to the sample through the RC-filter* that has total resistance 30 kΩ, so that the current corresponds approxi-

*to prevent from accidental spikes

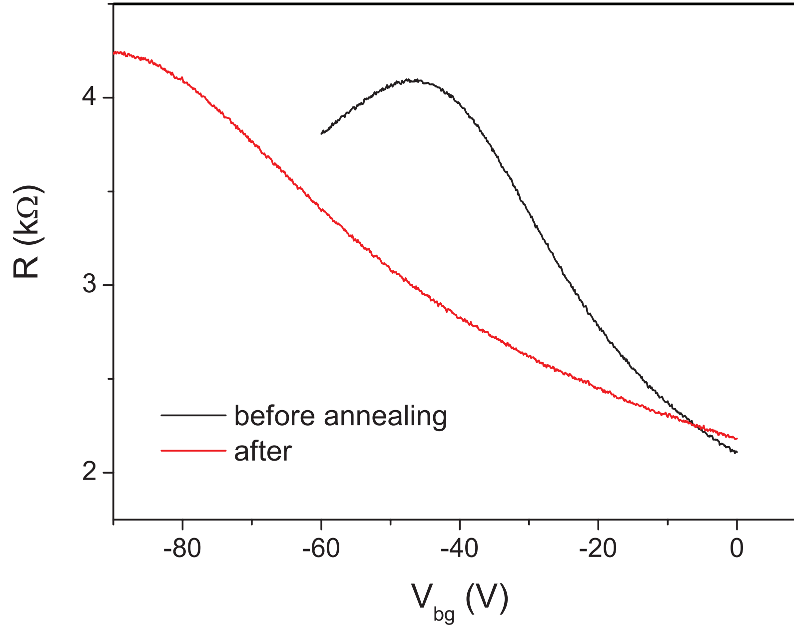

Figure 3.13: R(V_g) dependence of one of our sample, supported on SiO_2, before(black) and after(red) current annealing.

mately to the value 0.1 μA. By sweeping back-gate voltage we measure the voltage drop across the sample with the multimeter (Agilent-34410A), recalculate it into resistance and plot the R-V_g dependence. This gives an idea of resistance values for the range of applied gate voltages, which we then use for the estimation of the parameters of current annealing. Using a DC voltage source, we first deliberately apply a small voltage to the sample to estimate the current density ($j = I/W$, W is the width of the flake) and the voltage drop on the sample, which we compare to their critical values (will be discussed later). At the next stage, the applied net voltage is increased and obtained value of the sample's resistance is compared to previously measured one. If a significant change is noticed, than the R-V_g dependence is measured in the configuration described above. The procedure is repeated (the voltage is increased in steps) until the desirable result is achieved.

Both current annealing methods employed for our suspended graphene devices demonstrated successful results (see Fig.3.14). However, the pulse technique was found to be more convenient and efficient in the context of producing good result in a short period of time. For the majority of our suspended samples the latter method was used.

Since, during this annealing process, we send very large current, the amount of

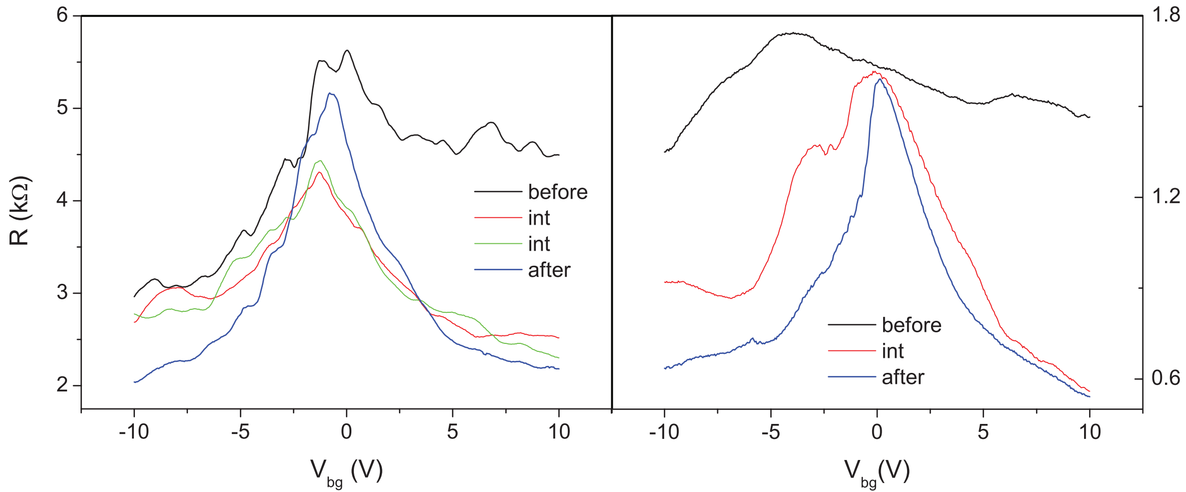

Figure 3.14: The effect of current annealing on different suspended trilayer graphene samples reflected on the dependence of the resistance as a function of gate voltage. The annealing was implemented by using (a) ramping technique, when current was gradually increased up to predefined value, and (b) pulse technique. "int" on the figure corresponds to intermediate step of annealing.

heat associated with the Joule heating can easily cause the break of the device. For this reason the procedure should be carried out carefully. There is a certain number of critical parameters connected to the breakdown limit of graphene samples. These parameters vary from sample to sample and the success of current-induced cleaning depends on the initial quality of as-fabricated devices. It was suggested that sample's breakdown limit correlates with the critical current density that was found to be 1-2 mA/μm in Ref. [60, 87, 88] and ∼0.5-1 mA/μm in Ref. [62]. The generated heat power per sample's area (P/LW) was considered to be also an important parameter [83]. During the annealing, along with the current density and normalized power (P/LW), we monitor also the voltage drop across the sample. In total, we annealed over 30 suspended multilayer devices using two different methods. In Appendix-IV the statistics of the samples destroyed by current annealing is shown. It was important to establish the range of critical values related to the breakdown point. Taking into account the experience of Ref. [60, 83] we chose the current density as an important quantity for the annealing and set the value 1 mA/μm as a "break point", after which the device was expected to be destroyed with high probability and further step of the increase in applied voltage was chosen carefully. Indeed, the statistics of broken samples showed that in 95% of the cases the breakdown current density was in the range from 1 to 2 mA/μm. Only one of our devices was destroyed at the current density slightly

higher than 2 mA/μm. The correlation was also found between the voltage drop across the flake and the breaking point, similar effect was reported in Ref. [86] *.

Using the circuit shown in Fig.3.12 the pulse annealing technique can be performed at various applied gate voltages. It was suggested to apply short pulses not only at zero back-gate voltage, which is eventually supposed to correspond to the neutrality point after successful annealing, but also at finite value of V_g. Presumably, shift of the Fermi level away from the charge neutrality point (NP) should reduce the number of electron-hole puddles, which provides more homogeneous annealing. However, no considerable difference in the results was observed between annealing at V_g=0 or $\pm$10 volts. It is just convenient to perform it at a finite carrier concentration, because after each current pulse one can apply low bias voltage for a quick check of the resistance and notice improvement or decrease of the mobility†. Once spotted an appreciable change in V_s (voltage on the sample) between two subsequent pulses, we perform low-bias R(V_g) measurements. Even when the uniform shape of the curve is achieved there might be still some residual doping that shifts the NP slightly away from zero gate voltage. At this stage, if further improvement is required, we continue annealing at $V_g = 0\,V$ and monitor the resistance after each pulse until we notice the enhancement of the resistance, indicating the shift of the curve peak to zero gate voltage.

The understanding of the interconnection between critical parameters and the mechanism of the device's breakdown is an important issue. We believe that the current density at which the annealing process is successful, final mobility and homogeneity of the device depend on its initial quality (before commencing the annealing procedure). For example, one of our ABA-stacked trilayer sample straight after the final fabrication step demonstrated very smooth and almost symmetric R(V_g) curve with a little shift ($\sim$ 0.9V) of the neutrality point. It has an as-fabricated mobility of about 16 000 cm^2/Vs, which was then enhanced up to 28 000 cm^2/Vs with just two applied current pulses. Many suspended samples were destroyed yet by current annealing. After being broken the devices were checked by optical or/and electron microscope. Some of them were exploded with adjacent metal electrodes (the example is shown on Fig.3.15) and

*The found values of V_c in our experiments $\sim$ 2-3 mV, depending on the sample's geometry and its initial quality.

†According to eq.(2.1) it is inversely proportional to the resistance at a given carrier density and, thus, decrease/increase in the mobility is reflected on the increase/decrease of the resistance at the "tails" of the R(V_g) curve

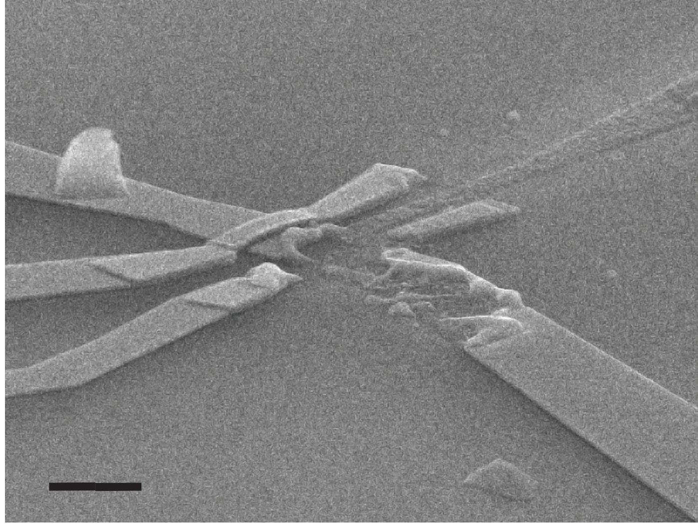

Figure 3.15: SEM image of the device exploded during current annealing. Scale bar corresponds to 2μm.

the others broke without damaging the contacts. Interestingly, the explosion of the contacts was observed mainly for thicker flakes ($W > 0.8\,\mu$m). There are several possible mechanisms of sample's destruction suggested in the literature: it might be caused by graphene oxidation [89], sublimation of carbon atoms at high temperature [90, 91] or electromigration [87, 92]. The explosion of the flake together with contacts can be initiated by one of these mechanisms, when the defects induced by sublimation or oxidation introduce additional scatterers, which increase the resistance. The heat power is then increased, which, in turn, increase the temperature on the sample and enhance this effect. The triggered process may suddenly increase the temperature on the flake within 1-2 seconds and produce the blast.

The degradation of some samples was noticed (Fig.3.16) during the process of current annealing, when a certain voltage was reached - the carrier mobility started to decrease and the R(V_g) curve became non-uniform. It is attributed to the contamination of the flake by dopants, which are desorbed from the SiO_2. New contaminants need another annealing pulse which also causes more dopants desorption from the oxide layer. This effect is cumulative. Taking these facts into account we come to the conclusion that the total time of current annealing (as well as the number of current pulses) plays essential role in this process.

The experiments and analysis of current induced cleaning, described above, were performed on multilayer graphene samples, mainly on trilayers, and further investiga-

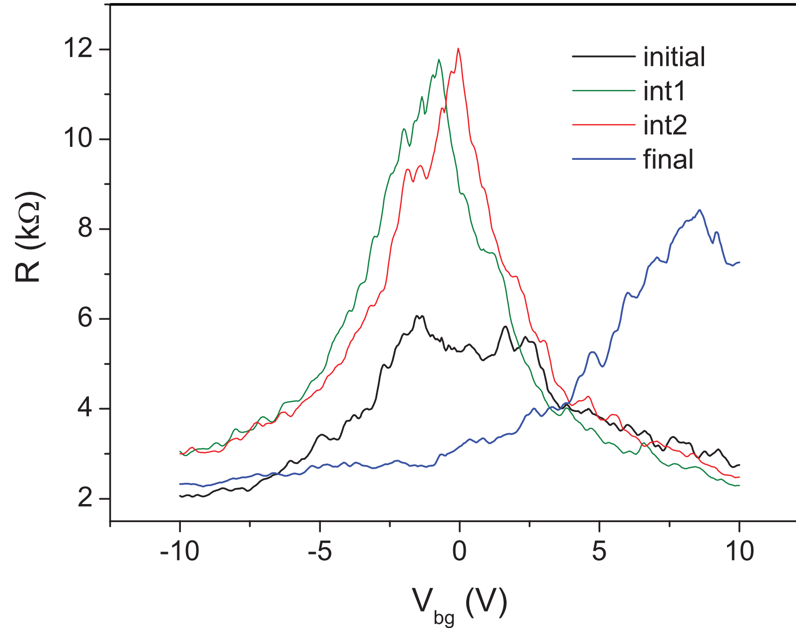

Figure 3.16: The example of the current annealing, when after a certain stage, the transport properties of the sample started to degrade until the total failure of the flake, represented as an evolution of the resistance as a function of gate voltage. Black and blue curves correspond to first and final annealing steps respectively. "Int1" and "Int2" represent two intermediate steps of annealing.

tion in determination of critical parameters, including temperature, should take into account the number of layers and the length of the devices. A detailed study, addressed to the reason of sample's failure, requires the consideration of a certain model with the solution of the heat equations etc. and is beyond the scope of the present work. Here is a summary of the recipe for the current annealing with pulses, which we found reasonable :

(1) With the circuit, similar to one on Fig.3.12, apply the voltage from the DC source of $\sim$ 3mV so that corresponding value of the current is close to 100 nA. Sweep the back-gate voltage between -10 and 10 volts to measure and plot the R(V_g) dependence for the estimate of mobility etc.

(2) Bring V_g value to -10 V (or +10 V) depending on which branch of the curve has higher resistance allowing for that R(V_g) characteristic should be symmetric in the ideal case.

(3) Apply short voltage pulse (1 sec) of small magnitude (1-5 V) and using measured value of the voltage on the flake (V_s) estimate the current density.

(4) Taking into account the results obtained in the preceding stage, calculate the voltage required for the next annealing pulse, which will correspond to the value of V_s (or j) close, but still not exceeding, its critical value ($j_c = 1mA/\mu m$ and $V_s = 2V$).

(5) Apply voltage pulse with the value estimated in the stage (4). If the resistance was changed considerably do measurements described in (1) and compare the results with those obtained in previous steps.

(6) Repeat the procedure (3)-(5), increasing in each following stage applied net voltage until the progress is noticed. Important: when approaching critical values of V_s and j the augmentation of applied voltage in the next step should be chosen carefully (for example ~0.1-0.4 volts).

(7) Try to minimize the number of annealing steps (voltage increase) as far as it possible.

At last, we want to mention the failure of implementing any of two current annealing methods on suspended multi-terminal samples (like those on Fig.3.8). The same result was previously reported in Ref. [62]. The problem is that the potential metallic contacts, that cover the area at the edges of the flake, bend the electric field lines during the annealing. This impedes homogeneous current flow across the whole flake, thus leaving charge puddles in the surrounding area of the contacts. Similarly, the current flow in graphene AB-ring is non-uniform, because this geometry introduces electrical circuit with parallel resistors - each half of the ring, where the charge is randomly distributed. This problem can be partially solved by performing thermal annealing of suspended devices in the probe before current-induced cleaning technique and hexagonal boron nitride can be used as an alternative solution of making high quality multi-terminal samples. Consequently, there is still a way forward in improvement and amendment of current annealing method to make it more reliable and possible for samples with non-standard geometries

3.6 Results

The combination of two methods - fabrication of stable air-bridge gate electrodes and wet chemical etching involving IPA drying technique - provides a high yield of sus-

pended dual-gated graphene samples. Fig.3.17 demonstrates our typical devices. On the bottom right image the contrast of the flake was enhanced intentionally for the clarity, since the suspended gate electrode covers the whole area of the flake between source and drain contacts, which makes the flake difficult to visualize under different angles.

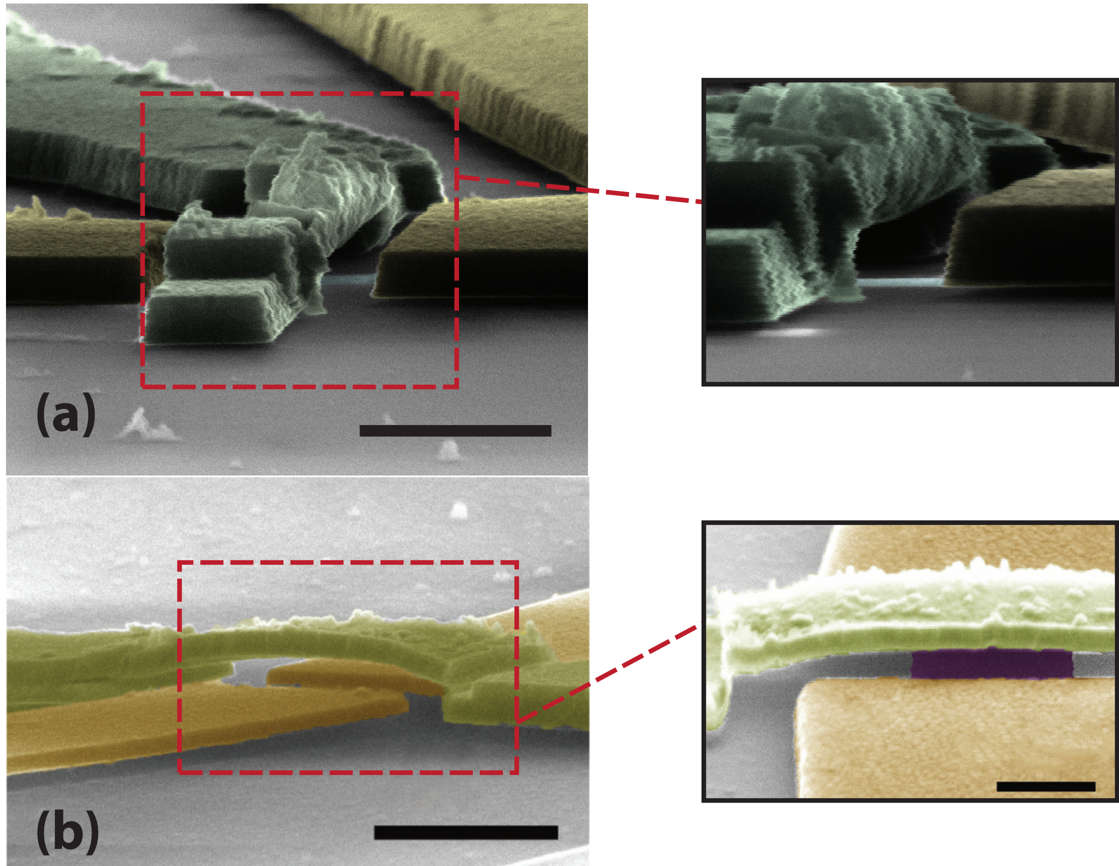

Figure 3.17: False-color SEM micrograph of suspended double-gated graphene devices. Yellow/green color correspond to metal contacts/gate electrode. Scale bar on (a) and (b) correspond to 1μm. Images on the right-hand side represent framed regions on (a) and (b) respectively (for the bottom right image the scale bar corresponds to 500nm), that were taken from different perspective.

Even pre-annealed multilayer graphene samples, measured straight after the fabrication, had relatively high carrier mobility, started from $\sim$ 5000 cm^2/Vs for concentration $n \approx 5\,10^{11}$ cm^{-2}, while the highest experimentally found mobility, for example, in trilayer graphene on SiO_2 was less than 4000 cm^2/Vs for the same carrier density [17,93,94]. With implementing current annealing *in situ*- i.e in high vacuum (10^{-6} mbar) and at low temperature T = 4K - the device's performance in electrical transport can be significantly improved. Typical mobilities, found for our post-annealed bi-

and tri-layer suspended dual-gated graphene samples, ranged from 14 000 up to 110 000 cm^2/Vs. On Fig.3.18(b) one can see the R(V$_g$) dependence of our bilayer device which has very high mobility (shown on Fig.3.18(a) as a function of carrier concentration). The latter was calculated by using eq.(2.1), where we took into account the resistance of the wires in the probe, that were measured to be $\sim 300\Omega$ for each contact. Unfortunately, we could not exclude the contact resistance, since the measurements were taken in two-terminal configuration. Thus, found values of carrier mobility are underestimated.

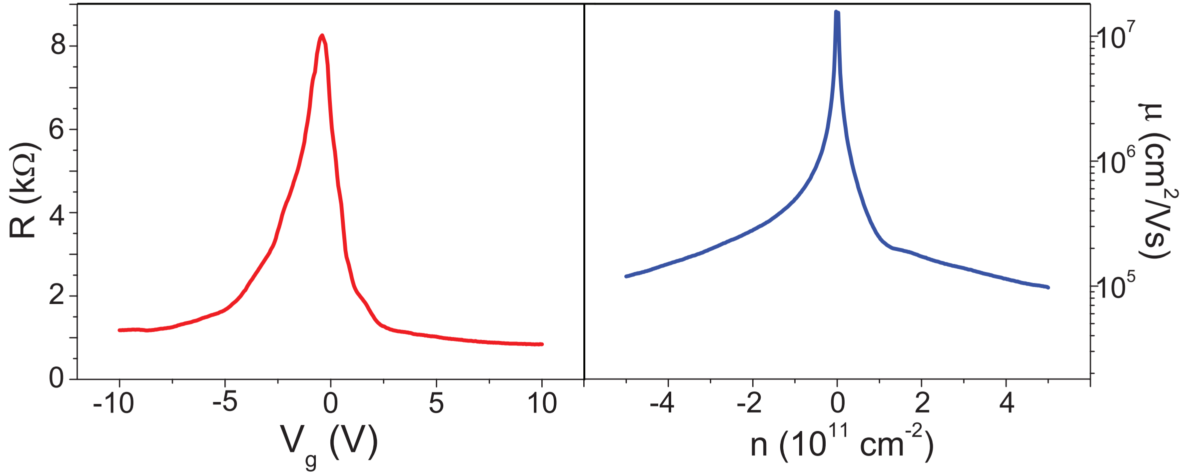

Figure 3.18: (a) Resistance as a function of back-gate voltage for bilayer sample. (b) Mobility as a function of carrier concentration. The data are taken at $T = 4.2K$.

We have characterized electrical properties of ABC-stacked trilayer samples, measuring the resistance as a function of back-gate voltage for various fixed top-gate voltages with standard lock-in technique in a current configuration (see Chapter2, Sec.2.2) and in the linear regime -i.e. the excitation current was varied to ensure that the voltage drop across the sample was smaller than the temperature broadening of the Fermi distribution. The two-terminal measurements performed at $T = 0.3K$ are shown in Fig.3.19a. It is apparent that the maximum of resistance increases with increasing the external perpendicular electric field. This observation is consistent with the opening of an electric field induced band gap in the energy dispersion of rhombohedral trilayer graphene (Chapter1, Sec.1.4). The high quality of these samples is demonstrated by the fact that we observe a particularly high on/off ratio of the current (Fig.3.19c). If we define the average electric displacement as $D = (D_{bg} + D_{tg})/2$ [95] with $D_{bg} = \dfrac{\varepsilon\varepsilon_0}{d\,(\varepsilon + \varepsilon_0)} V_{bg}$, which we determined using parallel capacitors model, and

$D_{tg} = V_{tg}\varepsilon_0/d$ (d = 150nm, $\varepsilon_0 = 1$ for air and $\varepsilon = 3.9$ for SiO_2), we find that I_{on}/I_{off} equals 250 for D ≈0.08V/nm. The I_{on}/I_{off} value found in our ABC trilayer devices is twice as large as previously reported in supported double gated bilayer graphene samples [96] for approximately the same electric displacement.

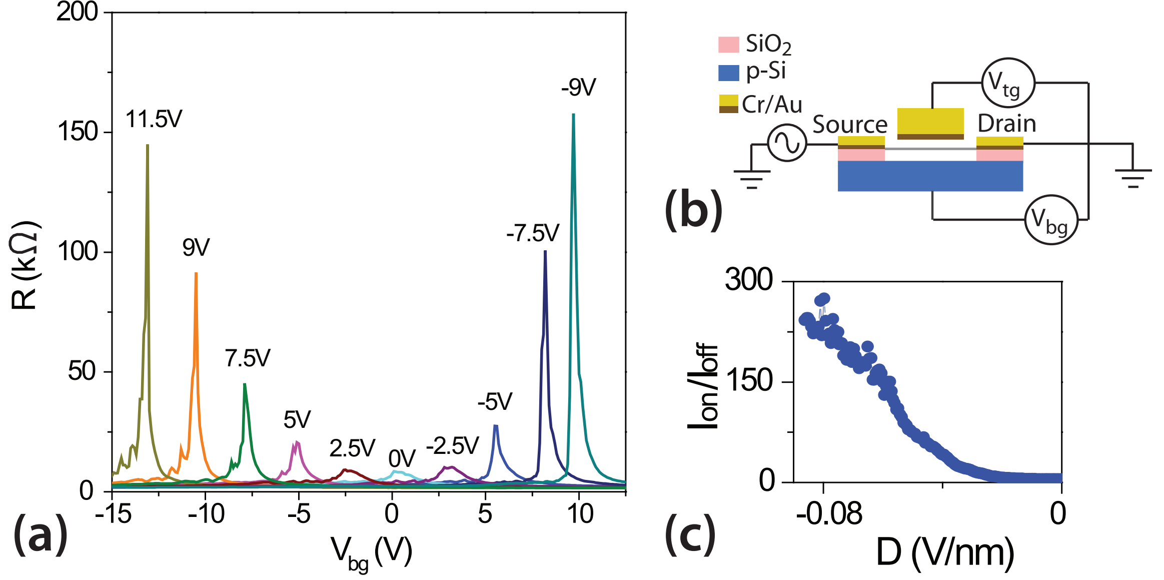

Figure 3.19: (a) Resistance versus back-gate voltage measured at T = 0.3K for different values of fixed top-gate voltage (V_{tg}) as indicated in the graph. (b) Schematic cross section of a suspended double gated device and the electrical measurement configuration. (c) Measurements of the on/off ratio of the current as a function of the average electric displacement D (see main text).

Electrical transport measurements in perpendicular magnetic field reveal the formation of Landau levels (LLs) starting from 0.5T, with the appearance of quantized plateaus in the conductance (see Fig.3.20). Experimentally we find that the unique quantization sequence of the rhombohedral trilayers $G = \pm 6, \pm 10, \pm 14, \pm 18...$ becomes clearly visible at magnetic fields as low as 0.9T. The identified values of the filling factors of Quantum Hall plateaus are $\nu = 6, 10, 14, 18$ with $\nu = n_s \phi_0 B^{-1}$ (ϕ_0 is the flux quantum, n_s is the charge carrier density and B is the magnetic field), that is consistent with theoretically expected numbers that stem from from the 3-fold degenerate zero-energy LLs of the ABC-stacked trilayer graphene with 4-fold spin and valley degeneracy (Chapter1, Sec.1.6.5). Interestingly, the plateau at $\nu = \pm 18$ was not observed before on ABC trilayers on SiO_2 even at magnetic field higher than 20 T. The problem concerning QHE in multilayer graphene will be considered in details in Chapter5.

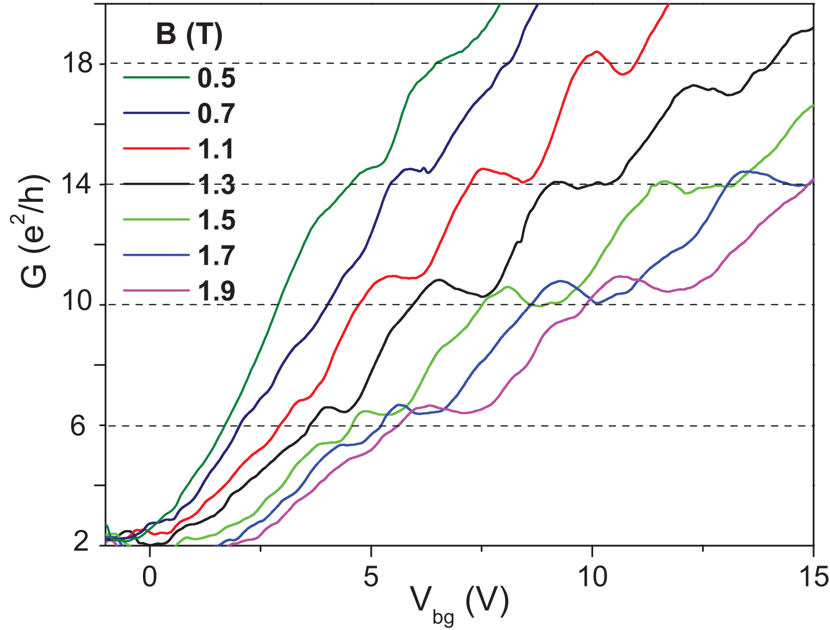

Figure 3.20: Conductance (G) vs. back-gate voltage measured for different values of perpendicular magnetic field.

3.7 Conclusions

In this chapter we analyse many different fabrication methods of high quality graphene-based samples. We demonstrated very reliable and well developed technique of producing ultra-clean suspended dual-gated devices with impressive performance [97]. Carrier mobility for our multilayer graphene devices ($N \geq 2$) is ranging from 14 000 up to 110 000 cm^2/Vs. We found the acceptable recipe of the current-induced cleaning technique which helps to considerably improve samples' quality. However, the improvements are yet to be done to make it reliable and there are still unanswered important questions concerning the reason and realized mechanisms of sample's breakdown.

Production of good-quality dual-gated graphene-based transistors opens new avenues to exploring graphene electronics, based on band structure engineering. Purity and high mobility of these devices make it possible to access the quantum Hall physics at magnetic fields which are 2 orders of magnitude smaller than previously experimentally reported in supported double-gated devices.

Chapter 4

Gate tunable band-gap in rhomboherdal-stacked trilayer

4.1 Introduction

A gate-tunable band-gap, characteristic of few layer graphene materials, is at the core of optoelectronics. So far, only infrared spectroscopy experiments have directly measured the value of this electric field induced band-gap in both AB-bilayers [31,98,99] and ABC-trilayers [32]. These experimental findings are contrasted by the lack of the direct observation of a tunable band-gap in charge transport measurements, where a transport gap at a very different energy scale has been reported [100, 101]. Proper consideration to the role of disorder induced sub-gap states can shed light onto this dichotomy between optical spectroscopy and electrical transport reports. In particular, the infrared absorption is largely dominated by the band-to-band transitions rather than transitions from the small density of disorder induced states (see Chapter1, Sec1.4.3 and Fig.1.7a). On the other hand, in electrical transport the hopping of electrons between sub-gap impurity states dominates the current flow hindering the observation of the intrinsic energy gap [102]. Indeed, the characteristic energy scale (activation energy) associated to the hopping conduction mechanism is related to the ionization energy of the sub-gap states and brings no knowledge of the intrinsic band-gap opened in the material. The direct observation of the FLG gate tunable band-gap in electrical transport experiments is still an open quest which prevents the development of graphene-based transistor applications.

In this chapter we demonstrate the evidence of direct observation of an electric field tunable band gap in rhombohedral stacked trilayer graphene by implementing electrical transport measurements on high quality suspended dual-gated devices, which result in the absence of any hopping mechanism assisting the electrical conduction. With a systematic study of the temperature dependence of the minimum conductivity in the devices it will be shown that conduction is due to thermally excited charge carriers over the energy gap and not to hopping between sub-gap impurity states. We found that the magnitude of the measured band-gap depends on the intensity of the external perpendicular electric displacement with values of 5.2 meV for an average electric displacement of -117 mV/nm. The values of the energy gap estimated from the temperature dependence of the minimum conductivity correlate well to the energy range of non-linearity measured in the current-voltage ($I - V$) characteristics.

4.2 Device characterization and description

ABC-stacked trilayer graphene flakes are obtained by micromechanical exfoliation of pristine natural graphite onto SiO2 (295 nm)/p-Si. "Kish-graphite" (Toshiba ceramics) was suggested as the best candidate to produce rhombohedral-stacked graphene flakes by "scotch-tape" method with high probability [103, 104]. The number of layers and the stacking order are identified by Raman spectroscopy. In particular, the 2D-peak of ABC-stacked trilayers is asymmetric as shown by the relative heights of the six Lorentzians fitted to it (Fig.4.1b)*. We follow the fabrication steps fully described in Chapter3 to produce suspended double gated ABC trilayer devices. The width and length of the top-gate electrode are larger than graphene area in-between source and drain contacts, therefore ensuring that a uniform electric field acts on the conductive channel. Produced samples are annealed *in situ* in the cryostat by applying the current density ~ 1.3 mA/μm (Fig.4.1d). Typically, the charge carrier mobility in these devices after current annealing is $\geq$ 20 000 cm^2/Vs at the charge density of $n \sim 5 \cdot 10^{11}$ cm^{-2}, with no appreciable residual doping (Fig.4.1d). The estimated mean free path is compared to the size of the sample ($L \approx W \sim$500nm, and $l_{MFP} \sim$200nm).

The independent control of the external perpendicular electric field acting onto the trilayer, which determines the opening of a band-gap (see Fig.4.1a), and of the charge

*For more details see Sec.2.3.2

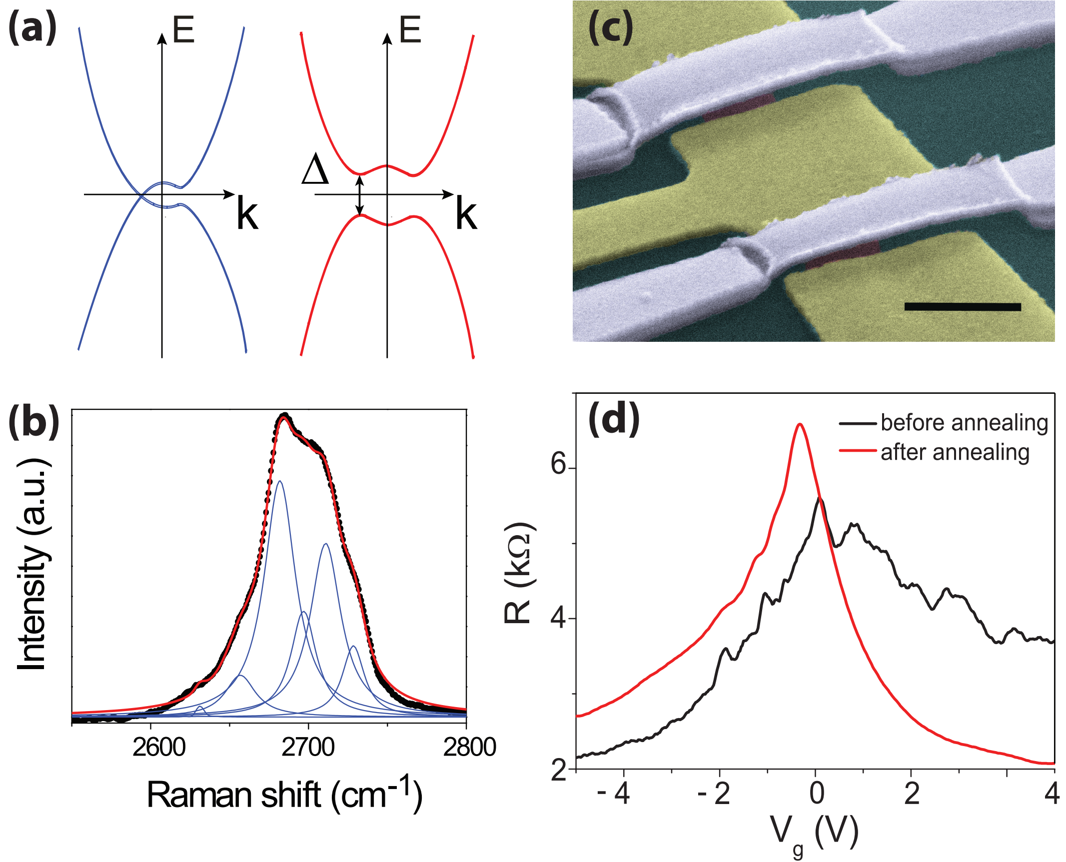

Figure 4.1: (a) Energy dispersion for ABC-trilayer with zero (left) and finite (right) external perpendicular electric field. (b) 2D-Raman peak for ABC-trilayer measured with a 532nmn laser. The dots are the experimental data points, whereas the red continuous line is a fit to 6 Lorentzians (continuous blue lines). (c) False-color SEM micrograph of suspended double gated graphene device. Scale bar corresponds to 1μm. (d) Resistance vs back-gate voltage before(black) and after(red) current annealing. The data are taken at T = 4.2K.

density is readily obtained in double gated devices by changing independently the two gate voltages*.

4.3 Low-T measurements

Electrical measurements were performed in a ^{3}He refrigerator (Heliox-TL) in the temperature range between 300 mK and 100 K. The conductance of the suspended double gated devices was measured using a lock-in amplifier in a voltage-biased two-terminal configuration. The experimental circuit is shown on Fig.4.2. The voltage applied to the

*For comparison, in IR spectroscopy experiment [32] there was no ability for an accurate independent control of the carrier concentration and an electric field. Thus, the energy gap was increased together with the lifting up the Fermi level, and low energy states between conduction and valence bands were inaccessible in this experiment.

sample is dropped down by a potential divider ($\times 10^{-5}$). The outcoming signal from the device passes through a current amplifier with an enhancement factor 0.1 V/μA. The measurements were performed in the linear regime (unless otherwise stated), where the excitation voltage was adjusted for each different temperature to prevent heating of the electrons and the occurrence of nonequilibrium effects.

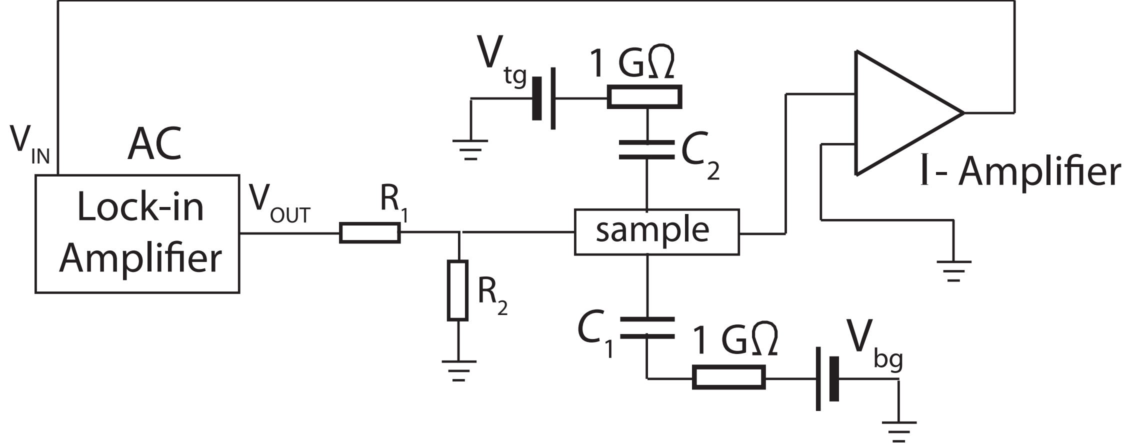

Figure 4.2: Electric circuit for low-T conductance measurements in a voltage-biased two-terminal configuration. The resistances R_1 and R_2 are 10 MΩ and 100 Ω respectively.

4.3.1 Resistance as a function of applied top- and back-gate voltages

Figure 4.3(a) and (b) show the resistance of the device, measured at 300 mK as a function of back-gate voltage (V_{bg}) for different fixed top-gate voltages (V_{tg}). Following Zhang *et.al.* [95] we define the average external perpendicular electric displacement as $D = (D_{bg} + D_{tg})/2$ with $D_{bg} = \dfrac{\varepsilon}{d_a\varepsilon + d_{ox}} V_{bg}$ and $D_{tg} = V_{tg}/d_{tg}$ (d_{tg}=150nm, d_a=85nm, d_{ox}=210nm and ε = 3.9 for SiO_2). Upon increasing D, the maximum of resistance (R_{max}) increases from 7.9 kΩ up to 1 MΩ and shifts its position in the gate-voltages (see Fig.4.3b). This dependence is summarized in the color plot of Fig.4.3a. Due to the gate voltage limitation in our devices the applied V_{bg} and V_{tg} ranged as indicated on the figure. We find that R_{max} moves linearly as a function of V_{bg} and V_{tg}, as expected for constant capacitive coupling to the two gates (see Fig.4.5a). At the same time, the temperature dependence of maximum resistance shows that the larger is electric displacement the more pronounced is the difference between the adjacent

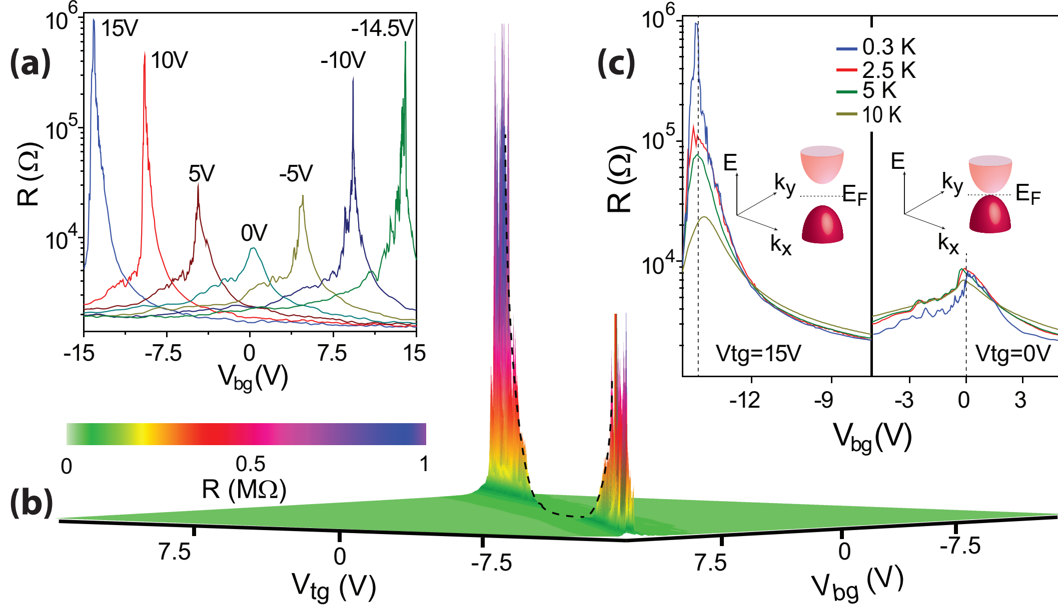

Figure 4.3: (a) Zero-bias resistance versus V_{bg} measured at T = 300 mK and for different fixed V_{tg} as indicated in the graph. (b) 3D Plot of R vs. V_{bg} and V_{tg}. The dashed line is a guide line connecting the maximum of resistance R_{max}. (c) $R(V_{bg})$ for V_{tg} = 15V (left) and V_{tg} = 0V (right) and for different temperatures, as indicated in the graph.

maxima (Fig.4.3c). Both the increase of R_{max} as a function of D and its pronounced temperature dependence at large V_{tg} suggest the opening of an electric-field induced band-gap due to the breaking of the inversion symmetry between the outer layers of ABC-trilayer graphene [15, 23, 30].

4.3.2 *I-V* characteristics and spectroscopy measurements

To gain further insight into this effect, the measurements of current-voltage ($I - V$) characteristics and differential conductance as a function of V_{tg} and V_{bg} are performed with the set-up represented on Fig.4.4 at T=300mK. We apply 30μV to the sample from the AC source and swept the source-drain voltage(V_{SD}^{DC}) between -10 and 10 mV (the potential divider was used as shown on Fig,4.4). The signal is then amplified by the factor 0.1 V/μA. The inset in Fig.4.5a shows I-V curves for three different perpendicular electric fields configurations highlighted in the color plot. In all cases, the I-V curves display an insulating state at low V_{SD} bias, though for very different ΔV_{SD} ranges. In particular, ΔV_{SD} decreases with decreasing D, i.e. $\Delta V_{SD}^{I} < \Delta V_{SD}^{II} < \Delta V_{SD}^{III}$. Correspondingly, the differential conductance (dI/dV) measured as a function of V_{sd}

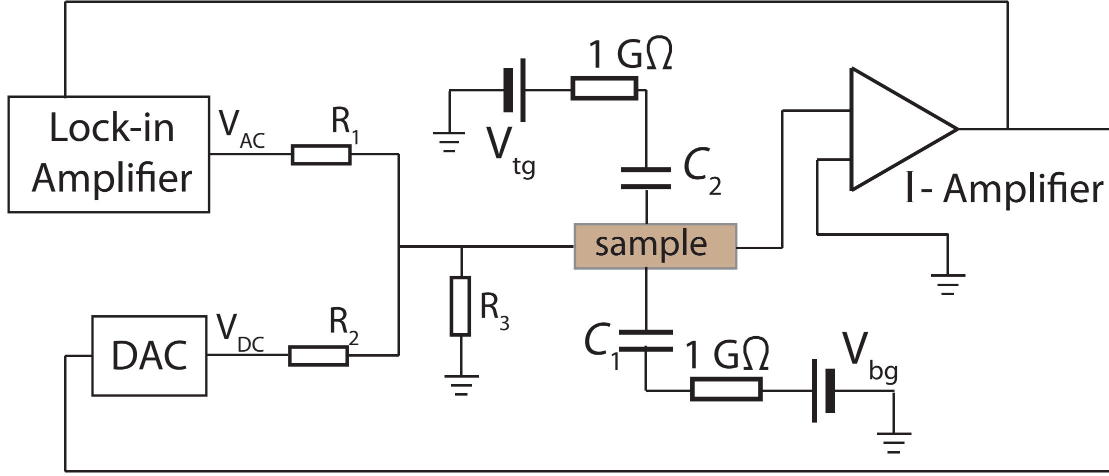

Figure 4.4: Electric circuit for the measurements of $I-V$ and $dI/dV-V$ characteristics at low temperature. The resistances R_1 and R_2 and R_3 are respectively 10 MΩ, 10 kΩ and 100 Ω.

for the same gate configurations, along the line of maximum resistance (dashed line on Fig.4.3b), is low when the Fermi level is in the middle of the band-gap. In contrast, a high dI/dV is observed when the Fermi level lays in the conduction or valence bands (see Fig.4.5b). This is another indication of an electric-field tunable energy gap. Indeed, the energy gap roughly corresponds to $\Delta V_{SD}/2$, since the zero-current region on $I-V$ curves reflects the situation when the energy, associated with an excitation voltage (eV_{SD}, e is electron charge), is less than the size of the band gap.

4.4 Temperature dependence analysis

To demonstrate that we probe an intrinsic band-gap in these electrical transport experiments, we performed a detailed study of the temperature dependence of the conductivity. These measurements can distinguish if charge carriers are hopping between sub-gap impurity states or if they are thermally excited between valence and conduction band over the energy gap (Δ). In the hopping regime, depending on the specific conduction mechanism and on the relevance of correlation effects, the temperature dependence of conductivity (σ) for a two dimensional system is described by $\sigma = \sigma_0 \exp(-(T_0/T)^n)$ with n = 1;1/3 or 1/2 and T_0 a characteristic parameter which is a function of the activation energy of hopping* [102]. On the other hand, in the absence of impurity

*The n=1/3 case corresponds to a hopping conduction mechanism with the assumption that there is a constant density of localized states (Mott's Variable Range Hopping (VRH) in a 2D system).

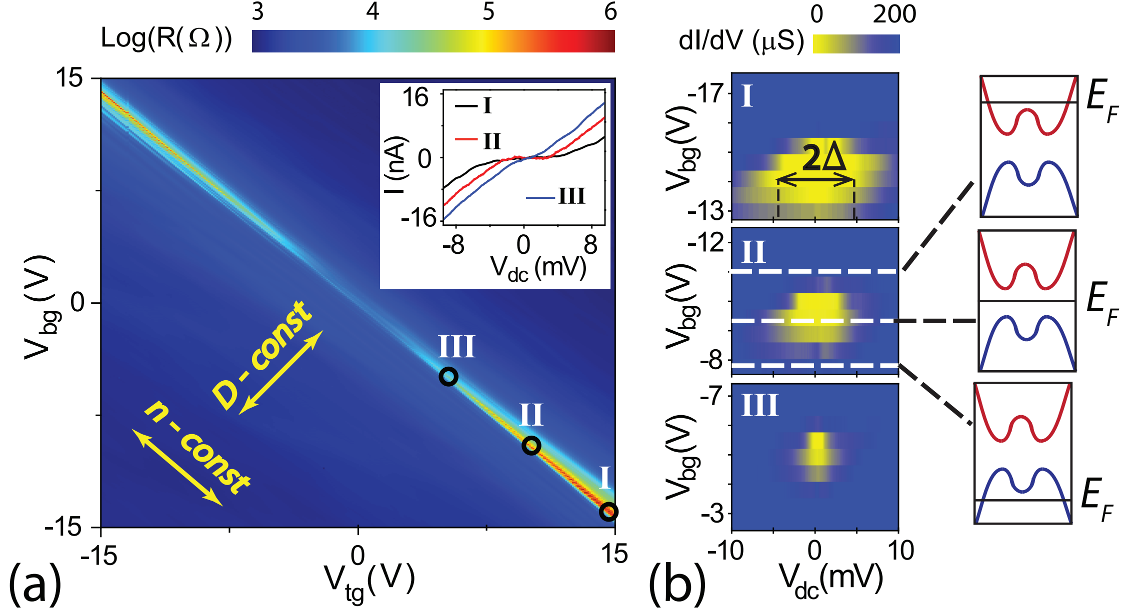

Figure 4.5: (a) Color plot of log(R) as a function of V_{tg} and V_{bg}. Yellow arrows indicate the directions of a constant carrier concentration and an electric displacement correspondingly. The inset shows $I - V$ characteristics at the R_{max} for 3 different gate configurations (I, II and III) highlighted in the main graph. The differential conductance dI/dV versus V_{sd} and V_{bg} for fixed V_{tg} corresponding to I, II and III is plotted in panel (b). The sketches on the right hand side show a schematic low-energy band structure of ABC-trilayer and the position of the Fermi level (E_F) for the three different values of V_{bg} indicated by the white dashed lines.

states thermally activated electrical transport described by $\sigma = \sigma_0 \exp(-\Delta/2k_B T)$ (k_B is Boltzmann constant) is expected. In addition, for short channel high quality devices and at low temperatures ($k_B T < \Delta$), a sub-gap electrical current is expected due to quantum tunneling through the energy barrier defined by Δ.

Figure 4.6b shows some representative Arrhenius plots (log(σ) vs. 1/T) of the temperature dependence of the minimum conductivity σ for different values of D. It is apparent that in all cases the experimental data are well described by a linear fit, as expected for thermally activated transport in intrinsic semiconductors and Δ is the only fitting parameter for the slope. We find that the band-gap can be continuously tuned up to $\Delta = 5.2 \pm 0.06$ meV at D = -117 mV/nm (see Fig.4.7a). To understand the temperature dependence of σ down to cryogenic temperatures, we consider the

For highly disordered systems the role of electron-electron interactions should be taken into account. This leads to a power n=1/2, which is valid for 2D and 3D cases (Efros-Sklovskii VRH). When the localization is strong (or the concentration of localized states is low), at a higher temperature region the hopping occurs between the nearest neighbour sites, which leads to a power n=1 in the exponent (Nearest Neighbour Hopping).

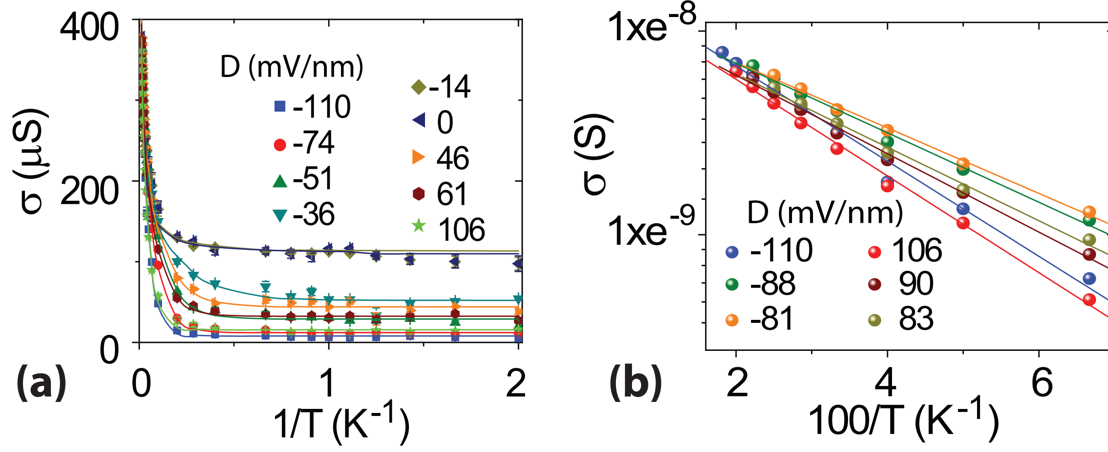

Figure 4.6: (a) Arrhenius plot for different values of external electric displacement. The dots are experimental data and the continuous lines are fit to thermally activated transport over the band-gap Δ.(b) Minimum conductivity as a function of inverse temperature for different average external electric displacements, as indicated. The dots are experimental data points, whereas the continuous line is a fit to Eq.(4.1).

combination of thermally activated transport and quantum tunneling through a short-channel semiconductor with a clean band-gap. The conductivity is given by the relation

$$\sigma = 2\mu e \int_{\Delta/2}^{\infty} \nu(E) f(E) dE + \sigma_1, \tag{4.1}$$

where $\nu(E)$ is the density of states for ABC-trilayer, $f(E)$ is the Fermi distribution and σ_1 is the measured low-temperature residual conductivity due to quantum tunneling. The low-energy dispersion of ABC-trilayer is described by one pair of conduction and valence bands trigonally warped below the Lifshitz transition point (see Chapter1, Sec.1.3.4) evolving into a cubic dispersion for E $\geq$ E$_L$ ($\sim$10 meV). In our experiments, both the temperature range and the values of Δ (see Fig.4.7a) are smaller than the energy corresponding to the Lifshitz transition (E$_L$). Therefore, we are probing electrical transport at the edges of the conduction and valence bands. The opening of a band-gap introduces a parabolicity at the band edges ("mexican hat"-like shape [23]), resulting in a constant density of states (DOS). Figure 4.6 shows that considering a constant DOS in eq.(4.1) gives an accurate fit to the experimental data. For $\Delta \ll E_L$ the low energy dispersion is similar to 3 gapped Dirac cones. In this case the density of states is represented in eq.(1.41)*. However, even in this limit, the difference between the

*Basically, $\nu(E) \sim |E|\Theta(|E| - \Delta)$

values of Δ found considering a linear or parabolic dispersion is within experimental error.

4.5 Results

The estimated values of Δ from the fit to eq.(4.1) are consistent with the values found from the Arrhenius plot analysis and they also correspond to the energy scale of the non-linearity measured in the $I-V$ characteristics (see Fig.4.5a and b). As was described in Chapter1, the self-consistent tight binding model predicts that the low-electric field dependence of the energy gap in rhombohedral-stacked multilayer graphene is $\Delta \propto D^{N/2}$, with N the number of layers [23, 30]. We verify this theoretical prediction by fitting the experimental data for $\ln(\Delta)$ vs. $\ln(D)$ to a linear slope. The best fit gives $N = 3\pm0.3$ as expected for the intrinsic band-gap in ABC-trilayer graphene (see Fig.4.7).

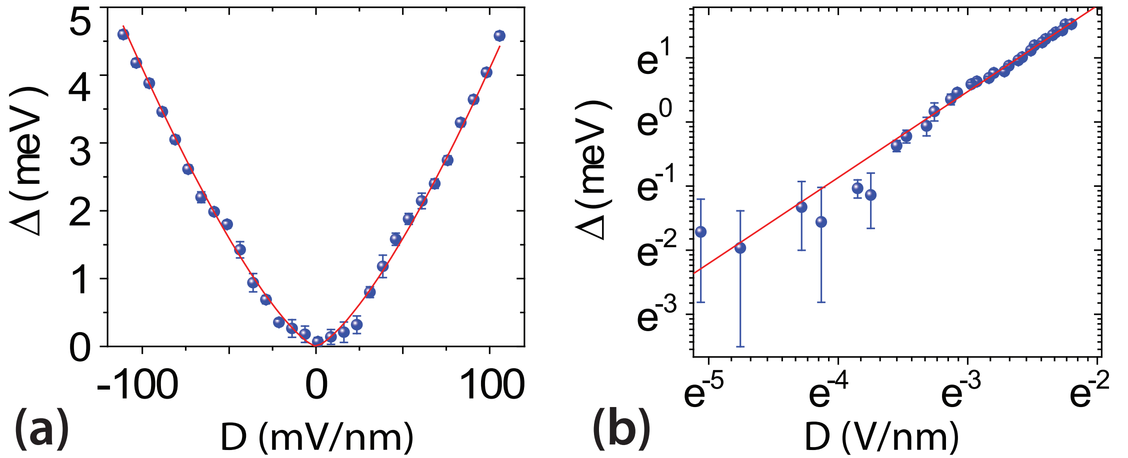

Figure 4.7: (a)The values of the band-gap, extracted from the fit to experimental data using eq.(4.1), as a function of D. The continuous line is a fit to $\Delta \propto D^{3/2}$ (see the main text for the description). Linear fit of $\ln(\Delta)$ vs. $\ln(D)$ with best fit $N = 3\pm0.3$.

Remarkably, the obtained result is independent on a sample size (see Fig.4.8). The values of the energy gap for another sample with different aspect ratio and mobility (L∼700nm , W∼450nm, μ ∼20 000 cm^2/Vs) are in a good agreement (within the experimental error*) with the data obtained for another sample. The energy gap for the sample#2 estimated from $I-V$ curves correlates well with the results obtained in temperature dependence analysis. Given facts exclude any possibility of hopping

*The error arises from the uncertainty in temperature measurements

mechanism to be involved in transport, leaving only thermal activation across bare energy gap. Indeed, assuming the possibility of realization of nearest neighbour hopping (NNH), which, in fact, gives similar dependence ($\propto$ exp(-1/T)) at higher temperatures, this would introduce new states in the mobility gap region of the DOS and would be reflected in transport. In this regime the contribution to the conductivity is attributed to the average transmission probability between localized states. This contribution, therefore, depends on the localization radius and is very unlikely to be the same for two different systems, since the impurity sites are distributed randomly. Thus, following the assumption, in the given case the activation energy should vary from sample to sample. Instead, we demonstrate that values for the band gap are consistent with those measured in the sample#1. One may conclude that observed energy gap is an intrinsic property of ABC trilayer graphene.

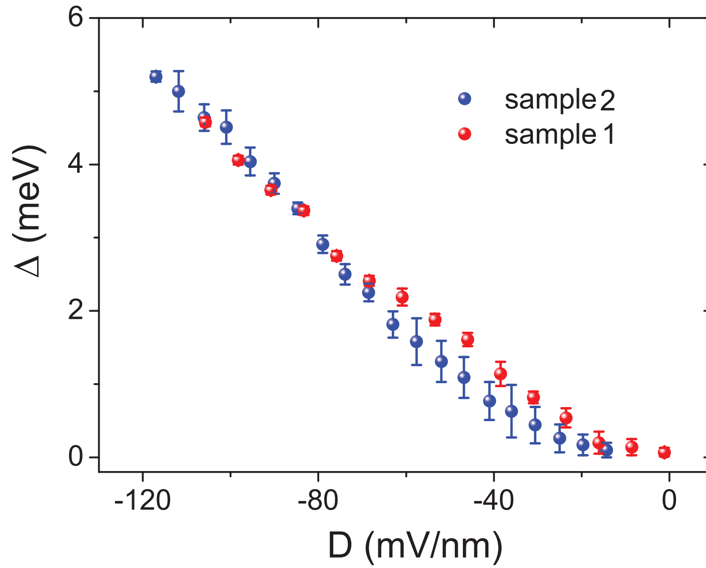

Figure 4.8: (a)Energy gap Δ as a function of average electric displacement D. Red and blue circles correspond to two different samples, as indicated in the graph.

4.6 Conclusions

In conclusion, we have reported a detailed study of the source-drain bias-, temperature- and perpendicular electric field-dependence of the resistance in high quality suspended double gated ABC-trilayer graphene. All these independent measurements consistently showed the appearance of an energy gap in the density of states of ABC-trilayer. We

have demonstrated that we can tune Δ up to 5.2 meV for an average electrical displacement of 117 mV/nm. The values of the energy gap estimated from the temperature dependence of the minimum conductivity correlate well to the energy range of non-linearity, measured in the current-voltage ($I - V$) characteristics. Our experiments present direct observation for a clean band-gap in electrical transport measurements in rhombohedral-stacked trilayer graphene.

The report done in this Chapter is submitted for the publication in 2012.

Chapter 5

Quantum transport in multilayer graphene structures at high magnetic field

5.1 Introduction

The exceptional nature of the charge carriers in graphene reveals a very distinguishable quantum Hall effect amongst conventional 2D electronic systems. Recent research interest was directed towards the exploration of magneto-transport characteristics in samples with reduced disorder. After success in fabrication of high-quality graphene devices, the observation of fractional QHE [63, 105, 106] and newly resolved broken symmetry states [66,85,107,108] disclosed novel physics, rich in interaction phenomena. In this regard the study of multilayer graphene is more intriguing compared to its single layer counterpart, due to an additional layer degree of freedom attributed to these systems, along with present spin-valley degrees of freedom. Enhanced electronic interactions in thin graphitic samples can result in fascinating quantum effects, like in bilayer graphene, where spontaneous symmetry breaking lead to an insulating state at the charge neutrality point [85, 109]. Due to the possession of the same type of symmetry as in Bernal-stacked bilayer graphene, one may expect similar effects arising in ABC trilayer.

The ability to produce high-quality dual gated devices creates a platform for study of unconventional quantization, induced by interlayer asymmetry in multilayer

graphene devices at low magnetic field in a quantum Hall regime. Concerning trilayer graphene, new broken symmetry states resolved by means of perpendicular electric field were reported only recently [67] in Bernal-stacked samples. So far there was no detailed investigation of broken symmetry states in ABC trilayer graphene.

In this chapter we study quantum Hall effect in trilayer graphene with particular focus on rhombohedral-stacked trilayer devices. We observe new broken symmetry states which are investigated at different applied perpendicular magnetic and electric fields. At high carrier concentration some Landau levels are split in the groups of three, which can be the signature of the Lifshitz transition predicted theoretically [15]. We also investigate the transition between quantum states at $\nu = 0$ Landau level at the regions of high and low external perpendicular electric and magnetic fields. It is found that at zero carrier concentration and high electric displacements the more energetically favourable state with $\nu = 2$ is realized as the magnetic field is increased.

5.2 Effect of external electric field on broken symmetry states in QH regime

5.2.1 Two terminal transport measurements in perpendicular magnetic field

Samples are fabricated by mechanical separation of thin graphene flakes from bulk graphite piece*. We follow the method described in [97] to fabricate two-terminal suspended and double-gated trilayer devices. The number of layers is verified by means of optical contrast technique and Raman spectroscopy. To identify the stacking order we employ a detailed analysis of the 2D Raman peak (Chapter2, Sec.2.3.2). The transport measurements are performed at low temperatures (300 mK) in the "Heliox" system with the superconducting magnet. An applied magnetic field is varied from 0 to 8 Tesla during the experiment. Our measurements are performed using a lock-in amplifier in a voltage-biased two-terminal configuration. We use the same experimental set-up as shown on Fig.4.2. To prevent the arising of non-equilibrium effects due to overheating of the electrons we stay in the linear regime, when the excitation voltage

*As was mentioned in Chapter4, "Kish graphite" (Toshiba ceramics) provides with high probability of obtaining rhobmohedral-stacked graphene flakes

across the sample is less than $k_B T$ (k_B is the Boltzmann constant).

At first, quick measurements of the resistance as a function of top- and back-gate voltages confirm the stacking order in trilayer devices. Indeed, in the case of ABA stacking arrangement an external perpendicular electric field causes the decrease of the resistance at the charge neutrality point (CNP) attributed to a band overlap [14]. In contrast, the gate-induced band gap in ABC trilayer leads to a dramatic increase of the maximum resistance (for example see Fig.4.3c and Fig.4.5a). The studied samples have transport mobility μ ~15-20 m^2/Vs at $n = 5 \cdot 10^{11}$ cm^{-2}. These values are comparable to the so-called quantum mobility μ_Q values, which are estimated from the relation $\mu_Q B_0 \sim 1$ (B_0 is the magnetic field at which the quantized plateaus start to appear) [62].

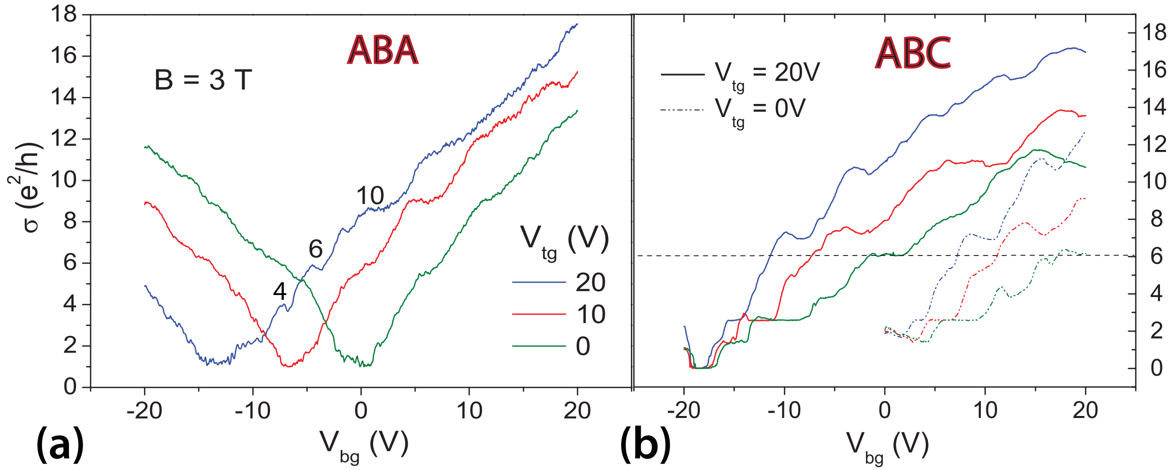

Figure 5.1: Conductance in units e^2/h as a function of V_{bg} for ABA(a) and ABC(b) trilayer graphene measured at T = 300mK. In (a) the data are taken at fixed magnetic field B = 3T for three values of top-gate voltages as indicated on the graph. The numbers on the blue curve correspond to different filling factors ν. In (b) the measurements are performed at B = 3(blue), 5(red) and 7(green) Tesla. The dotted and solid lines represent the data at fixed V_{tg} = 0 and 20 Volts respectively.

We aim to study the influence of an external perpendicular electric field on the evolution of the quantum Hall plateaus where the appearance of new broken-symmetry states is expected. To investigate this we measure first the conductance of trilayer samples as a function of back-gate voltage at various fixed top-gate voltages (Fig.5.1a and b). For Bernal-trilayer, when V_{tg} = 0V, the series of plateaus appear at expected quantization sequence [47], i.e $G = \pm 6, \pm 10$... An additional plateau at $\nu = 4$ starts to evolve as external electric field, related to the top-gate voltage, increases. The

signature of $\nu = 2$ and 8 is also observed. Similar result was reported recently by other experimental group [67]. Since unexpected sequence of newly resolved plateaus could not be explained simply within tight-binding model with all intra- and inter-layer coupling constants, the suggested explanation for the broken symmetry states was attributed to the influence of electronic interactions in trilayer samples with high mobility.

In the case of rhombohedral-stacked trilayer the effect of the out-of-plane electric field is more pronounced (see Fig.5.1b). At higher electric field unexpected QH plateaus at ν =0;2;3 are well developed. There is also a signature of $\nu = 4$ state appeared at high magnetic field. The quantization steps for $\nu = 2$ and 3 are resolved at B $\sim$ 1T and zero external electric field. The observation of $\nu = 3$ state in ABC trilayer was reported once in Ref. [17]. However, there was no detailed investigation concerning this arisen plateau. Developed $\nu = 2; 3$ states can be an indication of a spin- or valley-splitting and their nature require detailed analysis. In particular, the plateau at $\nu = 3$ was ascribed to a bias supported state which was anticipated persisting down to almost zero B-field [110]. There is another interesting feature that was identified around CNP. The plateau at $\nu = 2$ is quite robust when an average electric field is zero and then QH state at $\nu = 0$ evolves as E increases. We will return to the discussion of this point later in this chapter.

It is worth noticing that despite two-terminal geometry of the devices, which precludes the independent measurements of longitudinal and transversal components of the conductivity, the plateaus are yet clearly observable. The explanation is rather simple. In a real experiment we measure the resistance, which can then be converted to the conductivity. The transversal conductivity component is related to the resistivity as follows: $\sigma_{xy} = -\dfrac{\rho_{xy}}{\rho_{xx}^2 + \rho_{xy}^2}$. This means that even when the longitudinal resistance goes to zero (the Fermi level lies between the extended states) σ_{xy} is still finite. Thus, when one is measuring two-terminal conductance in the QH regime the transversal component makes a dominant contribution to this, resulting in quantized plateaus (for qualitative explanation see the current lines shown in Fig.5.2).

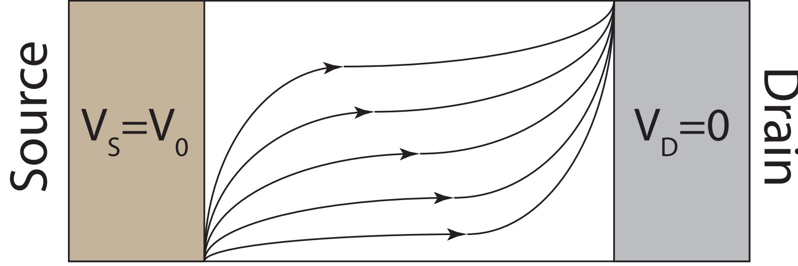

Figure 5.2: Schematic representation of the current lines in a sample with two-terminal geometry in the QH regime [111]. The current lines originate from one corner of the sample (left bottom corner) and terminate in the opposite corner. V_S and V_D denote source and drain voltage.

5.2.2 Evolution of QH plateaux with carrier concentration and magnetic field

A two terminal measurement of G(V_g) versus B does not provide accurate quantization values for the plateaus due to the presence of the contact resistance. This is reflected in shifted values of conductance in units of e^2/h, where the level of a plateau does not coincide with an integer number. Therefore, in order to analyse the appearance of LLs we represent the data in the form of so-called fan diagram : the derivative of the conductance over magnetic field as a function of B and n (n is the carrier concentration). The latter is determined by V_{bg} and V_{tg} via the following relation [95] : $n = \varepsilon_0/e \left(\frac{\varepsilon}{d_a\varepsilon + d_{ox}} \left(V_{bg} - V_{bg}^{NP}\right) + \left(V_{tg} - V_{tg}^{NP}\right)/d_{tg} \right)$ (d_{tg}=140nm, d_a=85nm, d_{ox}=215nm, ε_0 is electric constant and $\varepsilon = 3.9$ for SiO_2). In a fan diagram the QH plateaus are manifested as coloured lines or narrow bands on the (n,B)-plane, diverging from the origin (point of zero concentration and magnetic field). The corresponding filling factors can be found from the slopes of these lines/bands via the following relation: $\nu = nh/(eB) = \alpha V_g h/(eB)$, where α is the gate's coupling efficiency.

Shubnikov-de-Haas (SdH) oscillations measurements for identifying accurately the carrier concentration are impossible because of 2-terminal geometry in our devices. Thus, we rely on the capacitive constants, calculated for top- and back- gates in the samples using plane capacitor model. The data for dG/dB (in a colour scale) as a function of V_{bg} and B are represented on Fig.5.3b. The dashed lines follow the filling factors that were calculated using the aforementioned relation. Aside from expected quantized steps for ABC trilayer ($\nu = 6; 10; 14...$) one can also distinguish the separated

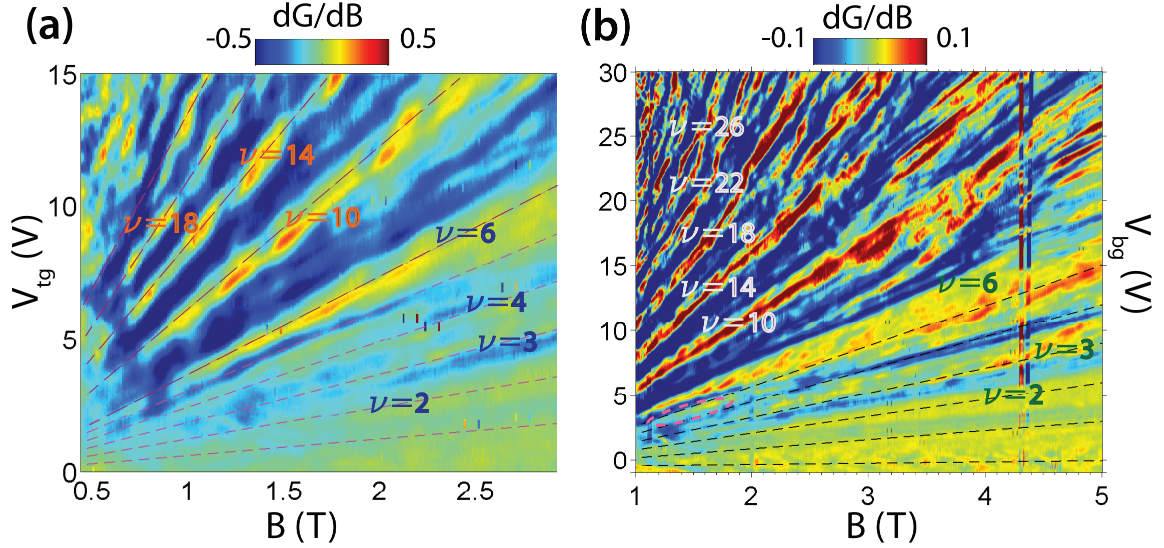

Figure 5.3: Fan diagram - dG/dB(in colour scale) as a function of gate voltage and magnetic field - of ABC trilayer at T = 0.3K. (a) The data are taken at fixed V_{bg} = 0V when V_{tg} is varied. (b) The top gate voltage is fixed (V_{tg} = 0V) and the V_{bg} is varied. Dashed lines in (a) and (b) are guide lines that correspond to filling factors ν (some of them are shown on the graphs), calculated as described in the main text.

lines that correspond to $\nu = 2$ and 3 filling factors. Between B ∼1 and 2 Tesla the signature of occured plateau close to the filling factor $\nu = 5$ is notable. The thin line, corresponded to this plateau and highlighted by the dashed ellipse, then merge into $\nu = 6$ at higher magnetic field. To determine the capacitive constant to the back-gate we need the value of the distance from SiO_2 to graphene (d_{ox}), which we cannot define precisely due to the difficulty in the control of etching time, that results in an uncertainty of ∼5-6 nm. For this reason in order to confirm the values of the filling factors that correspond to the arisen quantization steps we perform similar measurements at fixed V_{bg}=0 while sweeping V_{tg} and B (Fig.5.3a).

Interestingly, the plateaus $\nu = 2; 3$ are observable at both zero and finite electric field indicating that they have spin-polarized (ferromagnetic) nature [85] rather than layer-polarized. This is in contrast with theoretical expectation [110], where $\nu = 3$ QH state should be enhanced by external electric field. One may expect that newly resolved plateaus appear at non-zero interlayer asymmetry, induced by transversal E-field and ascribe this to the valley splitting, since the inversion symmetry protecting valley degeneracy is broken. Remarkably, these plateaus are seen at zero electric field when the magnetic field is relatively low (≤1.5T). We believe that in our low-disorder devices electronic interactions play a prevailing role in the formation of these QH

states (it is anticipated that interaction effects are stronger for ABC trilayers than for ABA and more likely result in developed intermediate filling factors [110]). The measurements performed at different tilt-angles of the magnetic field along with the temperature dependence analysis of the minimum of longitudinal resistance at a given filling factor could provide with the information about the nature of arising plateaus and about possible mechanism of the interactions that cause the symmetry breaking.

5.3 Signature of the Lifshitz transition

In the Chapter1 we discussed that in ABC trilayer graphene the trigonal warping effect leads to the topological transition of the Fermi surface, called the Lifshitz transition. This transition was predicted [15] to be observed in the quantum Hall effect and manifested as a splitting of Landau levels in groups of three. This is the consequence of broken degeneracy in ABC trilayer when $n \geq 10^{11}$ cm^{-2}. We expect the appearance of new plateaux on the fan diagram. Figure5.4 shows the evolution of QH plateaus as the magnetic field and the charge density are increased. One can notice the splitting, appeared along the lines that correspond to the filling factor $\nu = 22$, as shown on the figure. The splitting is barely seen in Fig.5.3a at $\nu = 10$ when higher magnetic field is applied. To gain further insight we do the high resolution scan over the range of larger B and n (Fig.5.4b). The signature of the Lifshitz transition is observed when $n \sim 7{\cdot}10^{11}$ cm^{-2} and B $\sim$ 1.5T. These values are slightly higher than it was predicted ($n \sim 2.6{\cdot}10^{11}$ cm^{-2}, B$\sim$1T) [15] and estimated experimentally [16]. The detailed analysis of occured splitting with an accurate measurement of the values of carrier concentration and magnetic field at this topological transition would allow to determine the coupling parameters γ_1 and γ_2 in ABC trilayer [15, 23] in experiment. The observed transition, however, is not apparent in our data. Even more, according to the theory, the splitting of LLs should appear for $\nu = \pm 6; \pm 18; \pm 30$. Surprisingly, we find the signature of the Lifshitz transition also for $\nu = 10; 14$ and 22 Landau levels.

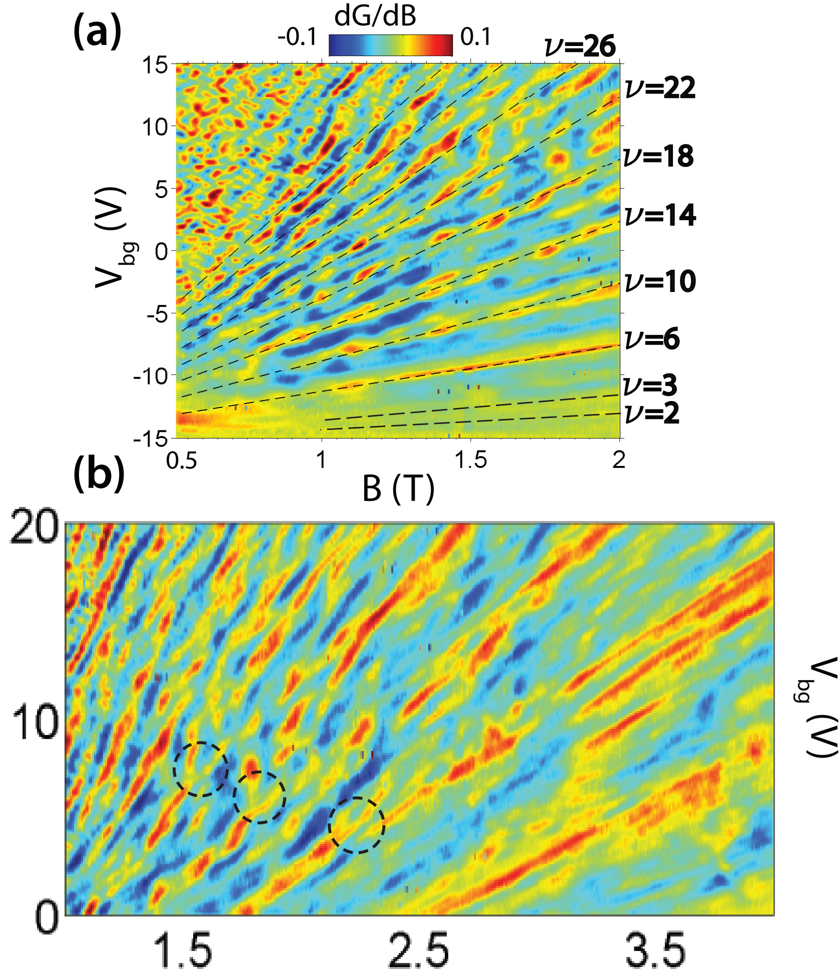

Figure 5.4: (a) Fan diagram - $dG/dB($ V_{bg},$B)$ - of ABC trilayer graphene at T = 300mK. The top-gate voltage is fixed at V_{tg} = 15V. The dashed lines are guide lines for calculated filling factors. Values of ν against given dashed lines are shown outside of the image. (b) High resolution scan related to (a). The measurements are performed over the range of B and V_{bg} indicated on the graph. The dashed black circles represent the regions of Landau levels splitting due to the Lifshitz transition.

5.4 $\nu = 0$ LL and the transition between quantum Hall states

We now consider the origin of an insulating state at $\nu = 0$ and try to explain why we observe the quantization at $\nu = 2$ instead when the external electric field is zero (Fig.5.1b). In graphene-based systems, like mono-, bi- and ABA tri-layer, the appearance of an insulating state at a finite magnetic field was reported in many experiments [46,49,67,85,112,113]. This effect was ascribed to electron-electron interactions. Nevertheless, there is no signature in our data of an appearance of the insulating state at zero electric field when magnetic field increases.

One needs to analyse the behavior of the conductance around the NP region at various magnetic and perpendicular electric fields in order to elucidate the origin of the $\nu = 0$ and $\nu = 2$ QH states. In a similar way as was done in Chapter4 we define an average electric displacement as $D = (D_{bg} + D_{tg})/2$, where $D_{bg} = \frac{\varepsilon}{d_a\varepsilon + d_{ox}} V_{bg}$ and $D_{tg} = V_{tg}/d_{tg}$. Figure5.5 (left image) shows the conductance (in color scale) as

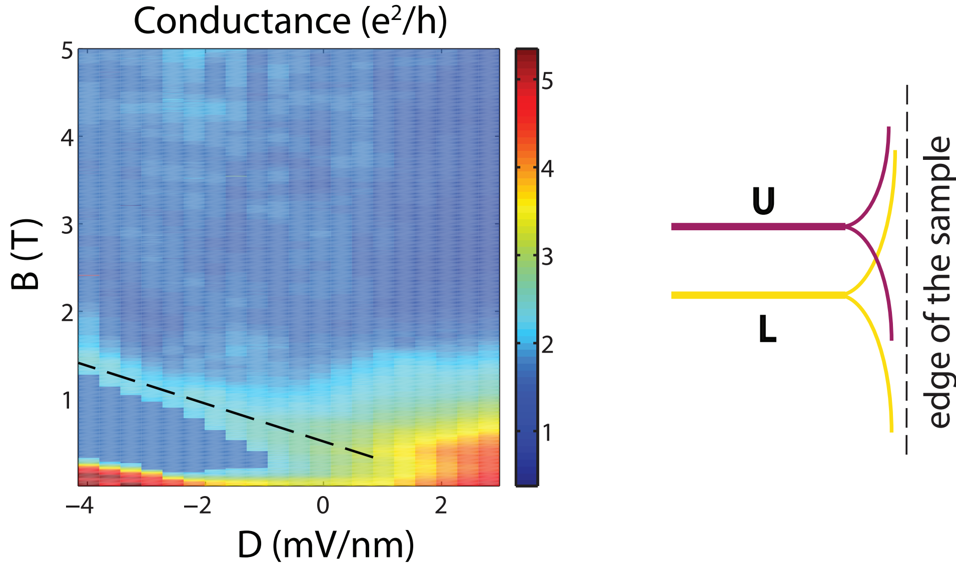

Figure 5.5: (a) Colorplot of the conductance in units e^2/h as a function of applied out of plane electric and magnetic fields. The data are taken around neutrality point region. The dashed line guides the transition region between $\nu = 0$ and $\nu = 2$ states. The picture on the right is a schematic representation of the counter-propagating edge modes, which have opposite layer indices (U and L for upper and lower layers respectively).

a function of magnetic and electric fields around zero concentration*. The plateau at $\nu = 2$ is quite robust when an average electric displacement is zero. The stability of this state at high magnetic field suggests its spin-polarized origin [85]. When the electric displacement increases the transition region is seen (dashed line guides the transition on the left picture of Fig.5.5). Destabilized by electric field, the $\nu = 2$ QH state turn to $\nu = 0$, which has the same spin polarization but opposite layer polarization. This can be explained as follows : the transition in ABC trilayer occurs due to counter-propagating spin-polarized edge modes with opposite layer polarization, coexisting at the same edge (Fig.5.5 on the right hand side). The $\nu = 2$ and $\nu = 0$ Landau levels are split in energy by electric field where electron-like and hole-like edge states for different layers diverge in opposite directions at the sample edge. In this case the ferromagnetic

*We fix V_{tg} at 0.15 V and sweep V_{bg} between -1 and 1 V

(spin-polarized) $\nu = 0$ state of the lower layer can propagate to the upper layer. The transition between two states happens at the crossing of given Landau levels [11].

The conductive region (specified with red color) along the line of zero magnetic field(Fig.5.5) can be a signature of another transition, when applied out-of-plane electric field is much larger. To understand this we implement similar measurements at higher magnetic and electric fields. We stay exactly at the neutrality point and measure the magneto-conductance, sweeping magnetic field from 0 to 8 T and moving along the line of constant n towards the augmentation of electric field (see Fig.5.6a). It is apparent, that conductance at zero B decreases with an increment in D (indicating an opening of band-gap by breaking inversion symmetry in ABC trilayer) and has a non-monotonic behavior as a function of B, passing the local maximum as the magnetic field increases. The summary of this $G(B, D)$-dependence is represented in Fig.5.6b as

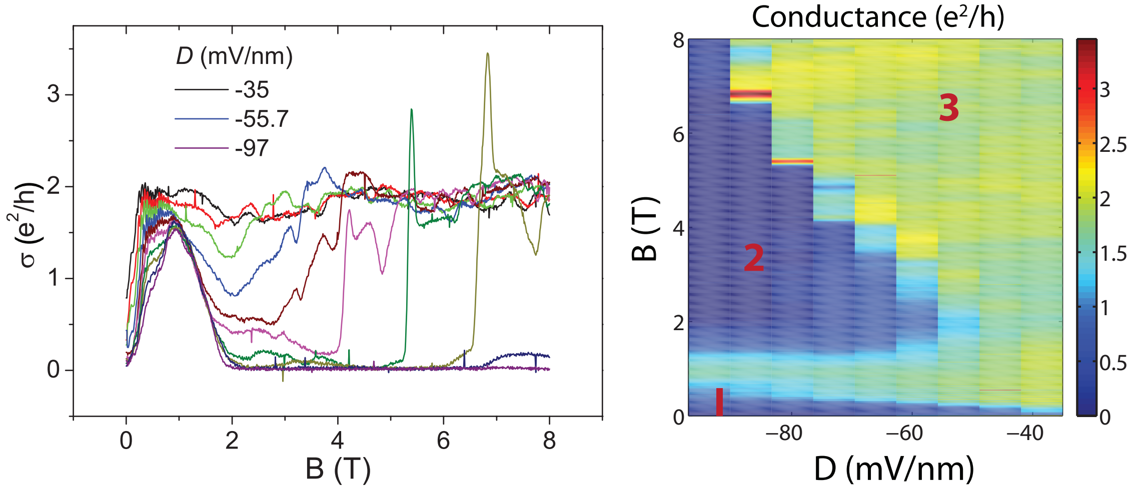

Figure 5.6: (a) Conductance of ABC trilayer (in units of e^2/h) at zero carrier concentration as a function of magnetic field for different fixed electric displacements D: the values are increasing from the top to bottom, as indicated on the graph. (b) Conductance (color scale) as a function of electric field D and magnetic filed B at zero carrier concentration. The data represent the result in (a) as the colorplot. The numbers on the figure denotes different quantum Hall states.

a colorplot data. Three different regions, denoted as "1","2" and "3", correspond to various QH states. The phase "1" of $\nu = 0$ insulating state is layer-polarized, because it is stable at large displacement and destabilized by magnetic field [85]. Further increase in magnetic field leads to the transition from the layer-polarized to spin-polarized $\nu = 0$ insulating state, marked as "2" on the figure. As the electric field decreases with increasing B, the phase, where $\nu = 2$ (region "3" on the colorplot), become more ener-

getically favorable and the transition from the spin-polarized insulating state ($\nu = 0$) to $\nu = 2$ state happens. Unfortunately the lack of the data points does not allow us to investigate carefully the given transitions. The full scan from high to low electric fields might give a complete picture with all existing regions of different phases for the charge neutrality state.

5.5 Conclusions

To sum up, we observed new broken symmetry states in ABC trilayer graphene which were likely induced by electron-electron interactions in low-disordered suspended sample. Both $\nu = 2$ and $\nu = 3$ quantum Hall states were stable at low out-of-plane electric field indicating their ferromagnetic nature. The arisen splitting of higher Landau levels in groups of three at larger carrier concentration signify the topological transition of the Fermi surface, expected in theory. The effect of a transversal electric field on the Lifshitz transition has not been noticed in this experiment. At zero carrier concentration the transition between two $\nu = 0$ insulating states was observed.

Apart from intriguing phenomena revealed in our ABC-stacked trilayer devices in the quantum Hall regime, there are several uncertainties and disagreements with other experiments and theoretical predictions, which yet awaiting for a detailed study. Perhaps, the fabrication of high quality double gated trilayer samples with multi-terminal contact geometry would enable to solve many problems concerning experimental obstacles we have encountered with.

Conclusions and proposals for future work

In this thesis we study transport properties of few-layer graphene samples. The main interest is concentrated on trilayer devices. We report the first direct observation in transport of an electric field tunable band gap in rhombohedral-stacked trilayer graphene. The energy gap can be tuned from zero up to $\sim$ 5.2 meV for an average electric field as low as 117 mV/nm. The estimated values from the temperature dependence of maximum resistivity are well-correlated with the data extracted from the transport spectroscopy measurements. The results obtained in the experiment are consistent with theory, based on self-consistent tight-binding calculations. As a consequence of a given property, ABC trilayer graphene samples exhibit high on/off ratio of current at relatively low external electric field, which makes them very promising for a new generation of transistor-based electronics.

Probing low-energy states in the band structure of graphene-based systems became possible thanks to low-disordered top-gated devices. We focus on the fabrication technology of suspended samples with air bridge electrodes. The developed method for production of high-quality graphene samples revealed to be effective and demonstrated significant enhancement in carrier mobility, ranging from 14 000 up to 110 000 cm^2/Vs. The low level of disorder found in our samples grants an access to the quantum Hall physics at low magnetic fields.

With a use of ultra-clean dual-gated devices new broken symmetry states in ABC trilayer graphene are resolved. We report the first investigation of an insulating state at $\nu = 0$ in the quantum Hall regime in rhombohedral-stacked trilayer samples. The measurements implemented for various magnetic and electric fields at charge neutrality

point drive us to the conclusion that spin-polarized QH state with the filling factor 2 is more energetically favourable when electric field is low. The transition between two insulating states at $\nu = 0$ is observed. We believe that resolved broken symmetry states at zero electric field and relatively low carrier concentration are induced by electronic interactions in our low-disordered devices. Also, the indication of the Lifshitz transition is noticed when Landau levels, represented as a lines on a fan-diagram, split into three separated pockets. This happens when magnetic field and the charge density are higher than 1.5 T and $\sim 7 \cdot 10^{11}$ cm^{-2} respectively. The obtained results underscore the importance of graphene-based systems with reduced disorder on new interaction-induced quantum effects.

Our work also opens some fundamental questions which need further study. Below we propose future experiments that can help to shed light on these issues.

In our work we have demonstrated high quality samples, which allowed us to probe the intrinsic band-gap in ABC-stacked trilayer graphene. However, much higher values of mobilities, required to probe novel quantum Hall states introduced by interactions, can be reached with the improvement in the fabrication technology of suspended dual-gated graphene devices. We suggest that this extremely low-level of disorder can be obtained in graphene samples by introducing some extra steps of thermal annealing in the fabrication process. In particular, heating the substrate with freshly deposited flakes in the furnace will outgas the oxygen molecules and other dopants, trapped into SiO_2 layer. Additionally, the sample can be annealed inside the probe, inserted into helium dewar, prior to current annealing. Proposed thermal annealing steps will lower the impurity concentration in the oxide layer and remove the dopants from the flake before the (in-situ) high current pulse technique. This will reduce the probability of graphene oxidation during the current annealing and lead to much better quality samples. It is still an open question concerning the reason of the sample's failure, the answer to which could make cleaning method with current pulses more safe and efficient.

Furthermore, in this thesis we have focused mainly on the study of electrical transport in two-terminal devices. This geometry is not ideal for addressing the physics of quantum Hall states. More specifically, in a two-terminal devices the contact resistance (R_C) is always in series to the resistance of the conductive channel. Therefore, the quantization sequence of quantum Hall states will appear for values of R_{xy} which

contain R_C and which varies from sample to sample. This problem is solved in a four-terminal geometry, where the source-drain leads are physically separated by the voltage probes. However, fabricating high quality suspended multi-terminal devices presents some serious technological challenges such as non-homogeneous current annealing [62]. We suggest to pre-define the shape of graphene flakes, where the Hall bar geometry is patterned by RIE before fabrication of the contacts. For suspended devices with this particular geometry the distance between all neighbouring contacts should be less than 1 μm. After current annealing step the middle area of the flake between four potential contacts is expected to be uniformly clean and homogeneous in the context of charge density, since Cr/Au electrodes now do not directly touch the channel between source-drain contacts (like in Fig.3.8a).

Occured disagreement between theory and our experimental results for ABC trilayer graphene in the quantum Hall regime require a detailed study. In particular, the mechanism of symmetry breaking of QH states when the degeneracy is lifted up can be partially understood with the help of extracted activation energy for a certain filling factor plotted as a function of magnetic field. With the Hall bar geometry this becomes possible, since one can measure the temperature dependence of longitudinal resistance independently of the transversal component. In addition, the behaviour of magneto-transport characteristics at different tilted magnetic field can answer the question of whether the resolved broken symmetry state has a ferromagnetic nature or not. Due to the lack of data points in our measurements, it is important to repeat the experiment with high quality ABC trilayer graphene in order to carefully investigate the transition between the insulating states of a charge neutral sample, performing the high resolution scan of conductance over big range of external electric and magnetic fields. Apart from interaction induced QH states, a careful study of the Lifshitz transition is yet to be done. There is only one report about observed LL splitting attributed to this topological transition [16]. However, it is still unclear whether appeared splitting of Landau levels into three branches induced by breaking an additional degeneracy (caused by trigonal warping in ABC trilayer), when the Fermi surface undergoes the topological transition, or by other interaction effect.

Till present the interplay between transport properties of few-layer graphene devices in the QH regime and mechanical stress still remains unexplored. It would be interesting to see an influence of high tension (the range where both the external electric

field and the carrier concentration are high) on magneto-transport characteristics of suspended 2D graphene sheets. In addition to this, it is intriguing to observe how high strain affects the change in the Fermi surface topology at the energy that correspond to the Lifshitz transition, similarly to what have been observed in bilayer graphene [64].

Bibliography

[1] K. S. Novoselov, et al., *Science* **306**(5696), 666 (2004).

[2] P. R. Wallace, *Phys. Rev* **71**(1), 622 (1967).

[3] S. Reich, J. Maultzsch, C. Thomsen, P. Ordejón, *Phys. Rev. B* **66**, 035412 (2002).

[4] K. S. Novoselov, et al., *Nature* **438**, 197 (2005).

[5] A. Bostwick, T. Ohta, T. Seyller, K. Horn, E. Rotenberg, *Nat. Physics* **3**, 36 (2007).

[6] A. K. Geim, K. S. Novoselov, *Nat. Materials* **6**, 183 (2007).

[7] M. S. Dresselhaus, G. Dresselhaus, *Adv. Phys.* **51**, 1 (2002).

[8] J. M. B. Lopes dos Santos, N. M. R. Peres, A. H. Castro Neto, *Phys. Rev. Lett.* **99**, 256802 (2007).

[9] J. Hass, et al., *Phys. Rev. Lett.* **100**, 125504 (2008).

[10] G. Li, et al., *Nat. Physics* **6**, 109 (2009).

[11] J. D. Sanchez-Yamagishi, et al., *Phys. Rev. Lett.* **108**, 076601 (2012).

[12] H. Lipson, A. Stockes, *Proc. R. Soc. London* **A181**(5934), 1530 (101).

[13] M. Koshino, E. McCann, *Phys. Rev. B* **79**, 125443 (2009).

[14] M. F. Craciun, et al., *Nat. Nanotechnology* **4**, 383 (2009).

[15] M. Koshino, E. McCann, *Phys. Rev. B* **80**, 165409 (2009).

[16] W. Bao, et al., *Nat. Physics* **7**, 948 (2011).

[17] L. Zhang, Y. Zhang, J. Camacho, M. Khodas, I. Zaliznyak, *Nat. Physics* **7**, 953 (2011).

[18] T. Ando, T. Nakanishi, R. Saito, *J. Phys. Soc. Jpn* **67**, 2857 (1998).

[19] E. McCann, V. I. Fal'ko, *Phys. Rev. Lett.* **96**, 086805 (2006).

[20] J. L. Mañes, F. Guinea, M. A. H. Vozmediano, *Phys. Rev. B* **75**, 155424 (2007).

[21] J. Cserti, A. Csordás, G. Dávid, *Phys. Rev. Lett.* **99**, 066802 (2007).

[22] I. M. Lifshitz, *Zh. Eksp.Teor.Fiz.* **38**, 1565 (1960).

[23] F. Zhang, B. Sahu, H. Min, A. H. MacDonald, *Phys. Rev. B* **82**, 035409 (2010).

[24] W. Zhang, et al., *ACS Nano* **5**(9), 7517 (2011).

[25] M. Y. Han, B. Özyilmaz, Y. Zhang, P. Kim, *Phys. Rev. Lett.* **98**, 206805 (2007).

[26] F. Withers, M. Dubois, A. K. Savchenko, *Phys. Rev. B* **82**, 073403 (2010).

[27] S.-H. Cheng, et al., *Phys. Rev. B* **81**, 205435 (2010).

[28] E. McCann, *Phys. Rev. B* **74**, 161403 (2006).

[29] E. V. Castro, et al., *Phys. Rev. Lett.* **99**, 216802 (2007).

[30] M. Koshino, *Phys. Rev. B* **81**, 125304 (2010).

[31] K. F. Mak, C. H. Lui, J. Shan, T. F. Heinz, *Phys. Rev. Lett.* **102**, 256405 (2009).

[32] C. H. Lui, Z. Li, K. F. Mak, E. Cappelluti, T. F. Heinz, *Nat. Physics* **7**, 944 (2011).

[33] S. H. Jhang, et al., *Phys. Rev. B* **84**, 161408 (2011).

[34] M. Berry, *Proc. R. Soc. Lond. A* **392**, 45 (1984).

[35] M. I. Katsnelson, K. S. Novoselov, A. K. Geim, *Nat. Physics* **2**, 620 (2006).

[36] A. H. Castro Neto, F. Guinea, N. M. R. Peres, K. S. Novoselov, A. K. Geim, *Rev. Mod. Phys.* **81**, 109 (2009).

[37] Y. Zhang, Y.-W. Tan, H. L. Stormer, P. Kim, *Nature* **438**(7065), 201 (2005).

[38] Y. Barlas, K. Yang, A. H. MacDonald, *Nanotechnology* **23**, 052001 (2012).

[39] K. S. Novoselov, et al., *Nat. Physics* **2**, 177 (2005).

[40] M. Koshino, E. McCann, *Phys. Rev. B* **81**, 115315 (2010).

[41] K. V. Klitzing, G. Dorda, M. Pepper, *Phys. Rev. Lett.* **45**, 494 (1980).

[42] L. Landau, E. Lifshitz, *Quantum Mechanics: Non-Relativistic Theory*, Teoreticheskaia fizika (Izd. 3-e) (Landau, L. D, 1908-1968). Butterworth-Heinemann (1977).

[43] S. M. Girvin, *arXiv:cond-mat/9907002* p. 80 (1999).

[44] M. Büttiker, *Phys. Rev. B* **38**, 9375 (1988).

[45] K. S. Novoselov, et al., *Science* **315**(5817), 1379 (2007).

[46] Y. Zhao, P. Cadden-Zimansky, Z. Jiang, P. Kim, *Phys. Rev. Lett.* **104**, 066801 (2010).

[47] S. Yuan, R. Roldán, M. I. Katsnelson, *Phys. Rev. B* **84**, 125455 (2011).

[48] V. P. Gusynin, S. G. Sharapov, *Phys. Rev. Lett.* **95**, 146801 (2005).

[49] T. Thiti Taychatanapat, K. Watanabe, T. Taniguchi, Jarillo-Herrero, *Nat. Physics* **7**, 621 (2011).

[50] J. W. Kłos, I. V. Zozoulenko, *Phys. Rev. B* **82**, 081414 (2010).

[51] P. Blake, et al., *Appl. Phys. Lett* **91**, 063124 (2007).

[52] A. B. Kuzmenko, E. van Heumen, F. Carbone, D. van der Marel, *Phys. Rev. Lett.* **100**, 117401 (2008).

[53] A. C. Ferrari, et al., *Phys. Rev. Lett.* **97**, 187401 (2006).

[54] J. Zabel, et al., *Nano Letters* **12**(2), 617 (2012).

[55] A. Das, et al., *Nat.Nanotechnology* **3**, 210 (2008).

[56] L. G. Cancado, et al., *Nano Letters* **11**(8), 3190 (2011).

[57] N. Lindvall, A. Kalabukhov, A. Yurgens, *Journal of Applied Physics* **111**(6), 064904 (2012).

[58] M. Lee, et al., *Nano Research* **5**, 710 (2012).

[59] J.-H. Chen, C. Jang, S. Xiao, M. Ishigami, M. S. Fuhrer, *Nat. Nanotechnology* **3**(4), 206 (2008).

[60] K. Bolotin, et al., *Solid State Communications* **146**(9), 351 (2008).

[61] X. Du, I. Skachko, A. Barker, E. Andrei, *Nat. Nanotechnology* **3**, 491 (2008).

[62] A. S. Mayorov, et al., *Nano Letters* **12**(9), 4629 (2012).

[63] K. I. Bolotin, F. Ghahari, M. D. Shulman, H. L. Stormer, P. Kim, *Nature* **462**(7270), 196 (2009).

[64] A. S. Mayorov, et al., *Science* **333**(6044), 860 (2011).

[65] E. V. Castro, et al., *Phys. Rev. Lett.* **105**, 266601 (2010).

[66] W. Bao, et al., *Phys. Rev. Lett.* **105**, 246601 (2010).

[67] Y. Lee, et al., *arXiv:1210.6592* (2012).

[68] W. Bao, et al., *Nat. Nanotechnology* **4**(9), 562 (2009).

[69] W. Bao, et al., *Nano Letters* (in print), DOI: 10.1021/nl301836q (2012).

[70] A. A. Balandin, et al., *Nano Letters* **8**(3), 902 (2008), PMID: 18284217.

[71] C. Lee, X. Wei, J. W. Kysar, J. Hone, *Science* **321**(5887), 385 (2008).

[72] J. S. Bunch, et al., *Science* **315**(5811), 490 (2007).

[73] C. Chen, et al., *Nat. Nanotechnology* **4**, 861 (2009).

[74] C. R. Dean, et al., *Nat. Nanotechnology* **5**, 722 (2010).

[75] C. Diaz-Pinto, D. De, H. Peng, *arXiv:1105.6032* (2011).

[76] W. Bao, et al., *Nano Research* **3**, 98 (2010), 10.1007/s12274-010-1013-5.

[77] G. Liu, J. Jairo Velasco, W. Bao, C. N. Lau, *Applied Physics Letters* **92**(20), 203103 (2008).

[78] M. T. Allen, J. Martin, A. Yacoby, *Nat. Communications* **3**, 934 (2012).

[79] V. Singh, et al., *Nanotechnology* **21**(16), 165204 (2010).

[80] J. Martin, et al., *Nat. Physics* **4**(2), 144 (2008).

[81] E. H. Hwang, S. Adam, S. Das Sarma, *Phys. Rev. Lett.* **98**, 186806 (2007).

[82] R. V. Gorbachev, *Fabrication and transport properties of graphene-based nanostructures*, Ph.D. thesis, School of Physics.

[83] J. Moser, A. Barreiro, A. Bachtold, *Applied Physics Letters* **91**(16), 163513 (2007).

[84] N. Tombros, et al., *Journal of Applied Physics* **109**(9), 093702 (2011).

[85] R. T. Weitz, M. T. Allen, B. E. Feldman, J. Martin, A. Yacoby, *Science* **330**(6005), 812 (2010).

[86] R. Murali, Y. Yang, K. Brenner, T. Beck, J. D. Meindl, *Applied Physics Letters* **94**(24), 243114 (2009).

[87] H. Zhang, et al., *Nano Letters* **12**(4), 1772 (2012).

[88] A. Barreiro, M. Lazzeri, J. Moser, F. Mauri, A. Bachtold, *Phys. Rev. Lett.* **103**, 076601 (2009).

[89] J. Yu, G. Liu, A. V. Sumant, V. Goyal, A. A. Balandin, *Nano Letters* **12**(3), 1603 (2012).

[90] A. Barreiro, F. Börrnert, M. H. Rümmeli, B. Büchner, L. M. K. Vandersypen, *Nano Letters* **12**(4), 1873 (2012).

[91] T. Paulmier, M. Balat-Pichelin, D. L. Quau, R. Berjoan, J.F, *Applied Surface Science* **180**, 227 (2001).

[92] J. Moser, A. Bachtold, *Applied Physics Letters* **95**(17), 173506 (2009).

[93] K. Nagashio, T. Nishimura, K. Kita, A. Toriumi, *Applied Physics Express* **2**(2), 025003 (2009).

[94] W. Zhu, V. Perebeinos, M. Freitag, P. Avouris, *Phys. Rev. B* **80**, 235402 (2009).

[95] Y. Zhang, et al., *Nature* **459**, 820 (2009).

[96] F. Xia, D. B. Farmer, Y.-m. Lin, P. Avouris, *Nano Letters* **10**(2), 715 (2010), PMID: 20092332.

[97] T. Khodkov, F. Withers, D. Christopher Hudson, M. Felicia Craciun, S. Russo, *Applied Physics Letters* **100**(1) (2012).

[98] Y. Zhang, et al., *Nature* **459**, 820 (2009).

[99] A. B. Kuzmenko, I. Crassee, D. van der Marel, P. Blake, K. S. Novoselov, *Phys. Rev. B* **80**, 165406 (2009).

[100] T. Taychatanapat, P. Jarillo-Herrero, *Phys. Rev. Lett.* **105**, 166601 (2010).

[101] J. Yan, M. S. Fuhrer, *Nano Letters* **10**(11), 4521 (2010).

[102] B. I. Shklovskii, A. L. Efros, *Electronic Properties of Doped Semiconductors*, vol. 41. Springer Verlag (1985).

[103] K. F. Mak, J. Shan, T. F. Heinz, *Phys. Rev. Lett.* **104**, 176404 (2010).

[104] C. H. Lui, et al., *Nano Letters* **11**(1), 164 (2011).

[105] X. Du, I. Skachko, F. Duerr, L. A., E. Y. Andrei, *Nature* **462**(7), 192 (2009).

[106] A. F. Young, et al., *Nat. Physics* **8**(7), 550 (2012).

[107] F. Freitag, J. Trbovic, M. Weiss, C. Schönenberger, *Phys. Rev. Lett.* **108**, 076602 (2012).

[108] A. Veligura, et al., *Phys. Rev. B* **85**, 155412 (2012).

[109] J. Velasco, et al., *Nat. Nanotechnology* **7**(3), 156 (2012).

[110] F. Zhang, D. Tilahun, A. H. MacDonald, *Phys. Rev. B* **85**, 165139 (2012).

[111] R. W. Rendell, S. M. Girvin, *Phys. Rev. B* **23**, 6610 (1981).

[112] Y. Zhang, et al., *Phys. Rev. Lett.* **96**, 136806 (2006).

[113] A. J. M. Giesbers, et al., *Phys. Rev. B* **80**, 201403 (2009).

Appendix I

Substrate preparation and device fabrication.

For a successful device fabrication it is important to work with clean tweezers and beakers, which are always washed in Acetone and IPA after the end of the process. It is strongly recommended to use separate beakers for different chemicals. Below we summarize the basic fabrication steps of suspended double gated graphene samples.

- 10×10 mm SiO_2 substrates, which have pre-patterned metalized (Cr/Au) markers for 80 keV electron-beam system, boil in Acetone for 10 min at T = 90 ^{0}C.
- Sonicate in the same beaker for 10 min.
- Place the substrates into a beaker with purified water and sonicate further for 3 min.
- Transfer the substrates into IPA beakers and then sonicate for 10 min.
- Dry the specimens with Nitrogen gun and etch at low power and low gas pressure (Oxygen) for 5-7 min in RIE .
- During RIE process exfoliate bulk graphite with blue sticky tape (10-15 times) and quickly search for the areas on the tape where the density of transparent flakes is large.
- Take the substrates from RIE machine and stright after this place them facedown onto prepared tape (on the place that was selected in previous step) and press with a finger for 15-20 sec. Remove slowly the tape from the substrate.
- Search for the flakes with optical microscope and characterize them using methods described in the main text (Optical contrast and Raman spectroscopy).

- Spin-coat the substrates with A6 495K PMMA layer : 4000 rpm, 40 sec. Bake on a hot-plate at 150 ^{0}C for 10 min.
- Spin layer of A4 950-K PMMA resist on top (4000 rpm, 40 sec) and bake the substrates for 10 min at 150 ^{0}C
- Perform e-beam lithography using the pattern files made in AutoCad software.
- Develop PMMA resist in IPA:MIBK:EMK solution (15:5:1 ratio by volume) for 20 sec. During that time put the beaker into the ultrasonic bath for 1 sec. After development quickly transfer the specimen into IPA and develop for another 1 min. The sonication of the beaker with IPA for 1 sec is also recommended.
- Dry the specimen with Nitrogen and straight after place it into the vacuum chamber for further metal evaporation*.
- Evaporate 10/100 nm of Cr/Au metal (evaporation speed is maintained $\leq$1 Å/sec).
- Place evaporated samples into beaker with Acetone (separate beaker for lift-off) and boil at 90 ^{0}C for 30 min for successful lift-off process.
- Flush with IPA and then dry with Nitrogen.
- Perform the steps described in details in the Chapter3 (Sec.3.3 and 3.4) using the calibration tables in Appendix II and III for air bridge fabrication and further suspension of graphene flakes (use 30/120 nm of Cr/Au metal for the bridge and 1 min for etching time in BOE).
- Use dry IPA technique : heat the sample in IPA for 10 min at 80 ^{0}C together with pre-cleaned thick glass slide. After that gently transfer the samples from IPA beaker onto the glass slide and let the devices dry in atmosphere for 3 min (glass slide is removed from the hot plate).
- The samples are ready for a wire bonding in a chip carrier which is the last step in fabrication process.

*it is important for good quality contacts to do the evaporation step immediately after developement to prevent the doping developed regions that are exposed to atmosphere

Appendix II

Thickness calibration of spin-coated PMGI-SF6 resist and its dilution speed in MF-319 developer

Thickness dependence on spin-coating parameters

spin speed (rpm)	spin time (sec)	baking temperature (^{0}C)	backing time (min)	thickness (nm)
4000	40	150	6	246
6000	40	150	15	205
8000	50	150	10	185
9400	50	150	10	180

Table II.1: Thickness dependence on spin-coating parameters.

Thickness dependence on the concentration with respect to the "T-thinner".

Concentration (%)		
T-thinner	PMGI-SF6	thickness (nm)
50	50	65
44.2	55.8	90
39.7	60.3	115
32	68	150

Table II.2: Thickness dependence on the concentration with respect to the "T-thinner".

Given calibration was set by using following spinning parameters :

- spin speed: 4000 rpm;
- spin time: 40 sec;
- baking time: 10 min;

- baking t^0: 150^0C.

Dilution speed of PMGI-SF6 resist in the MF-319/water solution.

dilution time (sec)	etched thickness (nm)
20	75
25	95
40	140
45	150

Table II.3: Dilution speed of PMGI-SF6 resist in the MF-319/water solution (the proportion is 50%:50%).

Appendix III

Calibration of etching time of SiO_2 in BOE solution

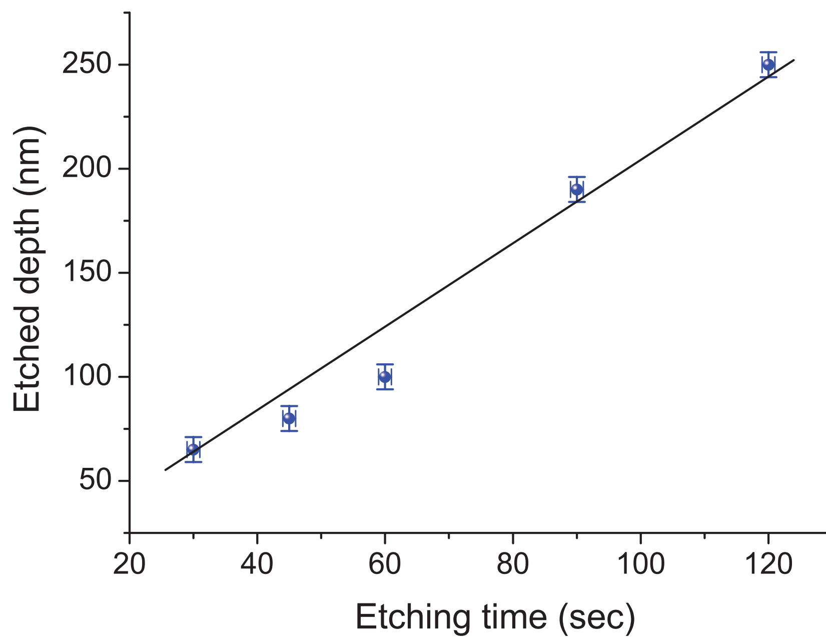

Figure III.1: Etched depth of SiO_2 as a function of etching time. A buffered oxide etch solution comprises of 40% NH_4F and 49% HF in water, which are mixed in the proportion of 6:1 by volume respectively.

Appendix IV

Statistics of suspended graphene samples broken by current annealing

Sample	L (μm)	W (μm)	V$_s$ (V)	$\jmath$ (mA/μm)	P/S (mW/μm^2)	destruction type	method	duration (s)
Y2G4SN1F8	0.55	0.7	1.47	1.1	2.3	break	sweep	5
Y2G4SN1F2	0.65	0.75	-	1.07	-	break	sweep	5
Y2G4SN2F3	0.63	0.8	1.65	1.63	4	burn	sweep	30
ASPF2	0.5	1.5	2.14	1.53	6.57	burn	sweep	20
Y2G4SN2F2	0.65	0.52	2.7	1.25	5.2	burn	sweep	20
Y2G4SN2F4	0.63	0.8	2.87	1.43	6.52	burn	sweep	60
Y3G1SBN2F11	0.76	2.3	4.32	1.05	5.96	burn	pulse	1
Y3G1SBN2F17	0.68	0.44	2.61	1.58	6.06	break	pulse	1
Y3G1SBN3F13L	0.6	0.6	3.05	1.95	6.2	break	pulse	1
Y3G1SBN3F13R	0.76	0.86	3.06	1.37	5.5	burn	pulse	1
Y3G1SBN3F4L	0.65	0.6	3.07	1.56	7.36	break	pulse	5
Y3G1SBN3F4R	0.61	0.56	2.55	1.39	5.8	break	pulse	5
Y3G1SBN3F11	0.65	0.65	2.97	1.71	7.8	burn	pulse	1
Y3G1SBN3F30	0.65	0.71	3.09	0.93	4.42	break	pulse	1
Y3G1SBN3F6R	0.56	0.4	2.55	0.98	4.46	break	pulse	3
Y3G1SBN3F6L	0.6	0.4	2.3	1.5	5.57	break	pulse	1
Y3G1SBN3F25	0.6	0.86	2.03	-	-	burn	pulse	1
Y3G1SBN3F17	0.63	0.64	2.2	1.3	4.92	break	pulse	1
Y3G1SBN4F1	0.6	0.72	2.11	-	-	break	pulse	1
Y3G1SBN4F7	0.55	0.85	2.61	1.47	5.11	burn	pulse	1
Y3G2SBN1F39	0.6	0.63	3.2	1.81	9.6	break	pulse	2
Y3G2SBN1F39	0.65	0.6	2.78	2.1	11.8	burn	pulse	10

Table IV.1: Statistics of suspended graphene samples broken by current annealing.

Here L and W are respectively length and width of a sample, $\jmath$ is a current density, V$_s$ is the voltage measured along the sample, $P/S = IV_s/(LW)$. The destruction type

named as break/burn corresponds to the cases where respectively only the sample was destroyed (the contacts remained undamaged) and the sample exploded together with the contacts. ”Method” represents whether we applied short pulses to the device or the annealing was implemented by ramping the current across the sample up to a predefined set-point.